$\bar{P}P$ BACKWARD ELASTIC SCATTERING BETWEEN 0.70 AND 2.37 GEV/C

Thesis by

John K. Yoh

In Partial Fulfillment of the Requirements

For the Degree of

Doctor of Philosophy

California Institute of Technology

Pasadena, California

1970

(Submitted May 19, 1970)

ACKNOWLEDGMENTS

The author wishes to thank his advisor, Professor Barry Barish, for advice and encouragement. The author also wishes to extend his gratitude to Professors Jerome Pine and Alvin V. Tollestrup for help and advice during and after the experiment. The author is also indebted to the other members of the collaboration who are involved with the experiment. These include Mr. Howard Nicholson of Caltech, Drs. Alan S. Carroll and Robert H. Phillips of Brookhaven National Laboratory, and Claude Delorme, Fred Lobkowicz, Adrian C. Melissinos and Yori Nagashima of the University of Rochester.

The author is also indebted to the support personnel of the three institutions, in particular to Messrs William Friedler, Hans Grau and Jack Sanders. The aid and support from the BNL computer center staff and the AGS EAO group are also gratefully acknowledged.

This research was supported by the U.S. Atomic Energy Commission.

ABSTRACT

$\bar{p}p$ backward elastic scattering has been measured for the $\cos \theta_{cm}$ region between - 1.00 and - 0.88 and for the incident $\bar{p}$ laboratory momentum region between 0.70 and 2.37 GeV/c. These measurements, done in intervals of approximately 0.1 GeV/c, have been performed at the Alternating Gradient Synchrotron at Brookhaven National Laboratory during the winter of 1968. The measured differential cross sections, binned in $\cos \theta_{cm}$ intervals of 0.02, have statistical errors of about 10%. Backward dipping exists below 0.95 GeV/c and backward peaking above 0.95 GeV/c. The 180^{o} differential cross section extrapolated from our data shows a sharp dip centered at 0.95 GeV/c and a broad hump centered near 1.4 GeV/c. Our data have been interpreted in terms of resonance effects and in terms of diffraction dominance effects.

TABLE OF CONTENTS

Index of Figures

Index of Tables

CHAPTER I: INTRODUCTION

In the study of high energy interactions, the dcs (differential cross section) at extreme angles has been very useful in revealing the important mechanisms responsible for the interaction. Strong contributions from s (except s-wave), t or u channels usually lead to dcs with characteristic peakings or dipping at extreme angles[1.1] or with characteristic dependence on energy. In the case of elastic scattering, the forward dcs is not very useful in revealing any mechanism aside from the diffraction which dominates forward scattering. Thus, the dcs for elastic backward scattering is crucial to the exploration of any important u channel and s channel mechanisms contributing to the elastic scattering. Figure 1.1 shows the Feynman diagrams corresponding to the s and u channel contributions to the backward elastic scattering of (a) $\bar{p}p$; (b) $\pi^- p$; and (c) $K^+ p$.

Away from the low energy region, s channel contribution to elastic scattering is no longer dominated by s wave. Thus, the individual partial wave amplitudes of the important terms contribute larger values to the extreme angles[1.2]. In the event that s channel is dominated by a particular resonance near a certain energy region, the s channel contribution to the extreme backward elastic dcs is characteristic. The size of the contribution peaks at the position of the resonance while at the same time there is backward peaking at the position of the resonance[1.3]. However, interference from other contributions such as u channel effects or background may obscure this behavior.

Figure 1.1: Feynman diagrams for the s and u channel contributions to the backward elastic scattering of (a) $\bar{p}p$, (b) $\pi^- p$ and (c) $K^+ p$. Quantum numbers of the s and u channels are given. Possible candidates for the contributions are given in parenthesis.

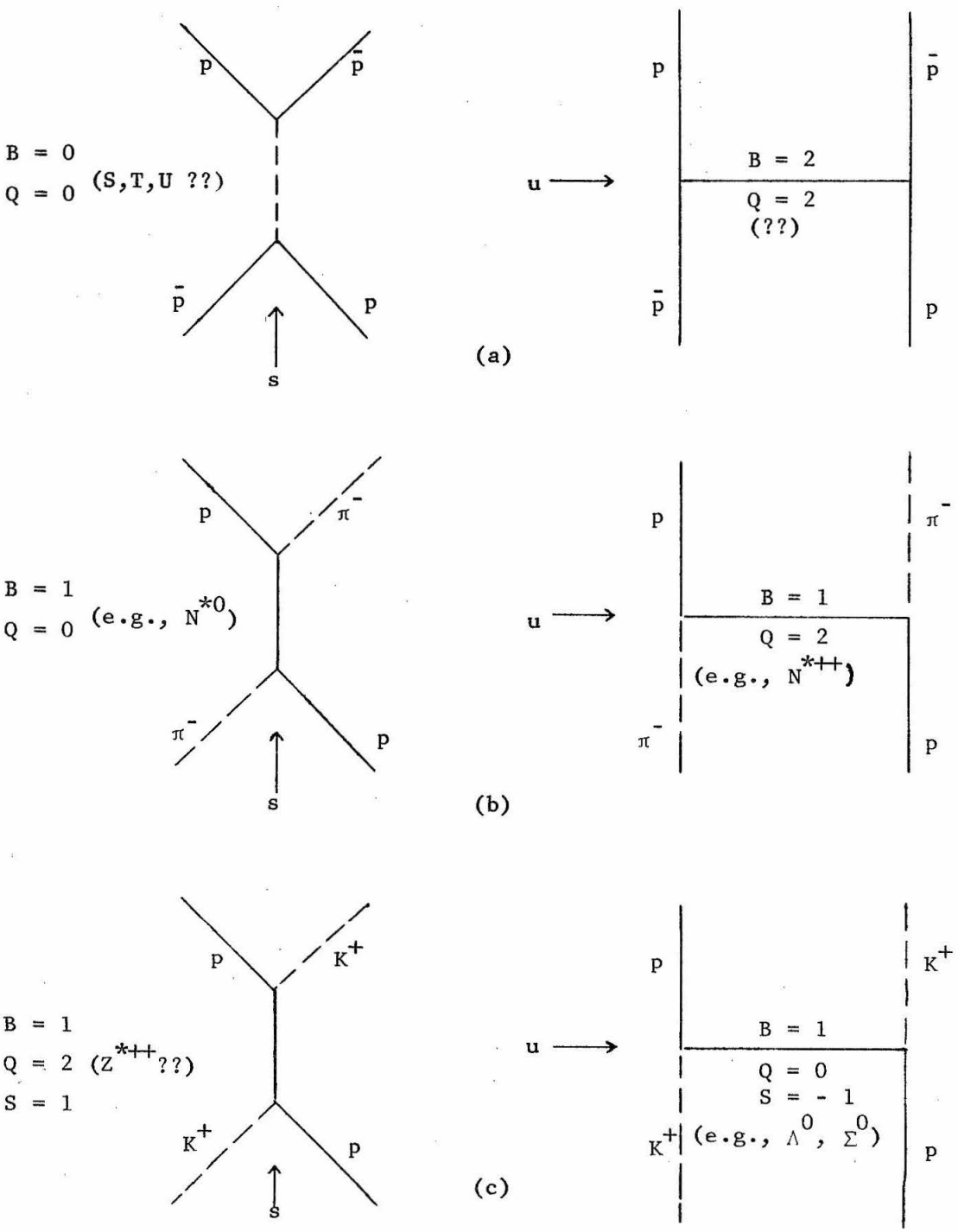

In $\pi^- p$ backward elastic scattering in the region 1.65 - 5.3 GeV/c[1.4], the dcs at 180^o, shown in Figure 1.2, revealed many sharp structures. For example, there are sharp bumps at 1688 and 1924 and a sharp dip at 2190, all of these can be attributed to resonance effects in the direct s channel. Indeed, this set of data was useful in indicating the properties of the resonances as well as suggesting possible existence of a new resonance at 3245 MeV. In the backward elastic differential cross section of other processes, it is possible to see similar structures in the event of strong resonance contribution from the s channel.

u channel effects may also be important in the backward elastic region. In the event that strong s channel and background contributions are absent, the u channel contribution, if it is dominated by a single (or an exchange degenerate set of) Regge trajectories, produces a backward elastic dcs ($d\sigma/du$, in this case) which has energy and angle dependence of $s^{2\alpha(u) - 2}$ [1.5] where $\alpha(u)$ is the function corresponding to the dominant trajectory. Thus, the $d\sigma/du$ at $u = 0$ would have a s^{-a} dependence where $a = 2 - 2\alpha(0)$. At a particular s, $d\sigma/du$ as a function of u shows an $e^{b\alpha(u)}$ dependence where b is $2\ \ell n(s)$. These behaviors are shown by $K^+ p$ backward scattering; we have plotted the $d\sigma/du$ near 180^o of $K^+ p$ scattering as a function of s in Figure 1.3a and the slope of $d\sigma/du$ in Figure 1.3b[1.6]. The data indicate that the dcs is consistent with the hypothesis that it is dominated by the Λ_γ (and/or the Λ_α, in case of exchanging degeneracy) trajectories. In this particular case, there are good reasons to suspect that u channel effects may dominate since the s channel is an exotic channel[1.7]

Figure 1.2: Plot of $d\sigma/d\Omega$ against incident π^- momentum (laboratory) for $\pi^- p$ elastic scattering at 180°. The positions and properties of the N* resonances are shown. The line drawn is a free hand curve of the data. The error bars are statistical. From Kormanyos et al., Phys. Rev. 164, 1661 (1967). See this article for the source of other data points.

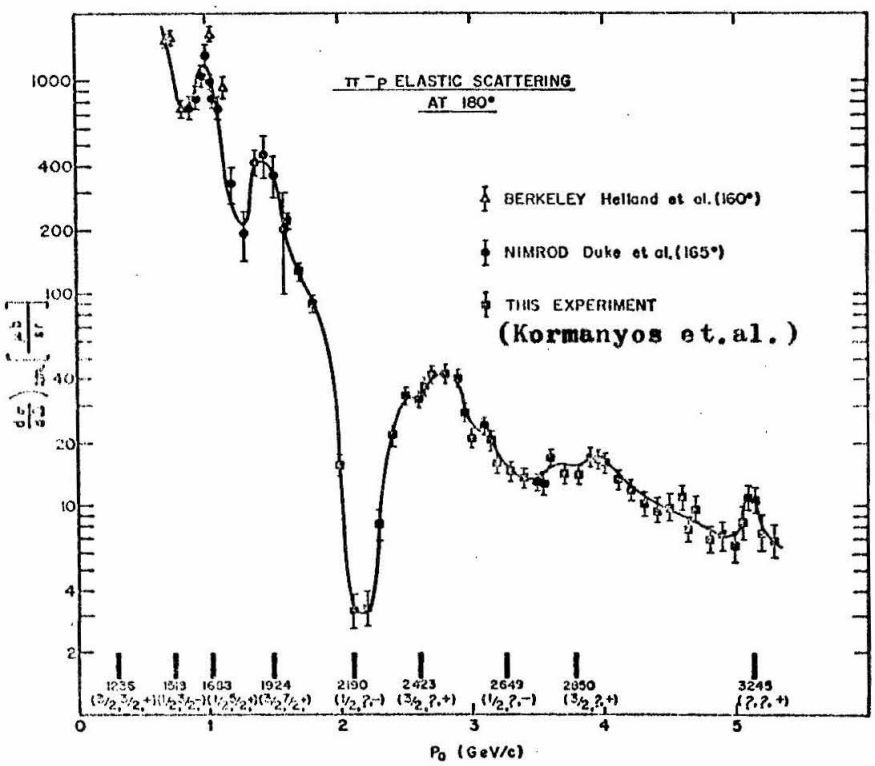

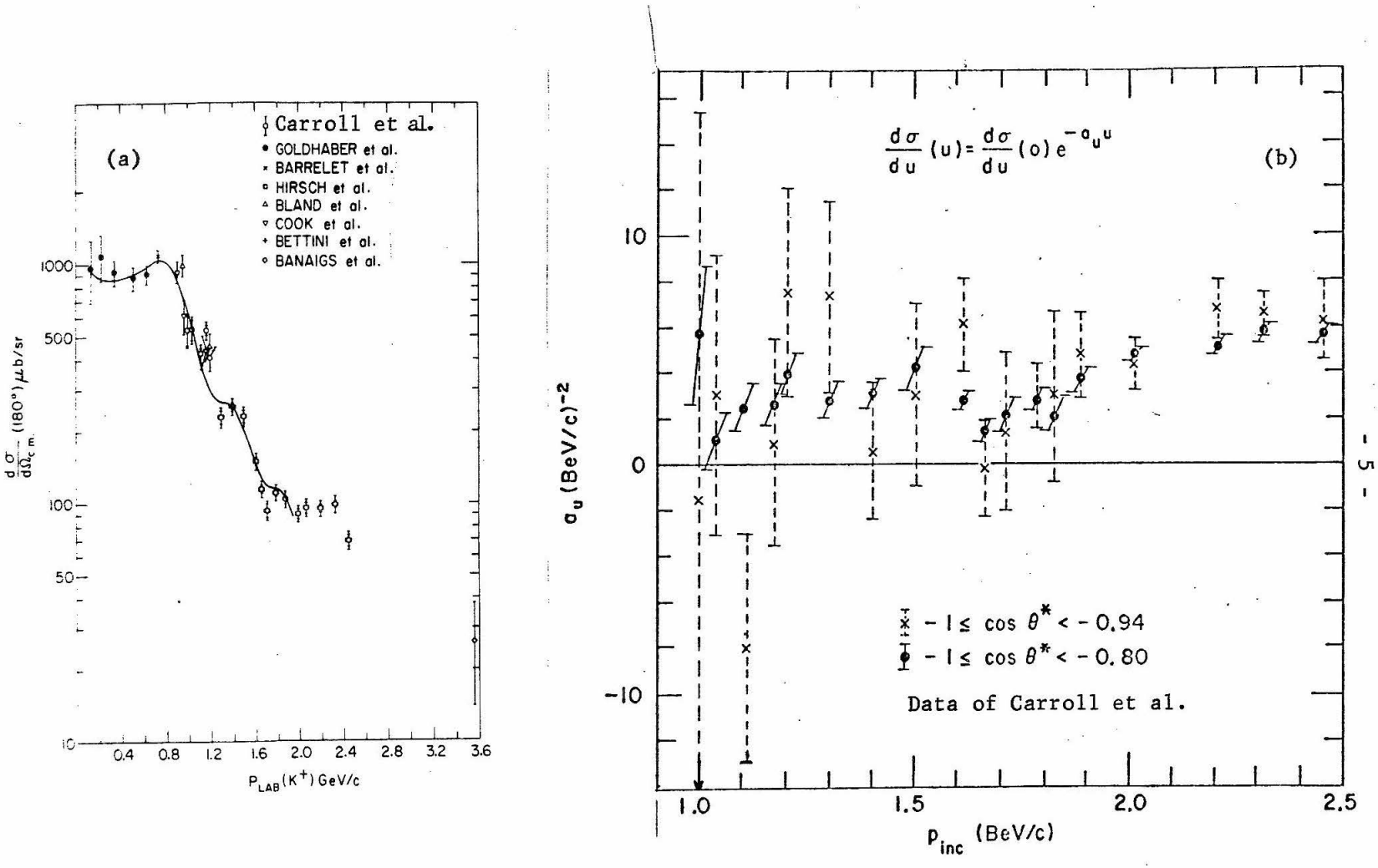

Figure 1.3: K^+p backward elastic scattering (a) dcs and (b) slope near 180°. For the sources of the data, see Ref. 1.6.

and thus its contribution to the scattering is not expected to be dominant.

$\bar{p}p$ backward scattering exhibits many features which do not occur for either $\pi^{\pm}p$ or $K^{\pm}p$ backward scattering since (1) the s channel has B = 0 instead of B = 1, and (2) the u channel requires an exchange of B = 2 and Q = 2. Many massive (with mass greater than 2 proton mass) B = 0 non-strange mesons have been indicated by previous experiments[1.8]. In addition, there exist theories which require the existence of such mesons[1.9]. It is expected that $\bar{p}p$ may couple to some or all of these resonances in the s channel if they exist. Thus, $\bar{p}p$ backward elastic scattering is a sensitive probe of such resonances. It is hoped that the coupling may be strong enough so that features similar to those seen in $\pi^{-}p$ backward scattering may also be observed in $\bar{p}p$ backward scattering. As far as the u channel effects are concerned, no B = 2 and Q = 2 resonance has been observed or indicated in experimental data. Therefore, it is likely that no distinct characteristics indicative of u channel dominance would be observed. It is therefore likely that the s channel effects, if any, are easier to observe. On the other hand, if there are significant contributions from the u channel, $\bar{p}p$ backward elastic measurements are sensitive to it.

It is thus interesting to obtain $\bar{p}p$ backward elastic scattering data over a fairly wide range of energies as well as a wide enough range of angles in order to extract the backward slope. We have measured the $\bar{p}p$ elastic scattering differential cross section with 10-20% statistical accuracy in the momentum range 0.7 to 2.37 GeV/c

incident $\bar{p}$ momentum (corresponding to the center-of-mass energy in the range 1.99 to 2.56 GeV). At each momentum, we obtain 5 to 7 angular data points with cos θ_{cm} between - 1.0 to about - 0.88. Preliminary results have been published[1.10].

This experiment, performed at the AGS partially separated beam 5 in Brookhaven National Laboratory during the fall of 1968, is a missing mass spectrometer experiment using a 37.5 cm long liquid hydrogen target, several counters and twelve wire spark chambers with digitized magnetostrictive readouts. We were able to measure the differential cross sections of $\bar{p}p$ annihilation into two charged mesons at extreme angles[1.11] simultaneously using essentially the same apparatus. Part of our apparatus was used previously for backward pi and K scattering on protons[1.12].

This experiment was performed by a collaboration of members from three institutions:

California Institute of Technology

Barry C. Barish, Howard Nicholson, Jerome Pine, Alvin V. Tollestrup and John K. Yoh (the author)

Brookhaven National Laboratory

Alan S. Carroll and Robert H. Phillips (now at SLAC).

and

University of Rochester

Claude Delorme (now at the University of Madagascar).

Fred Lobkowicz, Adrian Melissinos, and Yori Nagashima (now at Caltech).

CHAPTER II: EXPERIMENTAL APPARATUS AND METHODS

a. Introduction and Experimental Layout

We wish to measure the dcs (differential cross section) of $\bar{p}p$ backward elastic scattering. Therefore, we need to have a beam of $\bar{p}$'s incident on some hydrogen and to count all the $\bar{p}p$ backward elastic scattering events inside a well determined angular region.

Many accelerators have beams of partially separated negative charged particles with sufficient momentum range which we wish to cover (about 1 - 2 GeV/c)[2.1]. We thus need a system to identify the $\bar{p}$'s in the beam as well as to determine the momentum, position and direction distributions of such incoming $\bar{p}$'s. The $\bar{p}$'s are incident on a liquid hydrogen target.

To identify the $\bar{p}p$ backward elastic scattering events, we have to look at the final state particles of such reactions. The recoil proton from a backward elastic event (we only consider the region of $\cos \theta_{cm}$ less than - 0.90 or so) carries away essentially all the momentum of the system. The final state antiproton is left with a momentum of the order of 100 MeV/c or less. Such an antiproton has a range in hydrogen of the order of 0.3 cm and thus is not able to get out of the target. The final state antiproton will very likely be stopped and annihilated in the target. The likely annihilation of the stopped $\bar{p}$ is not easily distinguishable from an annihilation of $\bar{p}$ in flight. Thus, the $\bar{p}$ from a backward elastic event will not be useful in identifying the event. All our information must come from the recoil proton.

We can (and will) use four criteria to determine whether a forward outgoing particle is a recoil proton from a backward elastic event -- (a) charge, (b) momentum, (c) velocity, and (d) topology. The charge and the momentum, along with the scattering angle which we obtain from topology of the event, allow us to select only those forward particles which satisfy backward elastic kinematics[2.2]. The velocity, in conjunction with the momentum, allow us to remove all forward pions and kaons[2.3]. The topology criterion allows us to remove all events with scattering not inside the target and all events with more than one large angle scattering[2.4].

We describe briefly our apparatus and their layout in the following paragraphs. We indicate inside parenthesis the relevant sections of this chapter where further detailed information is given.

Beam: Beam Transport

We use the short branch of the partially separated beam 5 at the AGS in Brookhaven National Laboratory[2.5]. Figure 2.1 contains a layout drawing of the beam transport system, which contains 7 quadrupoles, 3 dipoles, 2 electrostatic beam separators, 2 beam stops and a mass slit. A detailed description of this system is given in Appendix A.

Beam: $\bar{p}$ Identification and Counting

We use a system of aperture scintillation counters (S_1, S_2 and S_3), one differential Cherenkov counter[2.6] and (for low incident momentum only) a scintillation counter time-of-flight system to determine whether an incident particle is a $\bar{p}$ and also whether it will pass through the target. These counters, most of which are shown

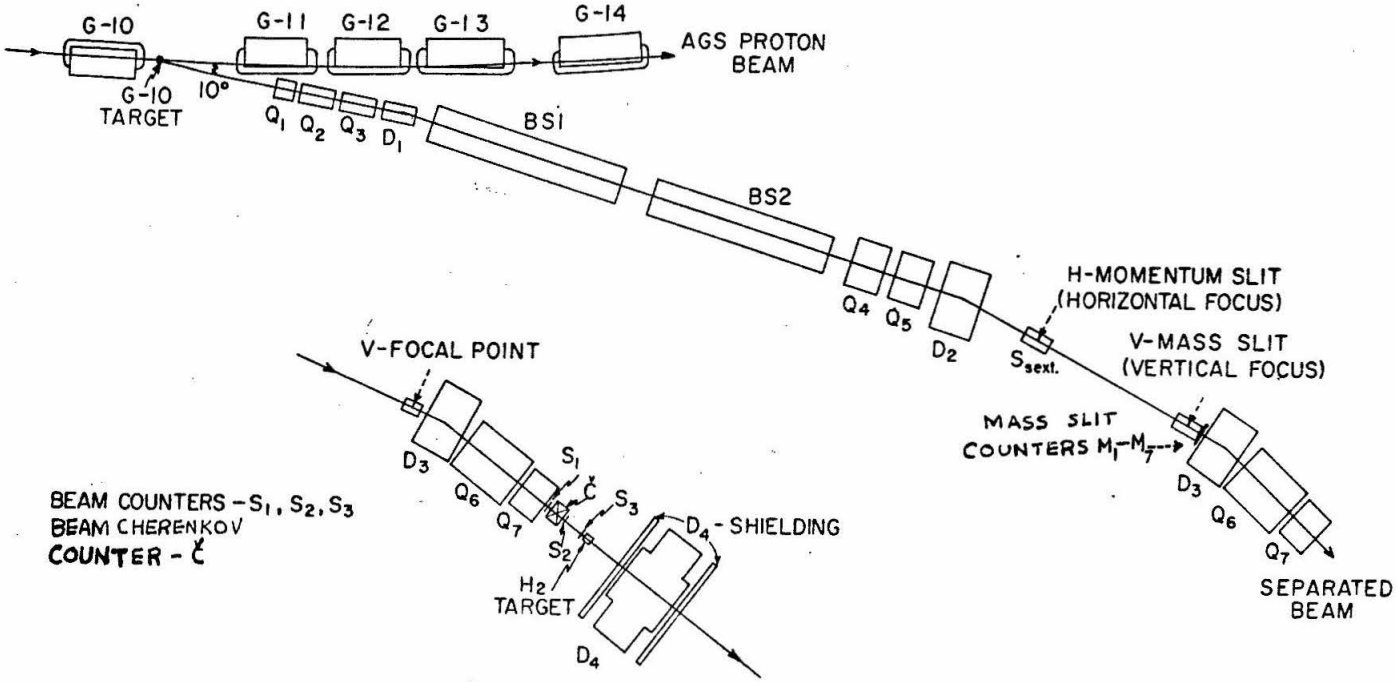

FIGURE 2.1

Layout of the separated beam transport system. Q_1-Q_7 are quadrupole magnets, D_1-D_3 are dipole magnets, S_{sext} is a sextupole magnet (not used), and BSI and BS2 are electrostatic separators. Also shown is the experimental area with the beam telescope, the Cerenkov counter (Č), the liquid H_2 target, and the large aperture, momentum analyzing magnet (D_4).

in Figure 2.2 (a figure of our entire apparatus), are discussed in detail in Section (b-i). A scaler system using the signals from these counters allows us to determine the number of useful $\bar{p}$ passing through our system.

Target

As shown in Figure 2.2, a 37.5 cm long liquid hydrogen target is situated just downstream of the S_3 counter[2.7]. The target, placed inside a vacuum box, is described in Section (b-ii).

Recoil Proton: Charge and Momentum Determination

In order to determine the charge and momentum of the forward particles, a large dipole bending magnet with gap 48" wide by 18" high is placed downstream of the target. To either side of the magnet (upstream and downstream) there are sets of 4 wire spark chambers with digitized magnetostrictive readouts[2.8]. These wsc (wire spark chambers) record the trajectories of passing charged particles. Thus, knowing the trajectories allows us to determine the charge and momentum of the forward particle. The details of this procedure are described in Section (b-iii). The characteristics of the wsc are described in Appendix B and the procedure for recording the particle trajectories is described in Section (d).

Recoil Proton: Velocity Determination

We use both a scintillation counter time-of-flight system and a threshold gas Cherenkov counter[2.9] to help us determine the velocity and hence (if we know the momentum) the type of particle going forward[2.3]. The time-of-flight system, described in Section (c-v), compares the time of arrival of the signals from the counter S_3 and

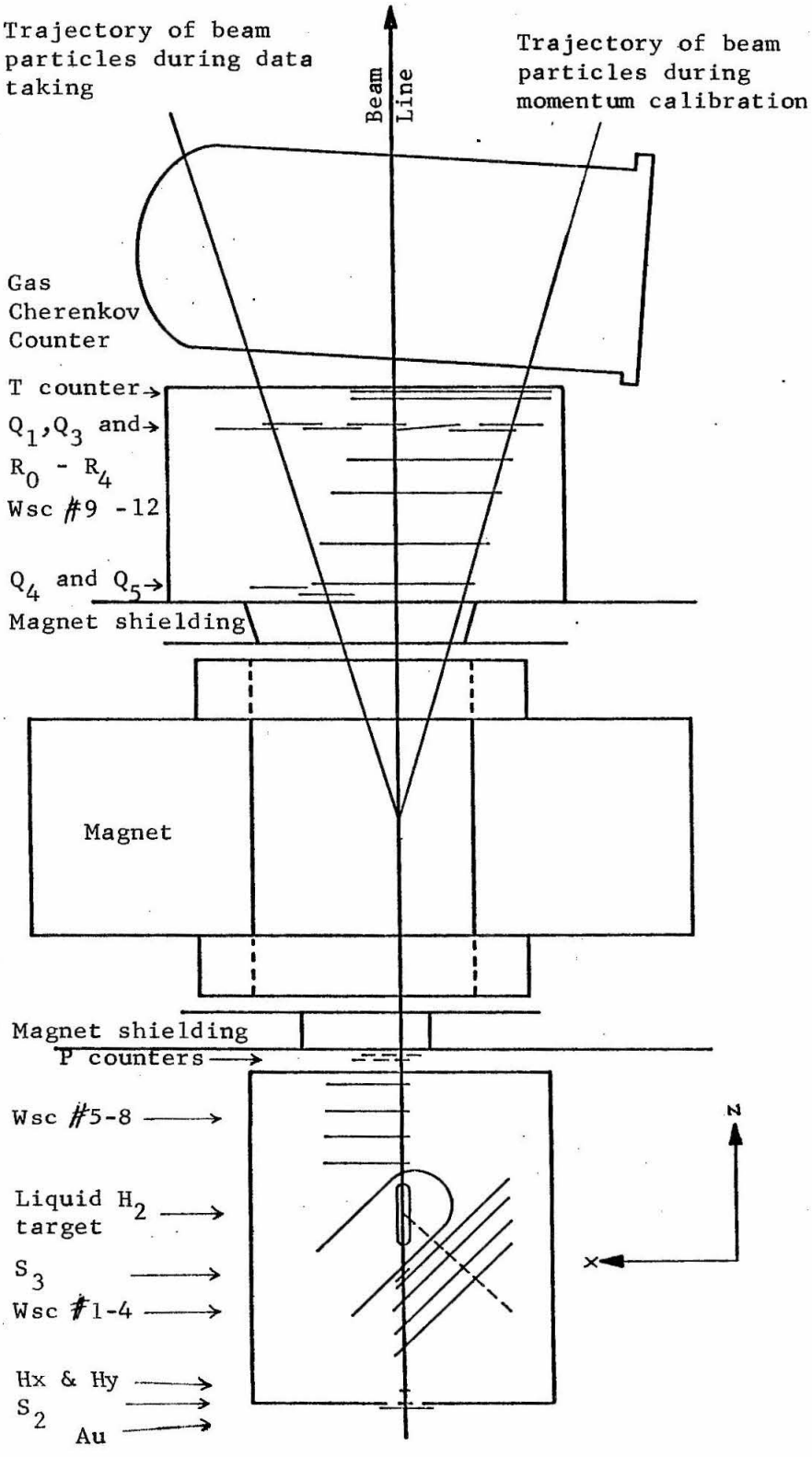

Figure 2.2 Layout of our Apparatus

from the set of counters T_1 - T_{10}. The Cherenkov counter, discussed in Section (c-iv), is placed downstream of all our other apparatus and has a threshold of 1.1 GeV/c for pions.

Recoil Proton: Topology of Event

In order to separate real events from background, we need to know that only one scattering has taken place. Hence, we need another set of four wsc upstream of the target. This allows us to determine the incident trajectory. This is also necessary so that we can obtain the scattering angle for the backward scattering and also obtain the distributions of position and direction for all incident $\bar{p}$'s to be used for the Monte Carlo of the acceptance of our apparatus.

Need for a Triggering System

The characteristics of the wsc (wire spark chambers) are that it can only be triggered a small number of occasions every beam pulse[2.10]. Since each beam pulse gives us of the order of 10^4 $\bar{p}$'s, we must use a triggering system to decide when we should trigger our wsc. Our triggering system contains three sets of counters P, R, and T (see Figure 2.2) and uses the $\bar{p}$ identification system as a coincident requirement. Only certain combinations of P and R counters which satisfy a loose momentum criteria will satisfy our triggering requirement[2.11]. Section (c-ii) describes this procedure in greater detail.

Event Recording System

Our analysis is not done on line. Thus, we must record the information on each event. We record wsc information and some counter information (along with the information on the velocity of the forward

particle from the time-of-flight system and Cherenkov counter) on magnetic tapes to be processed off line. This procedure is given in detail in Section (d).

We conclude this chapter with a brief assessment of our experimental apparatus and methods (Section (e)).

b. Beam, Target and Magnet

(b-i) Beam and $\bar{p}$ Identification and Counting

Beam 5 at the AGS in Brookhaven National Laboratory, which is described in Appendix A, supplies us with a collimated charged particle beam with a certain definite momentum acceptance and pion background. This beam is focused near the target. We must accept and count only $\bar{p}$'s which, if not scattered, will pass through the entire target. In addition, since the wsc (wire spark chambers) have memory time of the order of 1000 nsec, we would like to not count and use any $\bar{p}$'s which come within some specified period of time (500 nsec) of a previous particle. This enables us to reduce the amount of triggered events with spurious tracks[2.12].

We discuss each of these problems -- aperturing, $\bar{p}$ determination and spurious track reducing -- separately. All the position and sizes of the counters used for the beam system are given in Table 2.1.

Aperturing

We reject from consideration all particles which do not satisfy a three-fold coincidence S_1, S_2 and S_3 (defined as $S = S_1 * S_2 * S_3$). These circular scintillation counters are placed so that a straight line through all three counters automatically intersects all of the

Table 2.1: Beam Counters, Sizes, and Positions

A. Beam time-of-flight counters (M_1 - M_7). Also called the mass slit counters. 7 identical counters (scintillation).

size: 1-1/2" wide by 1/8" thick (height irrelevant)

pos : placed next to D_3 and behind the mass slit in the beam transport system (see Figure 2.1). They are in a vertical row with no overlap.

B. Beam aperture counters (S_1 - S_3) 3 scintillation counters.

	S_1	S_2
size:	3" round by 1/4" thick	2" round by 1/4" thick
pos :	(z)** at z = - 75"	at z = - 39"

S_3

3 - 1/8" by 2-1/4";* 1/8" t

at z = - 11-7/8"

(x,y) centered on beam line.

C. Beam liquid differential Cherenkov counter.

size of the radiator cell is 6" in diameter and 1/2 to 1" thick. position of radiator is centered on beam line and at a Z of about - 50".

D. Beam halo counter Au.

size: 12" by 22" (high) by 1/4" thick with a 2" round hole.

pos : the 2" round hole is centered on beam line at z = - 39-7/8".

E. Beam hodoscopes Hx_1 to Hx_4 and Hy_1 to Hy_4. 8 scintillation counters.

size: 1/2" by 2" by 1/4" thick.

pos : at z = - 35-3/4". Hx and Hy are arranged in vertical and horizontal non-overlapping rows centered on the beam line.

* S_3 is set at 45° to the beam line so as to present a circular aperture of 2-1/4" diameter to the beam.

** z = 0 at the center of the target. z is negative for upstream side.

target. (S_3 is actually oval due to the fact that it is 45^0 w.r.t beam line. This was necessary in order to place S_3 as close to the target as possible. Nevertheless, it presents a circular aperture normal to the beam line.) We will now equate a beam particle with a count in S.

$\bar{p}$ Identification

Two systems are used in identifying the $\bar{p}$'s in the beam.

1. Liquid Differential Cherenkov Counter[2.6]

A schematic cross-sectional drawing of the liquid differential Cherenkov counter is shown in Figure 2.3. The two lines -- the dash line and the dot-dash line, illustrate the operation of this counter. The movable diaphragm mirror is adjusted so that Cherenkov radiation from a $\bar{p}$ would strike the C bank of photomultiplier tubes while radiation from a pion would strike the $\bar{C}$ bank. The difference in radiation angle is due to the fact that pions of the same momentum are much faster than $\bar{p}$'s and thus have a larger Cherenkov angle.

Figure 2.4a contains a plot of the proportion of coincidences from the Cherenkov counter for each S as a function of diaphragm mirror position setting at a typical momentum. At the setting towards the left, the pion radiation strikes C's; at the right, the counter is sensitive only to $\bar{p}$. The $\bar{p}$ peak is at least a factor of 20 higher than the dip between the $\bar{p}$ peak and the pion peak giving evidence that much less than 5% contamination of pions underneath the $\bar{p}$ peak is expected. Checks show that typical pion contamination is in the 0.5% level. Efficiency for $\bar{p}$'s is better than 90% near 2.0 GeV/c.

Figure 2.3: Schematic drawing of the beam liquid differential Cherenkov counter. The C's are the coincidence signal and the $\bar{C}$'s are the veto signal. All scales are approximate.

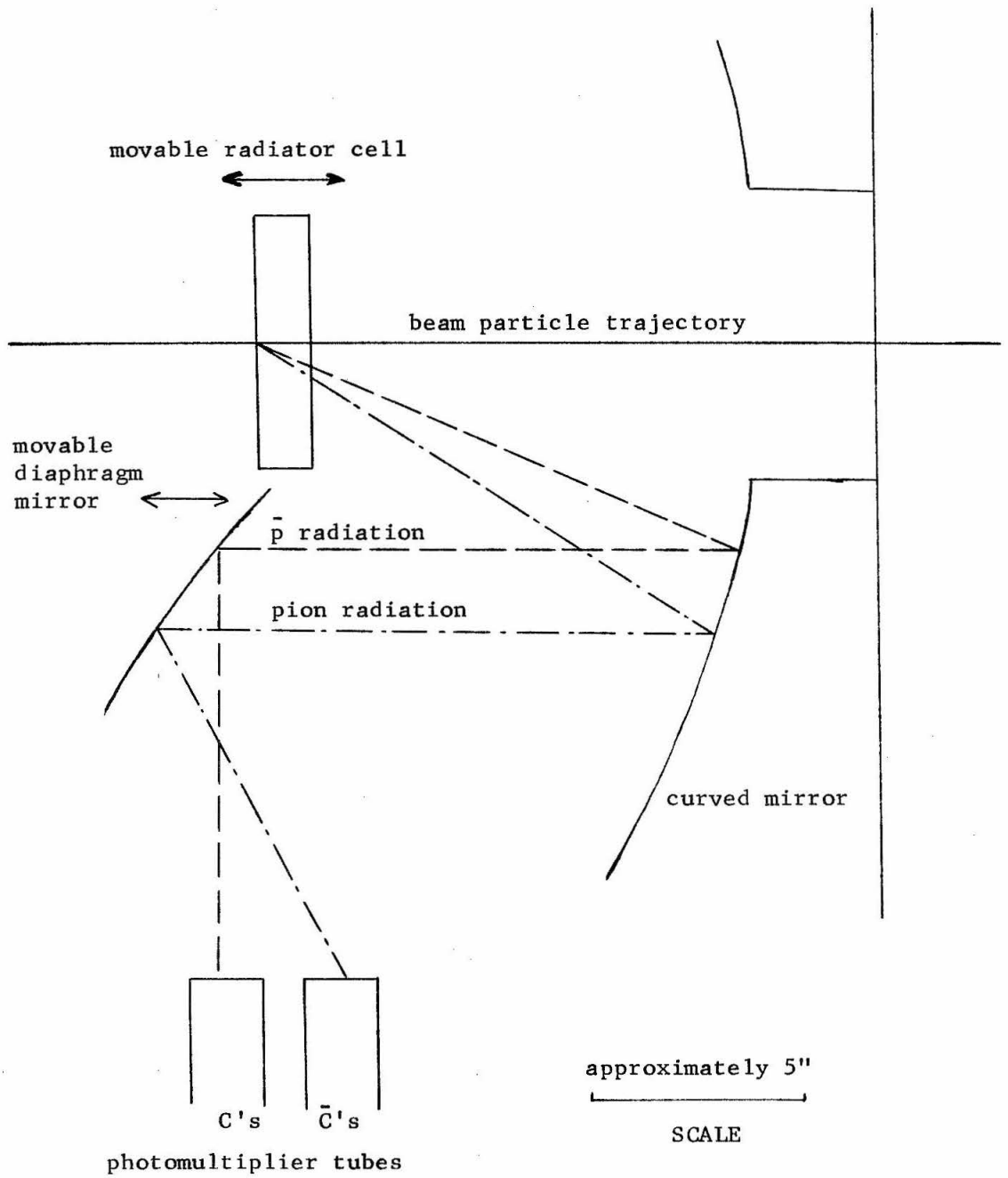

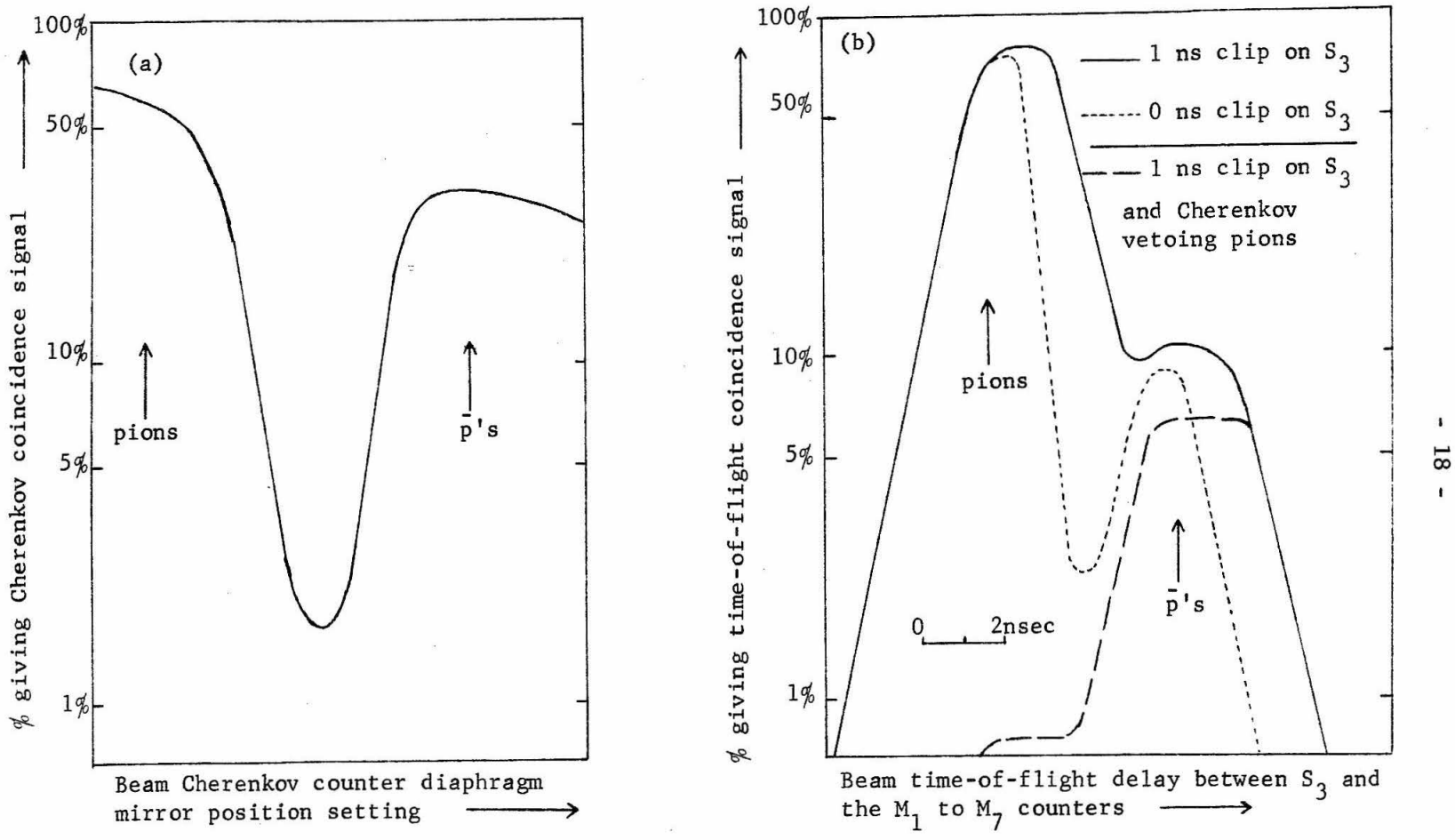

Figure 2.4: (a) % of Cherenkov coincidence vs. diaphragm mirror position. If, in the Figure 2.3, the diaphragm mirror moves to the left, the C's would then receive the pion radiation. (b) % of beam time-of-flight coincidence vs. time-of-flight delay.

The liquid differential Cherenkov counter is adequate in identifying $\bar{p}$'s and rejecting pions above 1.0 GeV/c. However, below 1.0 GeV/c, the efficiency in counting $\bar{p}$'s deteriorates. Thus, we use the Cherenkov counter to count (and reject) pions along with using a time-of-flight system described below.

2. Beam Time-of-Flight System

A set of 7 counters[2.13] (called the mass slit counters since they are placed next to the mass slit in the beam transport system -see Figure 2.1) about 14' upstream of the target is used in conjunction with the S_3 counter to give us a time-of-flight measurement of the velocity of the beam particles. Below 1.0 GeV/c, the $\bar{p}$ has a β of about 0.7 while the pion has a β of about 1.0. Thus, the difference in time-of-flight is about 4 nsec. Figure 2.4b shows the response as a function of time delay. The solid and dotted lines are the response for the time-of-flight system alone while the dashed line is the combined response of the time-of-flight with the Cherenkov counter set to reject pions. Again, we see that the pion background underneath the $\bar{p}$ peak is reduced to the 1% level. Notice that we clip the S_3 signal with a 1 nsec cable to give us a broader peak.

Reduction of Spurious Tracks in the wsc

We use a pile-up system to reduce spurious tracks in those events which we record. The beam halo counter A_u (see Figure 2.2) is situated next to S_2 and the two counters count all the particles in the beam. When either of these counters register a count, a pile-up gate is triggered which prevents any following particles to be counted within 500 nsec. This gate, which typically reduces the

amount of usable beam by 10-20%, cannot however, entirely cure the multiple track problem since the trigger system takes about 300 nsec to fire the wsc. Any particle which arrives between the backward elastic event and the firing of the chamber will be recorded along with the backward elastic event.

To help us decide which track belongs with the backward elastic event, two arrays of 4 2" by 2" wide and 1/4" thick scintillation counters called the beam hodoscopes are arranged in horizontal and vertical rows. The signals from these counters are used in the analysis. Any track which extrapolates into a counter which did not fire is removed in case of multiple tracks. This procedure is necessary only for a small percentage (of order of 1%) of all events.

Scaler Counting System

Our wsc impose a dead time of 20 msec each time they are triggered[2.14]. All $\bar{p}$'s satisfying our aperture and pile-up criteria which arrive during the time in which we are sensitive to backward elastic events must be counted. We use a series of logic modules (Chronetics 100 series -- 100 megacycles[2.15]) and scalers to count $\bar{p}$'s. In addition, several other beam quantities such as S (the beam particles, not necessarily $\bar{p}$'s, satisfying aperture and pile-up criteria) are also counted in order to monitor beam quality.

Table 2.2 lists the momenta where data were taken, the total $\bar{p}$ flux at each momentum, typical S and $\bar{p}$ per pulse, pi/$\bar{p}$ ratio and trigger rate. Figure 2.5 shows the distribution of momentum, positions and directions of the incident $\bar{p}$'s at three typical momentum[2.16]. Note that the spread in the distribution is due to the

Table 2.2: Beam fluxes and rates for each momentum. The "Real" momentum is the actual average momentum at the center of the target. The rates per typical pulse corresponds to about 1.5×10^{12} circulating p's in the AGS. Runs labeled L are special runs with low bending magnet setting. Trigger rates are usually higher for these runs. In our final results, the data at 1.585 and 2.125 which has been marked with an * were combined to form the 1.59 and 2.155 data.

Momentum		Total $\bar{p}$ flux		S	$\bar{p}$	pi/$\bar{p}$	Trigger rate
Nominal (GeV/c)	Real (GeV/c)	(empty)	full	per typical pulse			per 1000 $\bar{p}$'s
		in millions					
0.68	0.703		7.0	8K	0.5K	15.0	1.10
0.77	0.812		9.1	20K	0.9K	21.0	1.05
0.89	0.873	(3.0)	20.0	13K	1.0K	12.0	1.00
0.92	0.935		9.5	33K	2.5K	12.0	1.05
0.97	0.987	(6.2)	54.2	46K	3.5K	12.0	1.00
1.09	1.115	(4.2)	29.8	26K	4.0K	5.5	1.00
1.34	1.338	(11.0)	38.8	24K	8.0K	1.9	1.05
1.45	1.447		43.0	24K	8.5K	1.8	1.15
1.585AH*	1.580	(7.5)	24.5	32K	11.0K	1.8	1.10
1.585AL*	1.580	(3.0)	15.8	32K	11.0K	1.8	1.30
1.585BH*	1.589		10.8	40K	16.0K	1.5	1.05
1.585BL*	1.589		4.4	40K	16.0K	1.5	1.30
1.585C*	1.596		7.9	26K	12.0K	1.1	1.15
1.585D	1.610		63.3	30K	11.0K	1.8	1.15
1.70	1.716		78.2	35K	13.0K	1.8	1.10
1.815	1.797	(7.0)	60.3	55K	22.0K	1.5	1.05
1.8	1.844		73.7	40K	15.0K	1.6	1.10
2.0	2.032		73.5	55K	22.0K	1.5	1.10
2.125H*	2.155	(10.0)	59.8	55K	28.0K	1.0	1.10
2.125L*	2.155		21.7	55K	28.0K	1.0	1.40
2.365	2.370	(10.5)	48.4	75K	45.0K	0.6	1.05

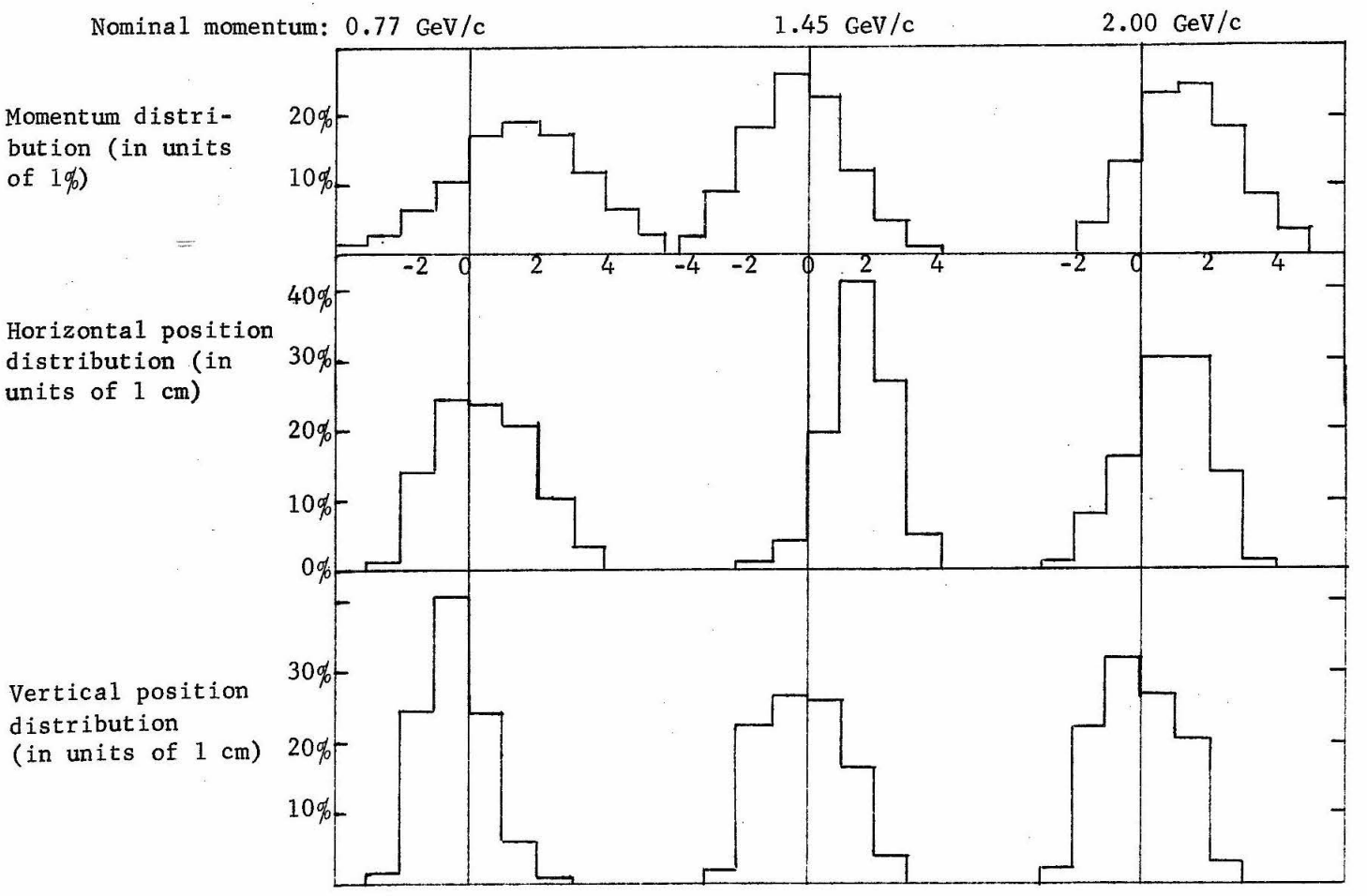

Figure 2.5: Distribution of momentum, positions and slopes of the incident $\bar{p}$ beam

Figure 2.5: (continuation)

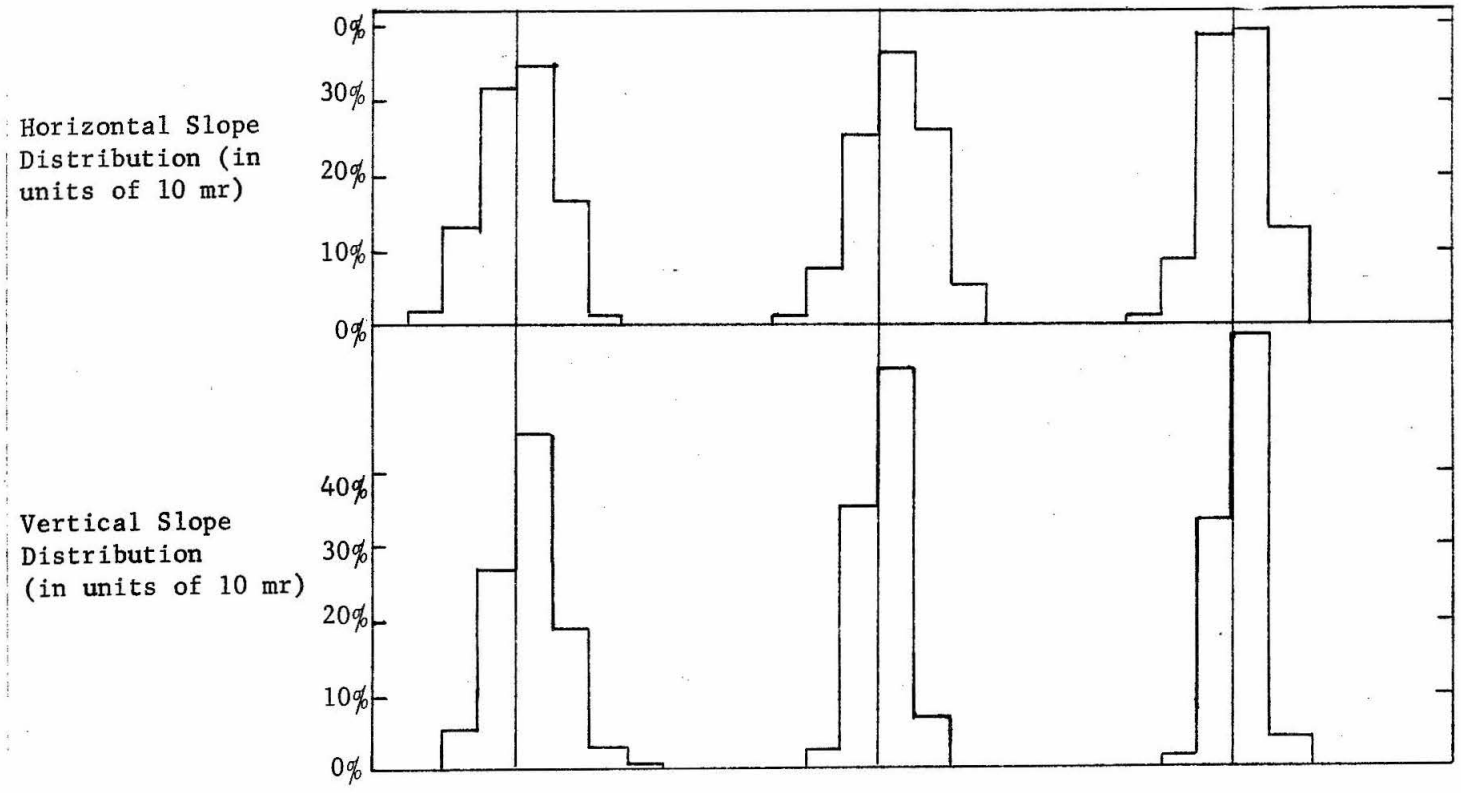

wsc resolution and multiple scattering in addition to the intrinsic properties of the beam[2.17].

Typically, we accept a momentum bite of ± 3% and keep the mass slit spacing narrow (about 1/8"). The total number of beam particles as measured by Au and S_2 per pulse is about 150 K. Since the beam pulse period is about 400 msec, this corresponds to a 0.3 megacycle rate. We have checked that this rate is tolerable since several data runs at a lower rate give answers which agree with the answer at the typical rate.

(b-ii) Target[2.18]

We use a cylindrical liquid hydrogen target 14-5/8" (37.2 cm) long and 3" (7.6 cm) in diameter. The target envelope is a single jacket of 14 mil mylar surrounded by 40 layers of 0.3 mil aluminized mylar acting as superinsulation. The target, shown in Figure 2.2, is housed in a vacuum box 15-3/4" wide set at 45^{o} to the beam line. The liquid hydrogen in the target is maintained at atmospheric pressure near the boiling point and has a density of 0.0708 gm/cm^3[2.19].

(b-iii) Magnet and Momentum Measurement

The magnet D_4 we use for momentum analysis is a 48D48 dipole magnet with an aperture 18" high by 48" wide. The useful aperture, however, is restricted by the hole in the magnet shielding which is 14" x 28" upstream and 16-1/4" x 46-1/4" downstream of the magnet. The size of these apertures is chosen such that any particle from the target which will go through all the wire spark chambers will not strike the shielding wall.

The shielding, an iron-wood sandwich[2.20] which contains iron layers of thickness 3/4", 1", and 6" is attached to either side of the magnet by long bolts and brackets. Its purpose is to minimize the stray field outside the gap of the magnet.

High stray fields would incapacitate both the magnetostrictive readouts of the wire spark chambers and the photomultiplier tube (even with shielding around it). Studies have shown that the magnetostrictive wire will not function with high transverse fields (of the order of 50 gauss) although longitudinal fields of up to several hundred gauss can be tolerated. Since the field inside the gap goes as high as 15 Kgauss, stray fields of 1% of the central field cannot be tolerated. In addition, the photomultiplier tubes, even with shielding, cannot withstand hundreds of gauss. Without any magnet shielding, the field at the beam line 50" from the side of the magnet is still about 1% of the field at the center of the magnet (i.e., about 100 gauss); the shielding reduces the field so that at the beam line 25" from the side of the magnet (just outside the shielding), the field is reduced to about 0.1% of the field at the center of magnet gap. Even then, the wire chamber readout wires of chambers 9-12 (downstream of the magnet) must undergo special treatment whenever we switch the polarity of the magnet (the wire must be re-magnetized and the pick-up amplifier must have its polarity switched also).

The momentum of the particle which goes through the magnet is obtained from the amount of bending obtained while traversing the magnet. The field at the interior of the magnet gap has been

obtained through the use of a nuclear magnetic resonance probe[2.21]. We then use the rectangle field approximation to calculate the momentum.

For a particular field B at the center of the magnet, we approximate the field by a vertical field B over a length L, the effective length which has been empirically determined to be[2.22]

$$L = 155.60 \text{ cm}/(1 + (B/255.51 \text{ Kg})^{0.99991}).$$

The momentum of the particle traversing the magnet is then

$$p = \frac{2.9978 \; B \; L(1 + x'^2 + y'^2)^{1/2}}{100(\sin \alpha + \sin \beta)(1 + x'^2)^{1/2}}$$

where x' and y' are the incident horizontal and vertical slope, α is the incident horizontal angle and β is the outgoing horizontal angle (see Figure 2.6a). Studies have shown that this formula is accurate to within 0.3%[2.22]. Figure 2.6 shows some of the geometry of the rectangle field approximation.

We can thus obtain the momentum of a particle at the magnet. To obtain the momentum at the interaction vertex, we simply correct for ionization losses.

In order to select backward elastic events using kinematics, we must have a good idea of the momentum of the incident $\bar{p}$. We calibrate the incident momentum by triggering on every $\bar{p}$ and changing the polarity of the magnet to bend negative instead of positive particles into the wsc downstream of the magnet. We do this momentum calibration for each of our momenta. The resultant distribution in momentum is typically that of Figure 2.7b.

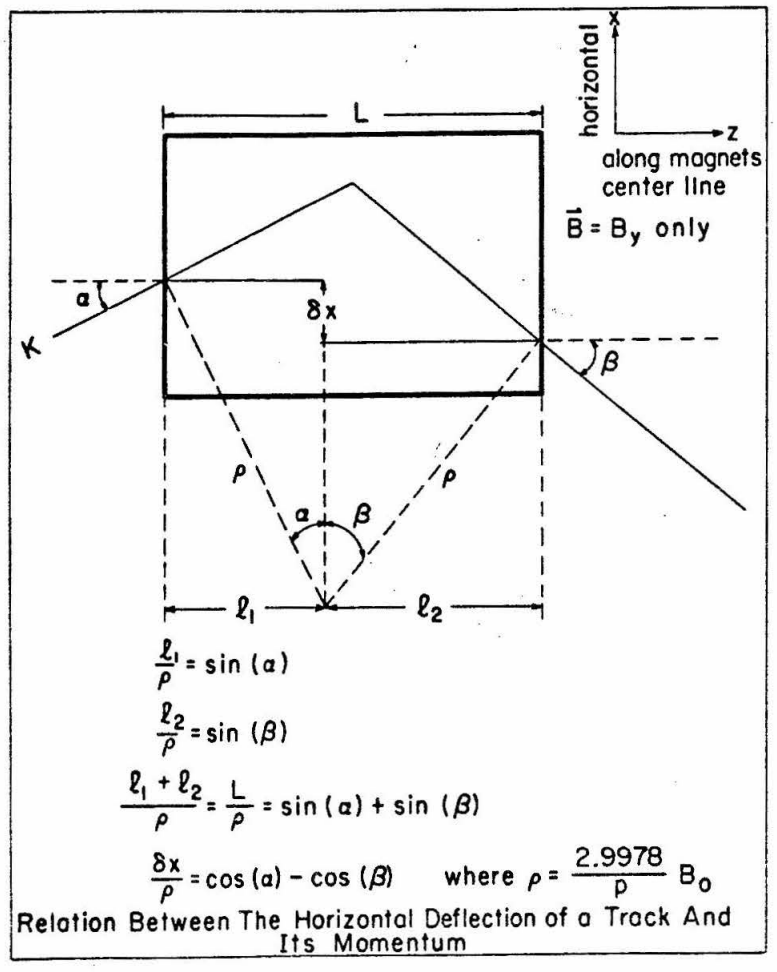

(a)

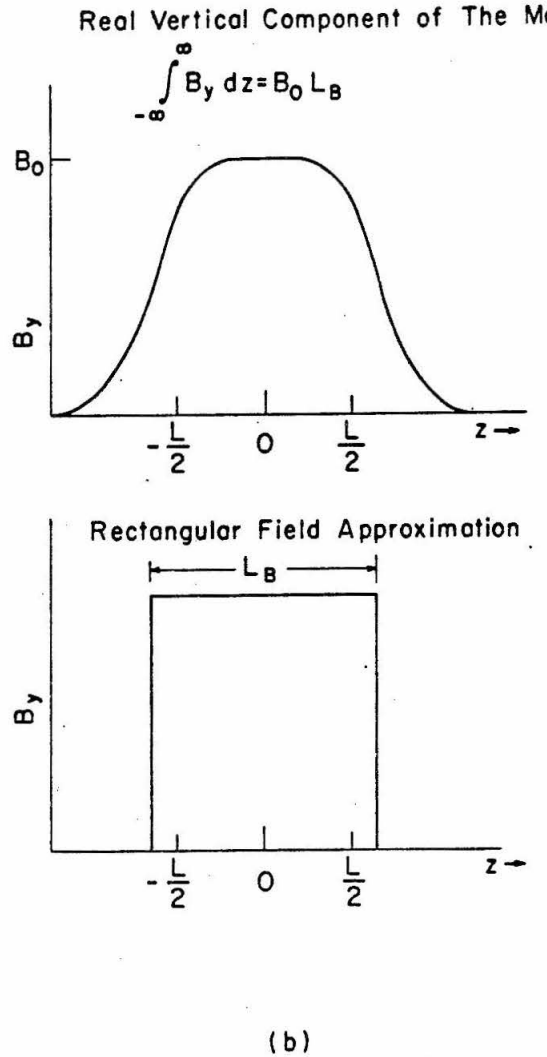

(b)

Figure 2.6

Rectangular field model for a dipole magnet.

It is possible to obtain a better estimate of the incident momentum by using the property of the beam transport system. Appendix A, which handles the beam transport system, indicates that at the mass slit, the horizontal (x) position of the beam is strongly correlated with the momentum -- particles with momentum higher than mean momentum tend to have positive x at the mass slit (see Figure A.1 of the Appendix A).

A set of 7-1/2" wide scintillation counters is placed vertically next to the mass slit[2.13]. The momentum distribution of $\bar{p}$'s hitting each mass slit counter is shown in Figure 2.7a. By combining the 7 distributions correcting for the shift in central momentum, we obtain a total distribution of Figure 2.7c instead of 2.7b for the same $\bar{p}$'s. Since the momentum spread in the distribution is also due to multiple scattering and the wire spark chamber resolution[2.23], the improvement in momentum determination is actually better than indicated. In any case, the FWHM is reduced from about 1.7% to about 1.0%.

c. Fast Counters and Logic

(c-i) Introduction

During each beam pulse, thousands of $\bar{p}$'s are incident on the target. We can record a maximum of 15 triggered events[2.24]. Also each time we trigger, the wsc (wire spark chambers) require a 20 msec dead time to allow us to record the event and to allow the wsc to recover. Thus, without losing any acceptable backward elastic events, we would like to trigger on as few events as possible. We use a trigger system of fast scintillation counters and fast logic

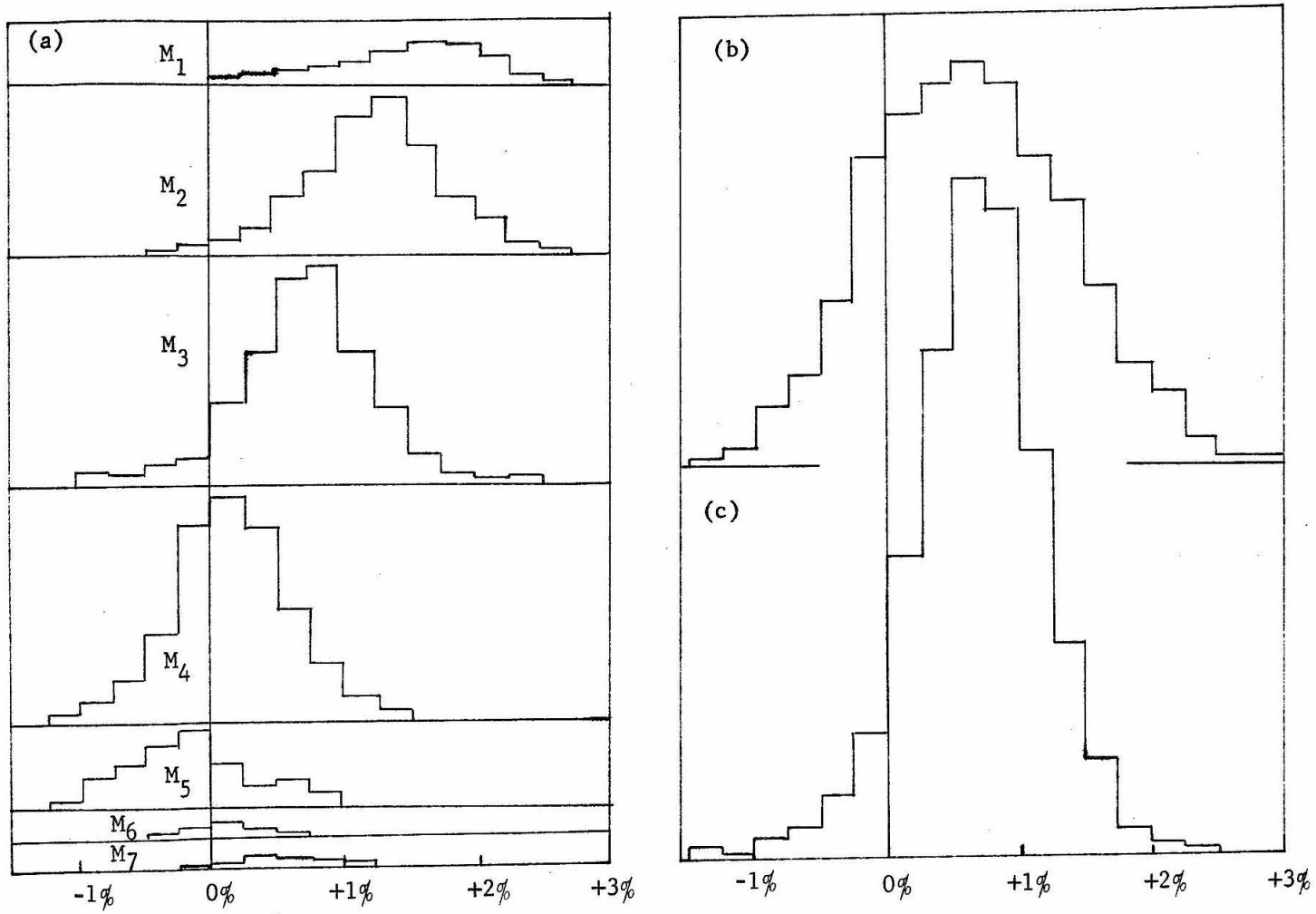

Figure 2.7: Momentum distributions of incident $\bar{p}$'s at 2.0 GeV/c nominal momentum for: (a) $\bar{p}$'s hitting a particular mass slit counter. (b) all $\bar{p}$'s. (c) all $\bar{p}$'s corrected according to which mass slit counter it hits.

modules[2.25] to test for the trigger condition. We are able to reduce the triggering to about 1 per 1000 incident $\bar{p}$'s. No backward elastic events are lost except for dead time. We will discuss the trigger condition, logic and rates in Section (c-ii).

Counter information is useful for analysis. For example, the knowledge of which counter registers a count for a particular event may be helpful in removing a spurious track. We record 48 binary bits for each triggered event. 35 of these bits which contain the counter and various coincidence information are discussed in Section (c-iii).

The other 13 bits contain information on the velocity of the forward particle essential to remove pion background underneath our recoil protons. This includes the information from the gas threshold Cherenkov counter (Section c-iv)) and a forward outgoing particle time-of-flight system (Section (c-v)).

(c-ii) Trigger Counters, Logic and Rates

Logic

We test for the trigger condition using a system of scintillation counters (listed under "non-beam counters" in Table 2.3 with their sizes and positions) and logic modules[2.25].

To satisfy our trigger condition, we require a coincidence of:

1. An incident $\bar{p}$. This is determined by the $\bar{p}$ identification system described in Section (b-i).

2. A forward outgoing positive particle with momentum close to that of the incident $\bar{p}$ and whose trajectory passes through the wsc (wire spark chambers). This condition is tested by the combination of three

Table 2.3: Non-Beam Scintillation Counter Sizes and Positions

Counter Name	Size x	Size y	Size z (thickness)	Position x	Position y	Position z
P_1	3"	7"	1/8"	- 4" to - 1"	- 3-1/2" to 3-1/2"	38-1/4"
P_2		same		- 1-1/2" to 1-1/2"	same	same
P_3		same		1" to 4"	same	same
P_4		same		3-1/2" to 6-1/2"	same	same
P_5		same		6" to 9"	same	same
P_6		same		8-1/2" to 11-1/2"	same	same
R_0	14"	24"	1/2"	- 30" to -16"	- 12-1/4" to 11-3/4"	175-3/8"
R_1		same		- 24-1/2" to -10-1/2"	same	same
R_2		same		- 14" to 0"	same	same
R_3		same		- 4" to 10"	same	same
Q_1		same		7" to 21"	same	same
Q_2		same		16-1/2" to 30-1/2"	same	same
Q_3		same		26-1/2" to 40-1/4"	same	same
Q_4	12"	22"	1/4"	9" to 21"	- 11" to 11"	139-1/4"
Q_5		same		19-1/2" to 31-1/2"	same	same
T_i (i = 1,3,5,7,9; non-overlapping)	5(7-3/8")	13-1/2"	1/4"	- 28-1/4" to 8-3/8"	- 10" to 3-1/2"	182-5/8"
T_j (j = 2,4,6,8,10; non-overlapping)		same		same	- 3-1/2" to 10"	same

counter hodoscopes P, R and T (see Figure 2.2, page 12). The P R combination is used to restrict the momentum acceptance of the forward particle. Figure 2.8 gives a plot of the horizontal position at the P counter plane (x_P) vs. the horizontal position at the R counter plane (x_R) for all particle trajectories. The area inside the solid line satisfies the triggering criterion in P and R. Dashed lines drawn in Figure 2.8 show the locus of points with the same momentum p coming from the center of the target.

T counters are required for triggering. This is used to reduce the aperture for triggering as well as to provide an additional coincidence requirement to reduce accidentals. Note that the T counters are also used for forward outgoing particle time-of-flight system.

3. An absence of a negative charged forward particle with essentially the incident beam momentum and slope. This is tested by a combination of P Q counters. This beam veto reduces the trigger rate by a substantial amount. Many mechanisms can be responsible for the large amount of incident $\bar{p}$ which satisfy condition 2 and yet have a forward negative charged particle with fairly high momentum. Two such mechanisms are a) $\bar{p}p$ annihilation into multi-pions in which one (or more) positive and one negative pion goes forward, and b) $\bar{p}p$ into $\bar{p}n\pi^+$ in which the momentum transfer to the $\bar{p}$ is small.

We have studied the possibility that a real backward elastic event is vetoed by this condition. Since the final state $\bar{p}$ will probably annihilate in the target, a forward pi minus giving a beam veto is possible. The conclusion is that there is a negligible loss

Figure 2.8: Triggering "area" in P-R space. x_p is the horizontal position of the trajectory in the plane of the P counters. x_R is the corresponding position in the plane of the R counters. Values of x_p and x_R inside this "area" implies that the event satisfies the P-R counter criterion for triggering. Lines show the loci of events from the center of the target with specified momentum.

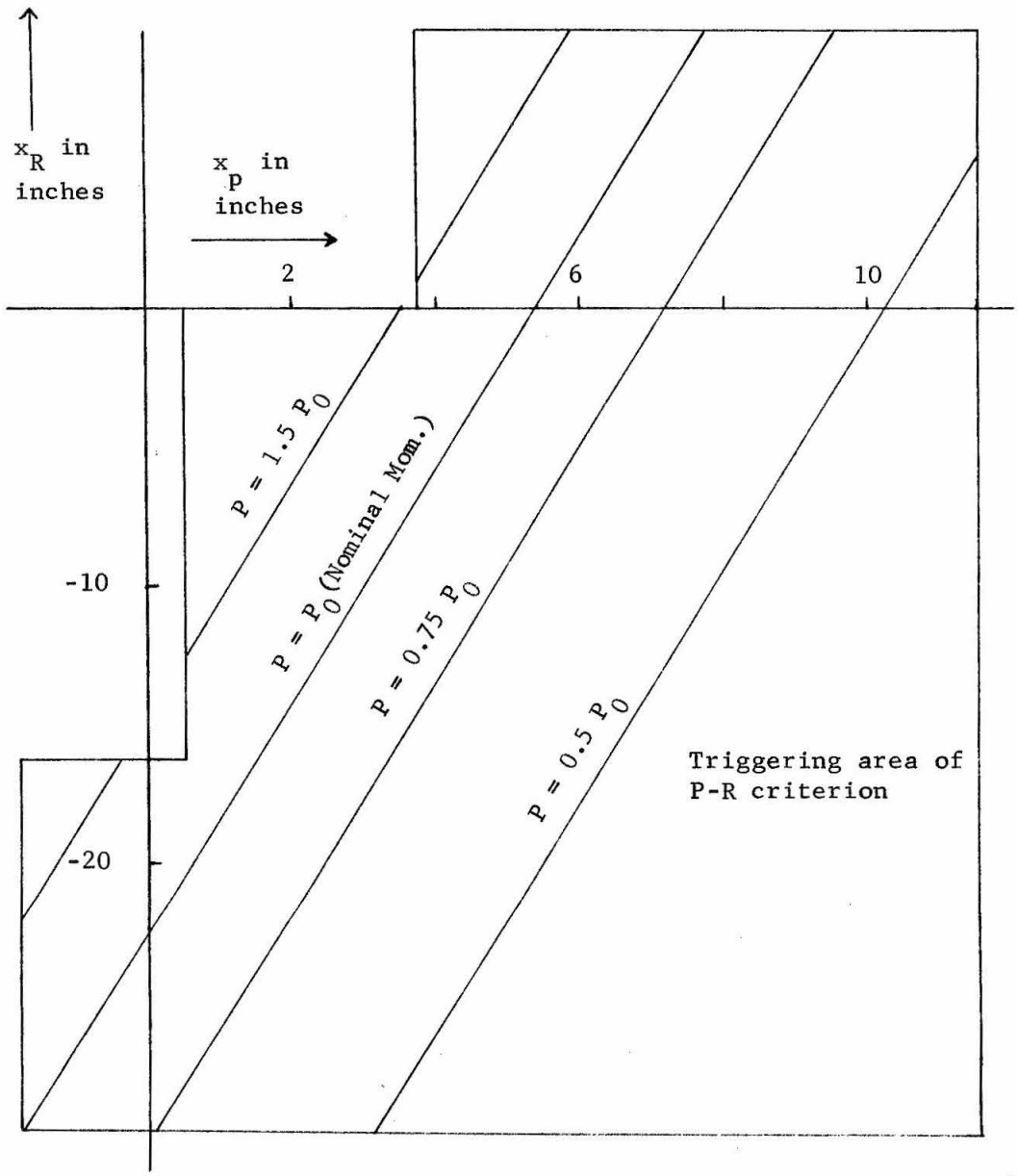

(see Section (d) in Chapter III).

Electronics

The trigger electronic logic system consists of a number of fast (100 megacycles) logic modules[2.25] used to identify, with a resolving time of about 10 nsec, the trigger condition. It also sends the trigger signal to the wsc pulsing system, the computer interface, and the master gate to generate a dead time during which the $\bar{p}$ counting system and trigger logic modules are inactivated. See section (d-iv) for further details on the operation of our recording system after the arrival of a trigger logic signal.

The logic of the trigger system is shown in Figure 2.9. Counter signals from the photomultipliers are shaped into standard pulses by discriminators (Chronetics 104[2.25]). These pulses are correlated to see if the trigger condition is satisfied. The modules with an x in the upper right-hand corner are those modules which are gated off by the master gate during the dead time. It is easy to see that without these particular modules, no $\bar{p}$ can be counted and thus no further trigger can be accepted.

Rates

The rates for triggering at each momentum is shown in Table 2.2. It is about one trigger per thousand incident $\bar{p}$.

Even though the trigger rate is only about 0.1%, the number of events which satisfy the trigger condition is still rather large since the average flux of $\bar{p}$ per pulse is as high as 45K. At incident momentum of 1.5 GeV/c or higher, this rate is intolerable. If we accept an average of 14 trigger per pulse, we have 280 msec of dead

Figure 2.9: The trigger logic flow chart (modules which are gated off by the master gate are shown with an x in the upper right-hand corner; veto enters through the side).

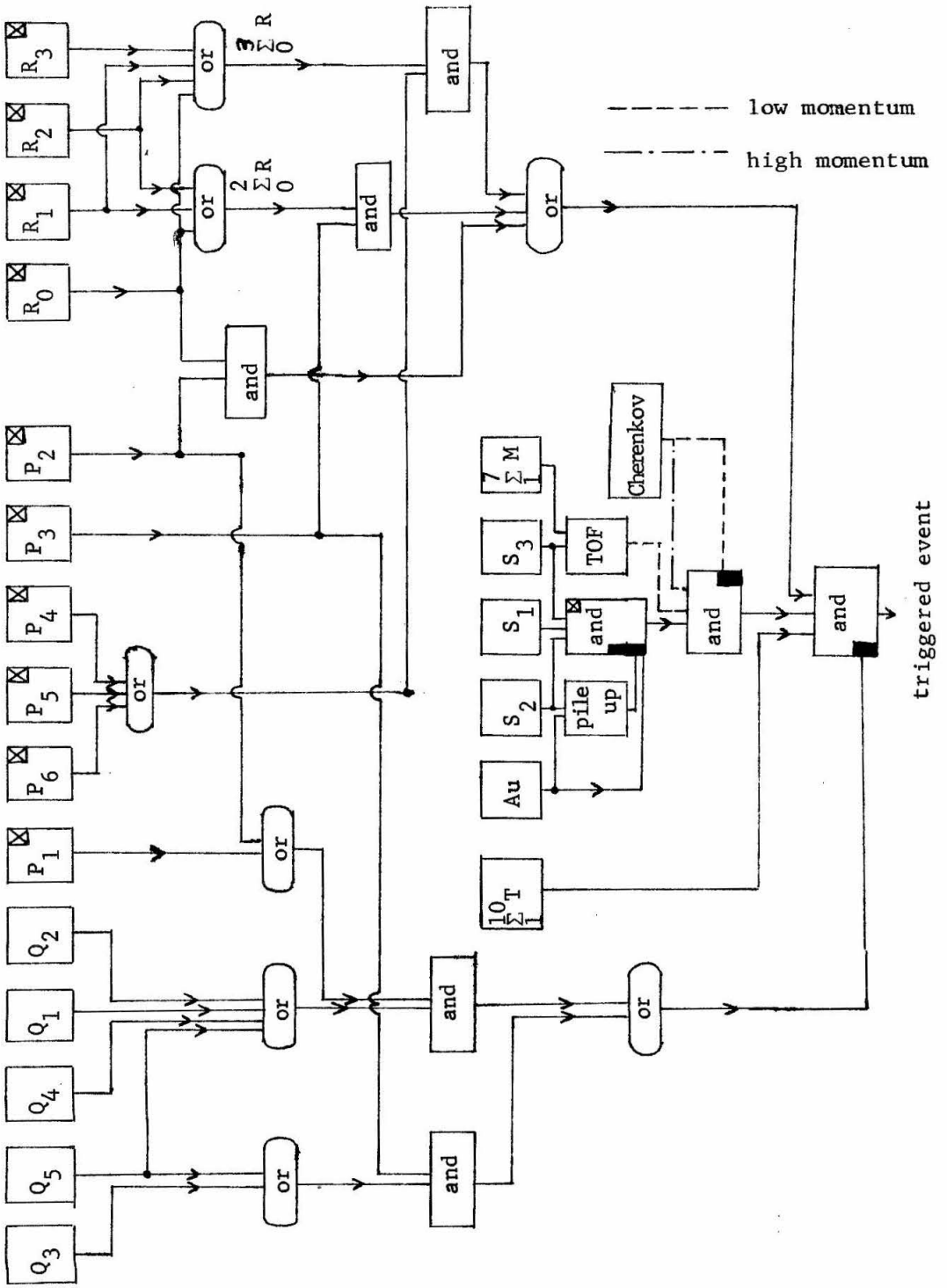

time. Since each beam pulse lasts only about 400 msec, we are only able to use 1/3 of the beam! It would be useful to reduce the trigger rate further since the actual number of backward elastic events is only about 1% of all the triggered events.

Several possibilities can be considered:

1. The (PR) triggering area (see Figure 2.8) can be reduced. We can use fewer combinations of P and R counters in our trigger. This would narrow our momentum acceptance. Due to the finite size of the target and counters, the maximum reduction possible without losing any backward elastic events is less than 1/3.
2. We could use the gas Cherenkov counter (see Section (c-iv)) to veto all events which give a pulse since recoil protons are below threshold for this counter. However, the reduction is only 15%. Most of the triggers are apparently due to low momentum protons or pions below the threshold for the Cherenkov counter.

Thus, it is possible to reduce the trigger rate by about 40%. We did not do it since the gain is not too significant[2.26] and also since we are interested in measuring $\bar{p}p$ going into pi + missing mass, K + missing mass or p + missing mass[2.27].

Another possible way to reduce trigger rate is to use the time-of-flight system. However, at high momentum, our system is not good enough to separate forward pions from forward protons.

(c-iii) "Counter Bits"[2.28] -- Scintillation Counter Information for Analysis

Digital counter information for each event is useful both in

analysis and in the efficiency calculation of the counters. We cover these uses in the appropriate section in the analysis chapter.

35 of the 48 available bits record the information of whether one or a combination of counters fired. The remaining 13 bits record the information from the gas Cherenkov counter and the forward outgoing particle time-of-flight system (see the next two sections).

Briefly, the counter bits work as follows. Counter signals are delayed and timed to arrive at the counter bit modules just after they receive the interface signal after each trigger (see d-iv). The counter bit modules remain receptive for a duration of 50 nsec. The arrival of a counter signal during this period will flip the module. The modules are then read by the interface and the information is written onto magnetic tape. The modules are then reset to await the arrival of the next triggered event.

(c-iv) The Gas Threshold Cherenkov Counter

One of the two systems we used to measure the velocity of the forward particle is the Gas Threshold Cherenkov counter[2.9]. This counter is a large 4' diameter aluminum cylinder 8' wide (see Figure 2.2 for the position of this counter) containing Freon-12 gas under about 8 atmospheres (about 120 psi) pressure as a Cherenkov radiator. The refractive index of this gas under this pressure is about 1.009. Pions with momentum above 1.1 GeV/c will Cherenkov radiate in this medium. The corresponding threshold for K's and p's are 3.5 and 6.5 GeV/c, respectively. Since such high momentum particles are kinematically impossible to produce for our incident momentum, we

assume that any time we receive a coincidence from this counter, a pion has passed. Although a high energy proton or kaon could in principle produce a pion with sufficient momentum to trigger this counter, this is expected to be rare[2.29].

Figure 2.10 shows a cross-sectional view of this counter and also demonstrates how this counter works. Note that the photomultiplier tubes sit at the top of the counter and thus they are not in the particle's path. Hence, we do not need to worry about Cherenkov radiation in the quartz window of the counter or the glass windows of the photomultipliers. Not shown in the figure are the heating coils necessary to keep the whole counter above 40°C. This is necessary in order to prevent the Freon-12 from condensing[2.30].

Although the counter is a cylinder 4' in diameter, the useful radiation distance, due to the placement of mirrors, is typically about 25". A total of about 50 photons are produced. (The Cherenkov radiation is focused by the curve-mirror and flat-mirror system into an area covered by light pipes.) Our phototubes[2.31] have about 10% quantum efficiency. Thus, an average of 5 photoelectrons are produced. The resultant signal from the photomultipliers are mixed and fed into a 64-channel pulse height analyzer. The output is recorded in 6 binary bits of the counter bits. Figure 2.11a shows a typical pulse height distribution for forward particles near the incident momentum. Figure 2.11b shows the portion of the events in 2.11a which are tagged as pi's by the time-of-flight system discussed in the next section. The cut we usually use is shown as an arrow. All events above this arrow are usually discarded.

Figure 2.10: Schematic drawing of the gas threshold Cherenkov counter. The dashed lines are rays of Cherenkov radiation from a particle with velocity above threshold (about 1.1 GeV/c for pions).

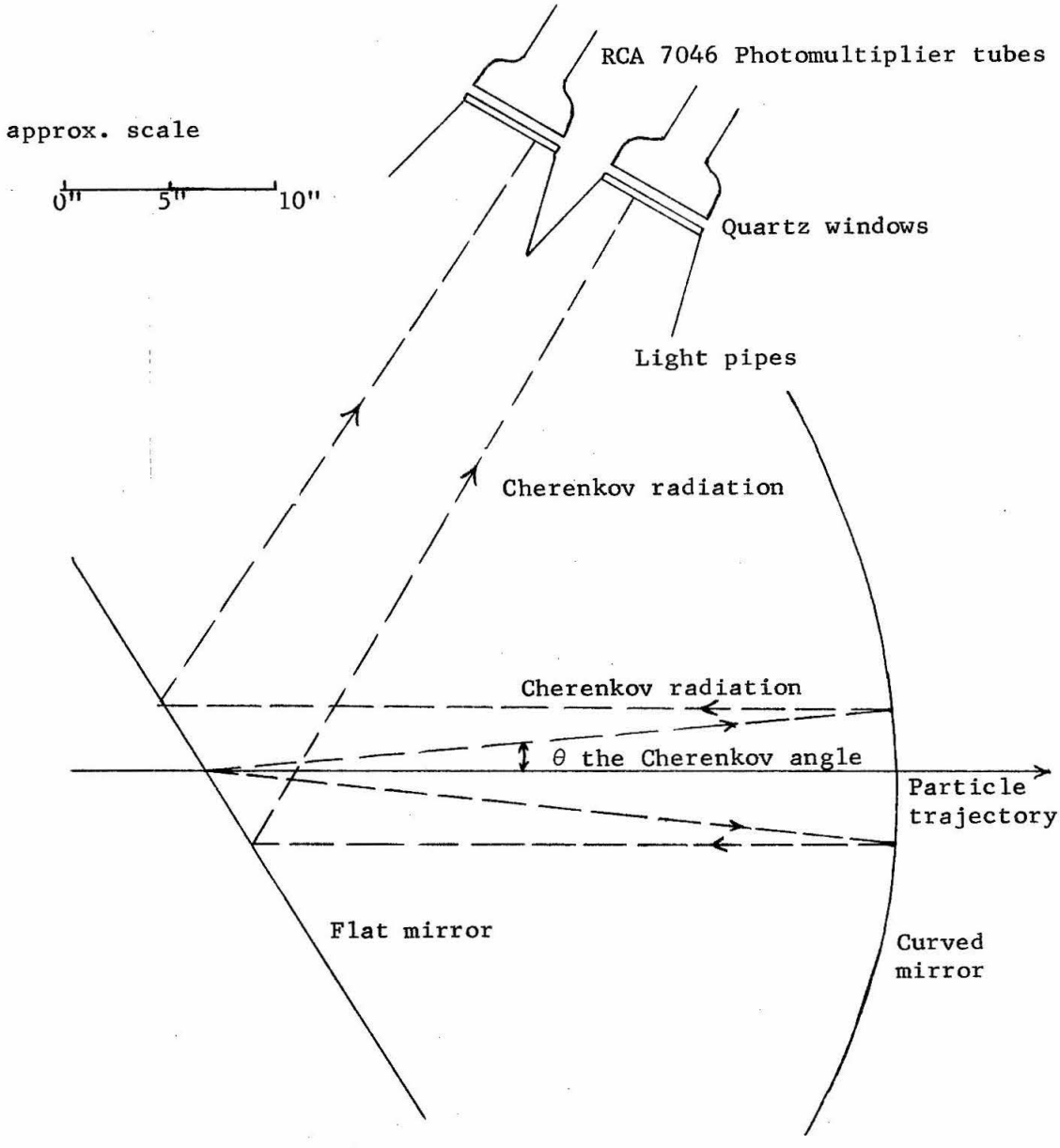

Figure 2.11: Cherenkov pulse height channel distributions for:

(a) Particles with momentum about 1.61 GeV/c

(b) Particles in distribution (a) which are tagged as pions by the time-of-flight system.

(c) Particles with momentum about 0.92 GeV/c (below threshold for Cherenkov radiation even for pions).

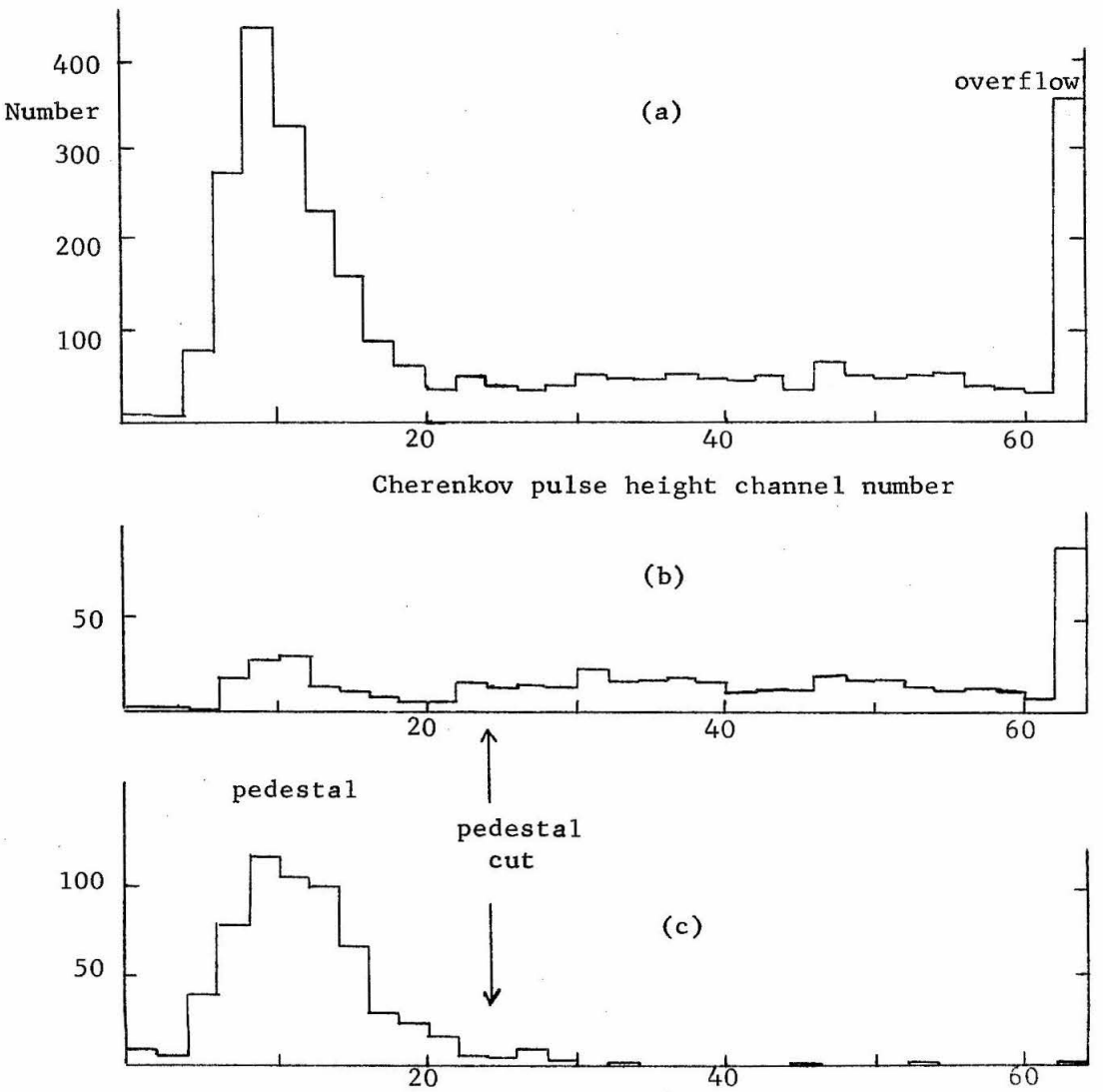

From 2.11b we see that we usually remove 75-85% of all the pi's by throwing away all events with Cherenkov pulse height channel above the arrow. Figure 2.11c shows a distribution of particles with momentum below threshold. We see that less than 2% of such particles have a Cherenkov pulse height above the arrow. Thus, we expect to lose less than 2% of protons by making this cut.

As mentioned above, the counter cannot separate about 20% of the pions from the protons. This is not due to the design of the counter. Although the counter was not built expressly for the experiment[2.9] and the geometry is not ideal, the mirrors are adjustable and we can still focus the light without significant loss in our geometry. We could have better performance by using photomultiplier tubes with higher quantum efficiency[2.32]. This was rejected due to cost. We used some available photomultiplier tubes which gave adequate performance[2.31].

Actually, the major source of inefficiency for pion counting comes from the possible scattering of pion with the front wall of the counter. Any scattering with large transverse momentum transfer would result in final state particles with bad geometry. Even if the particles Cherenkov radiate, the light may not be focused onto the photomultipliers. We found this by looking at the pulse height of those pions which pass through the counter unscattered (we put a scintillation counter behind the counter in coincidence while using a collimated beam of pions). The efficiency for those particles is better than 95%. The thick walls of the counter cannot be reduced since we require 120 psi inside the counter.

For low momenta, we could have used a liquid Cherenkov counter[2.33] which could count pions down to 0.3 GeV/c or 0.4 GeV/c and still have proton threshold above 1.0 GeV/c. However, for these particles, the time-of-flight system discussed in the next section does a good enough job.

(c-v) The Forward Outgoing Particle Time-of-Flight System (TOF)

We shall abbreviate the system by TOF in the following section. The time delay between the arrival of the signal from the T counters and the signal from S_3 counter (for the relative positions, see Figure 2.2, page 12) provides us with a way to measure the velocity of the forward outgoing particle. For particles of the same momentum, the pions will have a shorter delay time than protons.

The TOF system works as follows. The signal from S_3, shaped by a discriminator, arrives at the pulse height analyzer and starts a 2.5 gigacycle clock scaler. The signal from the T counters stops the scaler and the elapsed time for the clock scaler is read and recorded using 6 binary bits. There are 64 channels and each successive channel is separated by about 0.4 nsec. The FWHM of the system is about 2 nsec.

We show in Figure 2.12a a typical TOF channel distribution for particles close to a particular momentum. We see clearly resolved pion and proton peaks. Thus, the TOF system can be used to remove the pion background at low momentum where the gas Cherenkov counter cannot count pions.

Above 1.2 GeV/c, the pion and proton peaks are not well

Figure 2.12: Time-of-flight channel distribution for low (0.99 GeV/c) and high (1.61 GeV/c) momentum particles.

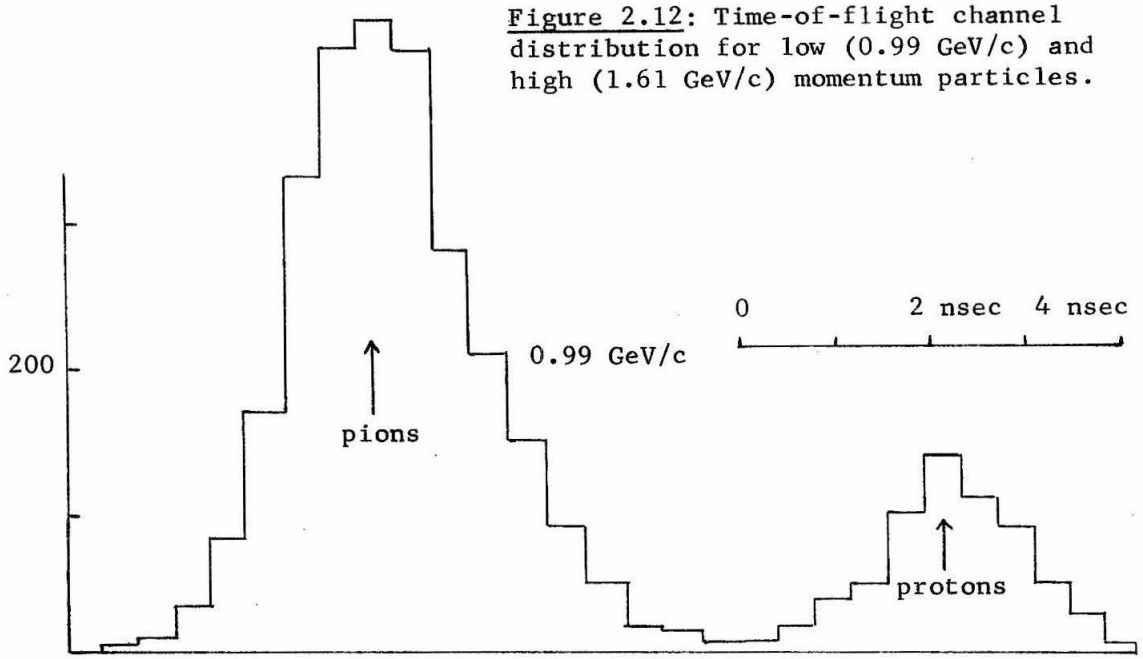

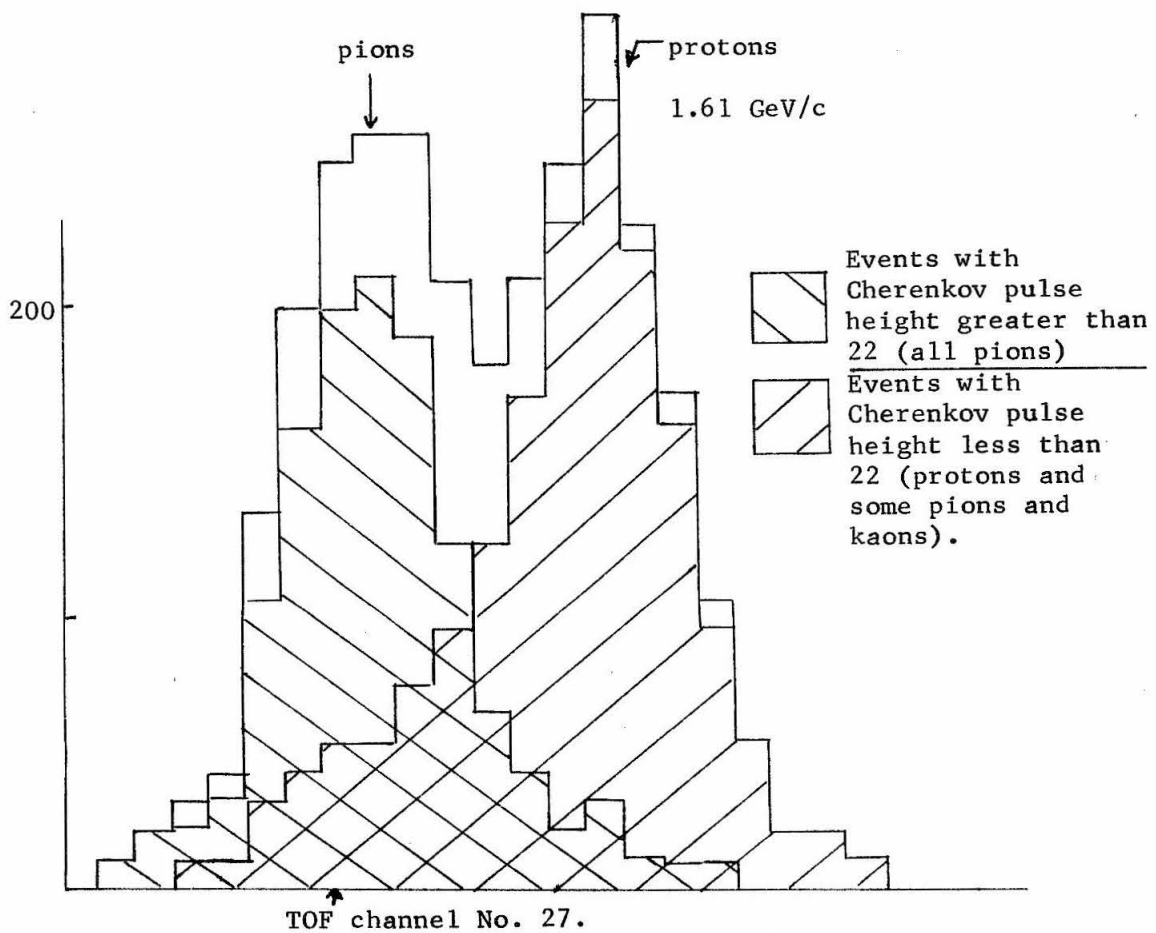

separated. Figure 2.12b shows a typical higher momentum TOF distribution. We also show in different shadings the event distribution for those events with gas Cherenkov pulse height above 24 (almost definitely pions) and below 24 (contains both pions and protons). We can reject all events with TOF channels less than 27 without losing many protons.

d. Recording and Monitoring of Data

(d-i) Introduction

The analysis of our data is done off-line[2.34]. For each event satisfying our triggering criteria, the various information about the event is recorded on magnetic tape by a system consisting of a PDP-8 computer with tape drive and interfacing[2.35].

The information from the wire spark chambers (described in detail in Appendix B) specifying the spark positions are digitized by a system of clock scalers. This procedure is discussed in Section (d-ii). In Section (d-iii) we describe the PDP-8 and the interface system of recording the data. Section (d-iv) contains a summary of the data recording procedure including triggering, wire spark chamber pulsing and counter bits. Section (d-v) contains a list of the information recorded for each event. We describe in Section (d-vi) the procedures we used to monitor the data taking.

(d-ii) Wire Spark Chambers and the Recording of Digitized Spark Positions

To record the positions of the particle trajectories for each

triggered event, we use 12 wsc (wire spark chambers). These wsc are divided into three sets of four wsc and measure the incident $\bar{p}$, the recoil proton, and the momentum analyzed recoil proton trajectories. The positions and sensitive area sizes of the 12 wsc are given in Table 2.4. We describe the construction, operation and characteristics of the wsc in Appendix B. We shall briefly describe the operation in the following paragraph.

A trigger logic signal (specifying that the trigger condition has been met) is sent to the wsc pulsing system. The pulsing system then applies the charge from a storage capacitor across the wire chamber planes through a thyratron circuit. Spark avalanches occur at the points where ionization from passing charged particles exists. Fiducial lines which are placed at both sides of the sensitive area are simultaneously pulsed. The magnetostrictive readout wire then transmits the magnetostrictive wave pulses into readout amplifiers. The resultant signal is transmitted into a digitizer.

The signal from the readout system of the wsc is a string of pulses specifying the spark positions for each coordinate in series. The pulse signal from each coordinate in a wsc is transmitted back into magnetostrictive pulses of successive coordinate so that the final signal of the 24 coordinates of the 12 wsc are in series. Part of a typical signal train containing two coordinates is shown as "input" in Figure 2.13. We digitize the signal in order to store the information in magnetic data tapes.

The fiducial line at the edge of the sensitive area is pulsed at the same time as the sparking of the wsc. The position of the

Table 2.4: Sizes and Positions of the Sensitive Areas of the wsc

wsc	Sensitive area	z position	x position	y position
(regions 1 and 2)				
1	36" (x) by 18" (y)	- 18-3/4"*	-33" to 3"*	-9" to 9"
2	same	- 15-3/4"*	same	same
3	same	- 12"*	same	same
4	same	- 9-1/4"*	same	same
(regions 3 and 4)				
5	18" (x) by 9" (y)	12-3/4"	- 2" to 16"	-4-1/2" to 4-1/2"
6	same	19-1/4"	same	same
7	same	25-1/2"	same	same
8	same	31-3/4"	same	same
(regions 5 and 6)				
9	36" (x) by 18" (y)	144-1/2"	-19-1/4" to 16-3/4"	-9" to 9"
10	same	153-1/2"	-21-3/4" to 14-1/4"	same
11	same	162-1/2"	-23-3/4" to 12-1/4"	same
12	same	171-1/4"	-26-1/4" to 9-3/4"	same

* For the first four wsc, the z distance is the distance normal to the chamber from the center of the target. Since the wsc is set at 45^{o} to the beam line, the distance from the target center to the beam line intersect of each wsc is thus a factor of $(2)^{1/2}$ larger. The x position is measured with respect to a coordinate system set at 45^{o} to the beam line. x = 0 is the beam line.

Figure 2.13: The wire spark chamber signals and the digitizer operation.

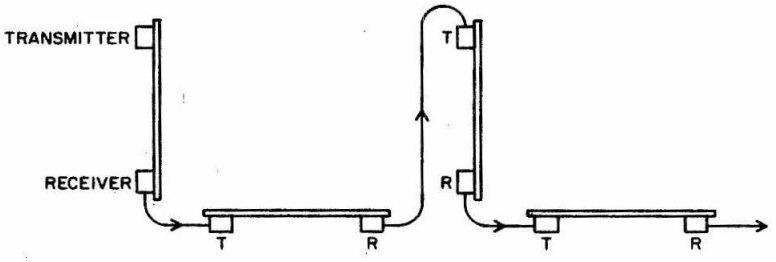

SERIAL CONNECTION OF MAGNETOSTRICTIVE PICKUP LINES

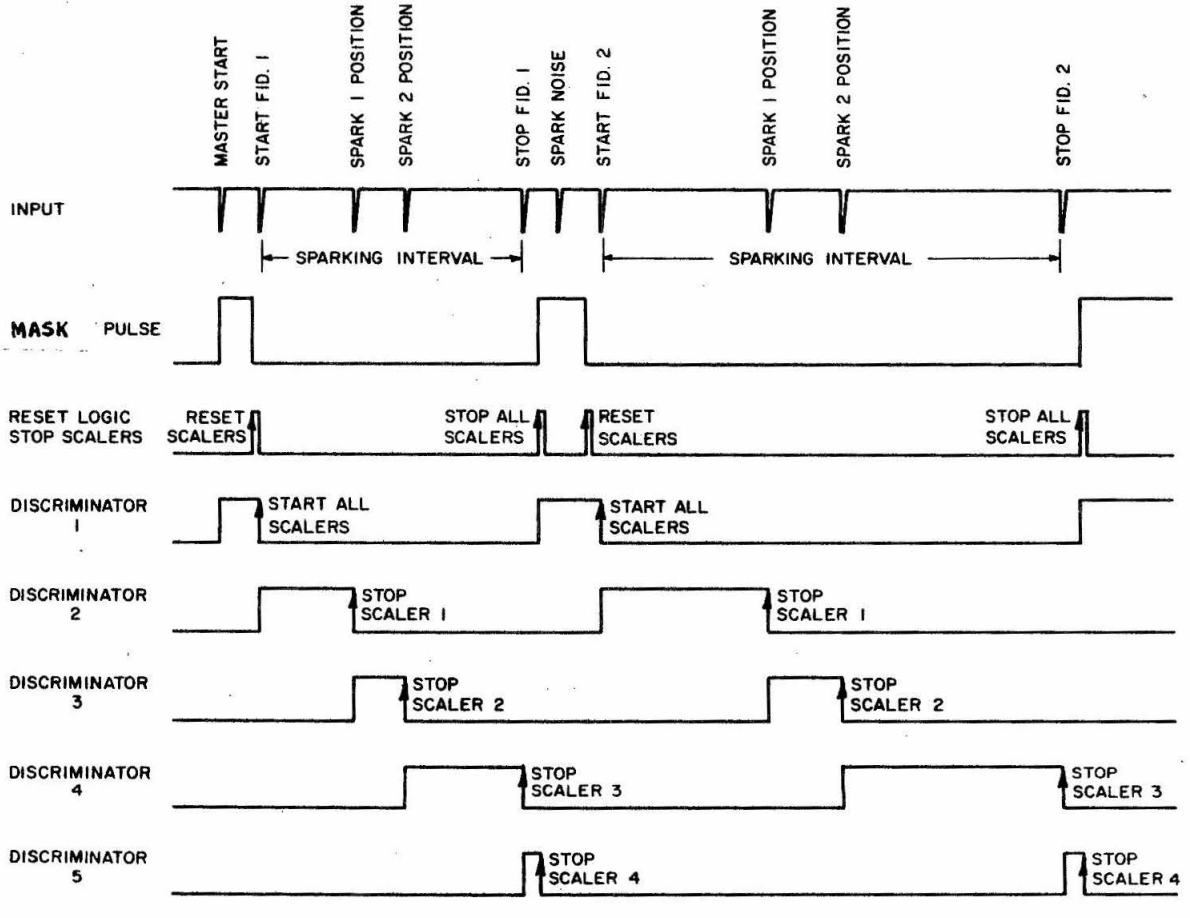

SCALER SWITCHING LOGIC

fiducial was surveyed and measured to a great accuracy[2.36]. Thus, we can use the fiducial pulse as a reference. The time delay between the spark pulse and the fiducial pulse thus represents the distance between the position of the fiducial line and the spark position. Figure 2.13 shows a schematic drawing of the operation of the digitizer[2.37]. The fiducial near the receiver gives a pulse which arrives first -- called the first fiducial or starting fiducial. This signal starts four 10 megacycles clock scalers. Each subsequent pulse received then stops one successive scaler. At the end of each coordinate segment, all scalers still running are stopped by the interface. The scaler readings are then transferred into the buffer and eventually written onto magnetic data tapes (see d-iv).

The interface issues a mask pulse prior to each coordinate designed to screen out the noise due to chamber sparking. This mask pulse, adjustable in timing, is issued about 5 microseconds after the second or stopping fiducial of the previous coordinate and is terminated about 3 microseconds prior to the first fiducial. Note that the noise pulses are the transmitted pulses which were picked up by the amplifiers of each coordinate and thus arrive before the first fiducial of each coordinate.

The leading edge of the mask pulse stops all the scalers. The four scalers are read and reset during the existence of the mask pulse. The first pulse after the mask pulse is terminated is assumed by the interface to be the first fiducial of the next coordinate and any subsequent pulses are assumed to be spark pulses or the second fiducial. If any noise pulses arrive before the first fiducial and

after the mask pulse is terminated, difficulties occur. Such occurrences were kept at a tolerable level (less than 1/2%) by continuously monitoring the output of the digitizer and the timing of the mask pulse.

For each coordinate, since only four scalers are used, a maximum of 4 spark positions can be recorded. Any spark position beyond the fourth one is lost. Since the scalers are 10 megacycle scalers, the time delay between the first fiducial and the spark signal is digitized in 100 nsec steps. Since the velocity of the magnetostrictive wave is 5.2×10^5 cm/sec, this corresponds to steps of 0.52 mm.

We will make a few comments on the serial readout system. Compared with the parallel readout system where each coordinate has its own digitizing system, the serial readout system requires fewer scalers and electronics. It is also simpler to operate and monitor. Since our dead time of 20 msec is imposed by the recovery time of the wsc, the additional time required to serially digitize the 24 coordinates (about 3 msec) does not make us lose any beam. There are two disadvantages in the serial readout system. Since all 24 coordinates are interconnected, trouble shooting is more difficult. In many instances, the trouble spot cannot be localized immediately. In addition, any reduction in resolution due to the readout system, such as one particular pick-up coil being too wide, could cause similar resolution loss in all subsequent coordinates whose signals, because of the serial readout configuration, have to pass through the amplifier of this coordinate.

(d-iii) PDP-8 Computer and Interface System of Recording the Data

The interface system allows the PDP-8 to communicate with the various electronic systems such as the digitizer, counter bits, scalers, trigger electronics, etc. It coordinates the reception of the data.

The procedure which the interface system is involved in is as follows (we will summarize all the data taking procedure in the next section).

1. The interface receives the trigger logic signal specifying that the trigger condition has been satisfied. It is understood that another signal has been sent to pulse the wsc.
2. The interface than sends a signal (called the "BUSY") to the master gate for a duration of 20 msec. During this period, the trigger logic modules are gated off (see Figure 2.9).
3. The interface handles the counter bit information as described in Section (c-iii). The information is stored in the buffer and eventually written onto magnetic tape.
4. The interface activates the digitizer system to handle the arriving spark signals. For each coordinate, a mask pulse is issued at the appropriate time and the scalers are read. The four scaler readings are combined into one 60-bit word (12 bits are sufficient for each number since the scaler count never exceeds 1900. The remaining 12 bits are blank.) All the spark information, which is stored in the buffer, takes 24 words for each event.

During each beam pulse, the interface can put a maximum of 15 event records containing 30 60-bit words each[2.38] (24 spark infor-

mation words, counter bit information word and 5 blank words) in the buffer. The size of the buffer imposes this limit. If 15 events were accepted, any additional events (and $\bar{p}$) for that beam pulse are rejected. At the end of each beam pulse, the information in the buffer is transferred into the magnetic data tapes. In addition, the PDP-8 also make special calculations on items which we wish to monitor (see Section d-vi).

The user is allowed to interrupt data taking to print out the information stored in the buffer. This allows us to check the format and contents of the event records and aids us in trouble-shooting and monitoring.

(d-iv) Data Recording - Summary of Data Taking Procedure

We are now prepared to describe the over-all data taking procedure.

Data are separated into data files called "runs" which usually last 1-2 hours. These runs are separately identified. Thus, runs with significant inefficiencies can be discarded without affecting the rest of the data. For each run, the PDP-8 writes run records (whose contents is described in the next section) before and after all the event records.

During a data run and before the beam pulse arrives, the entire data system is dormant -- the trigger logic is gated off. The gate is removed upon the reception of a signal from the AGS signifying the beginning of the beam of $\bar{p}$'s. The trigger logic then tests each incoming $\bar{p}$ to see if the trigger condition is satisfied (see c-ii). We will now describe what occurs when an event satisfying the trigger

condition is detected (Figure 2.14 is a timing diagram of what occurs -- all timings are approximate).

1. At T = 0 to 20 nsec, the event occurred. It takes 20 nsec to go through the apparatus. The scintillation material in the counters receives light.

2. It takes of the order of 50 nsec to get through the photomultiplier and an additional 20 nsec cable delay before the trigger logic receives the various counter signals.

3. The trigger logic, after about 50 nsec electronics delay, decides that the event satisfies the trigger condition. It sends four signals:

A) One to pulse the wsc; B) to the interface; C) to the delay module which eventually turns off the interface again after 20 msec, and D) to the prompt event gate to turn the master gate on before the interface sends the BUSY signal. Note that the trigger logic is now incapacitated by the master gate. We shall now follow each of the signals.

A1) The pulse driver (Appendix B) receives the trigger logic signal after about 10 nsec cable delay. T is now about 170 nsec.

A2) After a delay of 20 nsec, the pulse driver sends an 800 volts, 80 nsec-wide pulsing signal to all the 12 pulsers.

A3) After a delay of approximately 20 nsec (for transit time in the cables), the pulsers receive the pulse driver signal.

A4) The pulser fires the thyratron about 60 nsec after it receives the pulse driver signal.

A5) The thyratron is turned off by the inductive kickback produced

Figure 2.14: Trigger and event recording timing diagram (continue on the next page). All timings are approximate.

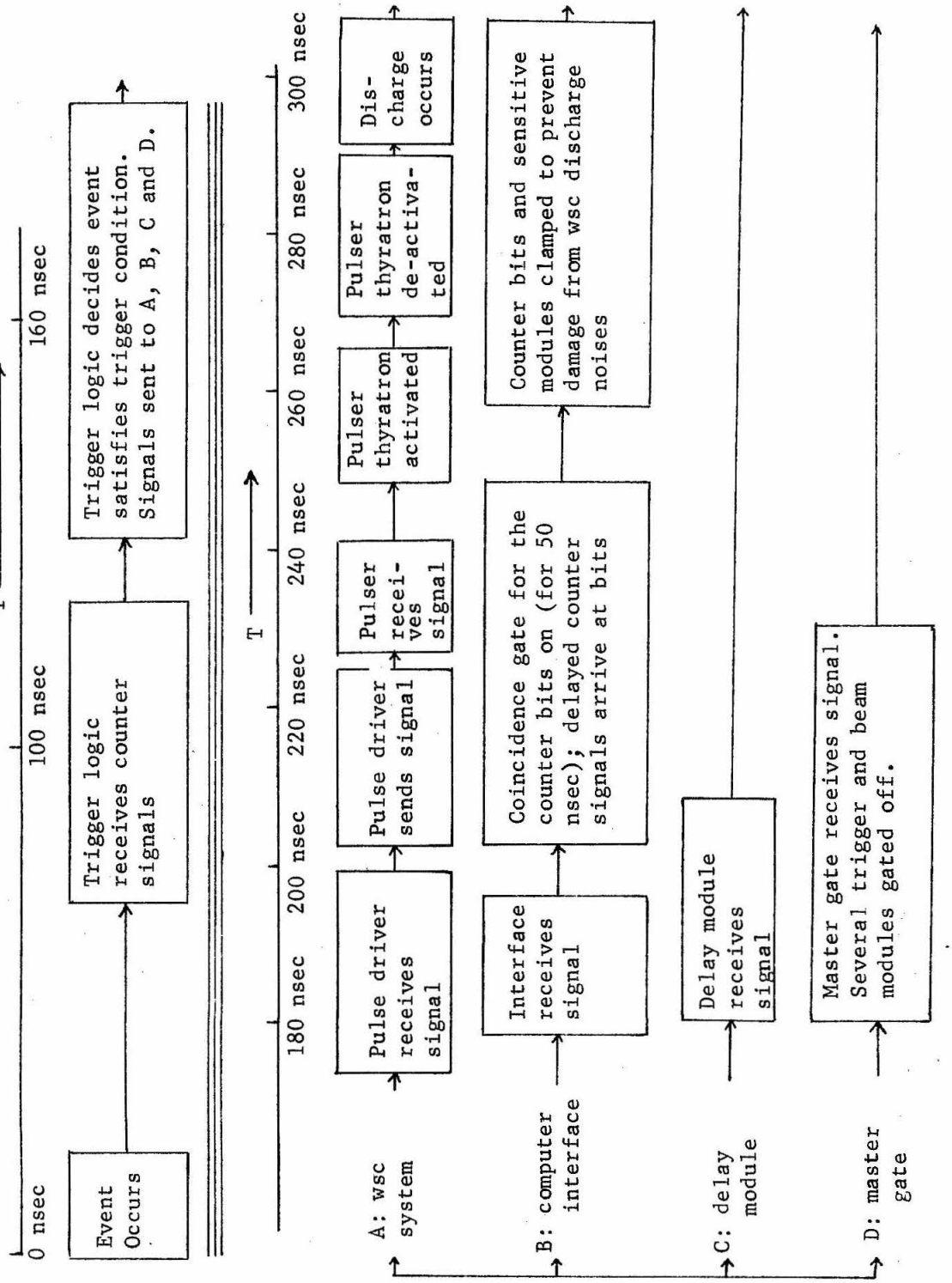

Figure 2.14: (continued) Trigger and event recording timing diagram.

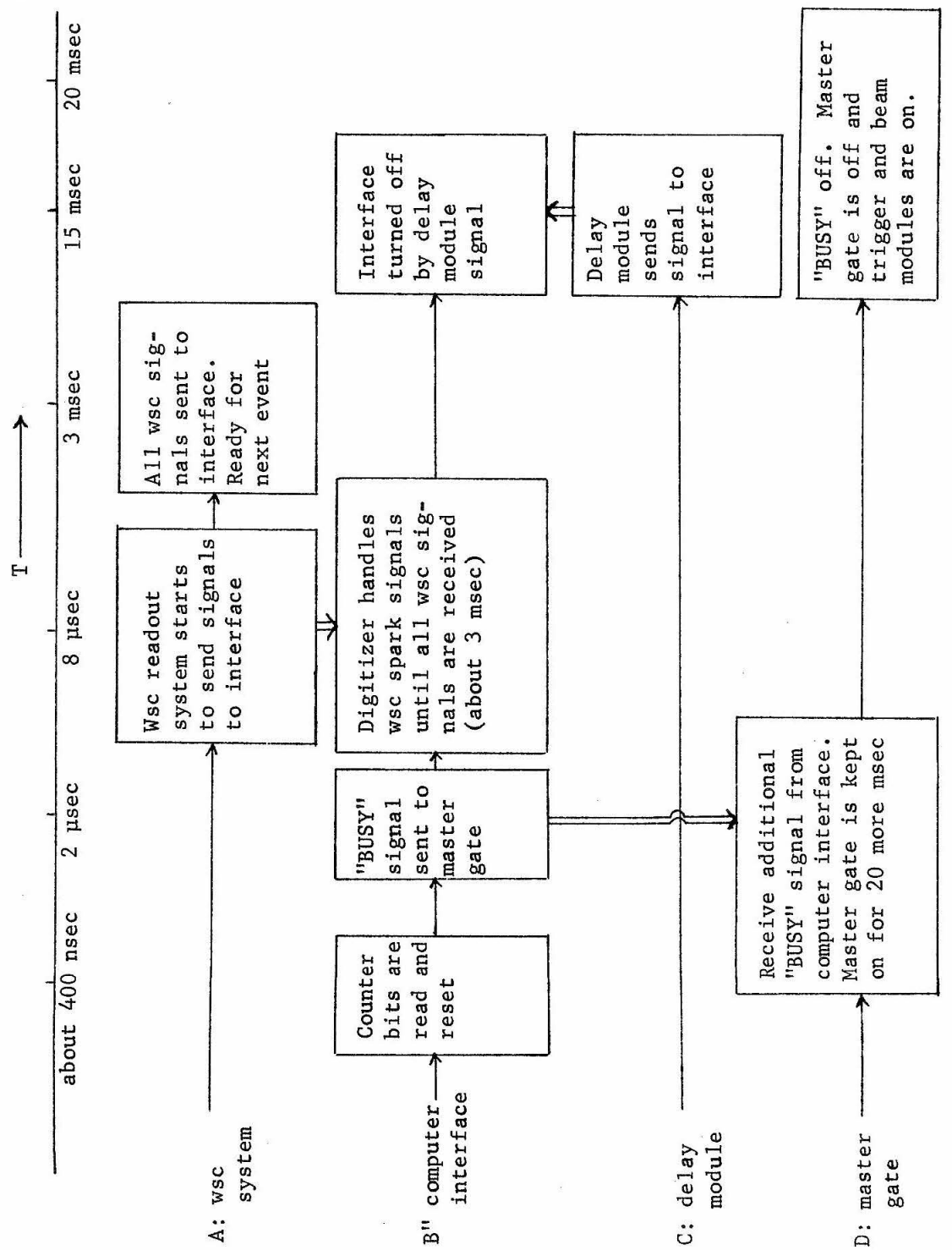

by the trailing edge of the pulse driver signal, which arrives about 20 nsec after the thyratron is fired.

A6) The spark discharge takes about 30 nsec to form; thus, it occurs about 30 nsec after the thyratron is fired; T is now about 300 nsec.

A7) After a delay of about 8 nsec due to transit delay in the magnetostrictive readout wire and in the readout amplifiers, the signal train of the spark information begins to arrive at the digitizer, which has been anticipating the signal (see B-5 below); the signals keep arriving and is processed for a duration of about 3 msec. All the spark information has been sent and the readout system is ready for the next event (note, the readout amplifier system is not turned off). However, as mentioned in (d-vii), the wsc requires recovery time of the order of 20 msec.

B) The interface system;

B1) The interface receives the trigger logic signal after a cable delay of about 20 nsec.

B2) Coincidence gate for the counter bits (for a duration of 50 nsec) is sent; the appropriate counter signals, delayed for an appropriate time (typically 100 nsec), arrive during the period of the gate and thus are allowed to set the bits.

B3) After the previous step, at T approximately 250 nsec, the counter bits modules as well as other sensitive modules are clamped to prevent the wsc sparking noise from creating disturbances. The clamping lasts until after the wsc spark discharges

(at T approximately 300 nsec).

B4) Afterwards, the counter bits are read into the memory buffer and reset.

B5) At T about 2 μsec, the BUSY is issued (this signal lasts for a duration of 20 msec) to the master gate. For the duration of this signal, the master gate gates the trigger logic off (see D2 below).

B6) In the meantime, the interface prepared the digitizer to receive the wsc spark signals. These signals, in the form of a train of pulses, arrive for a duration of 3 msec starting at T about 8 usec. The interface transfers the scaler readings of each coordinate to the buffer after the digitizer treated that coordinate (see d-ii).

B7) The interface received the delayed signal C (see C2) which turns the interface off except for the BUSY; the interface now awaits the next trigger logic signal.

B8) At t = 20 msec, the BUSY is stopped. The master gate is now off and the trigger logic is reactivated. New events can now be accepted and we go back to step 1.

C) Delay module

C1) At T about 180 nsec, the delay module receives the trigger logic signal.

C2) After a delay of 15 msec, it sends a signal to the interface to turn the interface off except for the "BUSY" signal, which remains on for an additional 5 msec.

D) Master gate (when this gate is on, the trigger logic is turned off; (see Figure 2.9).

D1) The master gate receives the fourth signal from the trigger logic -- the "prompt event gate"; this turns the master gate on for 30 μsec; however, prior to the end of this period of time, the master gate receives

D2) The "BUSY" signal from the interface; the BUSY is continuously sent for 20 msec during which the master gate is kept on and the trigger logic kept off.

Thus, at the end of 20 msec, we are ready to start again at step 1.

This process continues until either 15 events are accepted or the signal from the AGS specifying the end of the beam pulse is received. The data taking system except for the PDP-8 is now dormant. During the 2 seconds between each successive beam pulse, the PDP-8 writes the event record information onto magnetic tapes and does calculations for monitoring the data taking. The monitoring of data taking is described in Section (d-vi). The data taking system now awaits the next signal from the AGS indicating the next beam pulse.

Our buffer is only large enough for 15 event records. It is possible to increase the buffer size so that more event records can be accepted per pulse. However, since the beam duration per pulse is only 400 msec while the dead time per event is 20 msec, accepting 15 events per pulse already implies that we are only using 1/4 of the beam. Thus, accepting more events per beam pulse would only be important if our trigger rate or beam intensity is high. This is true

only for the highest momenta. Thus, any gain we make would not be significant over-all.

(d-v) The Contents of the Data Recorded

Data recorded on the magnetic tapes

For each triggered event, we record on data tapes:

1) 24 60-bit words[2.38] (each word stored as 10 6-bit characters on tape) each consisting of 5 12-bit numbers. The first four are the scaler readings of the digitizer for the signals from a coordinate representing spark positions. The last number is blank to provide a check on the format of the record. If the last number is not blank, then we know something is wrong.

2) A 60-bit word containing 48 bits of counter information (see c-iii).

3) 5 blank 60-bit words. This also allows us to check the format of the record.

For each run we record at the beginning and at the end a record of 30 60-bit words containing the information of the condition under which the data is taken, some identification numbers and the scaler readings specifying fluxes and number of triggered events. The run condition information which we record includes nominal momentum, NMR frequency of the bending magnet, beam charge and type, and magnet polarity. Each run is identified by an individual run number. The scalers which we read include those which scale $\bar{p}$ flux, number of triggers and number of beam pulses.

Data recorded manually

Important normalization numbers such as $\bar{p}$ flux are also recorded manually to double check. In addition, the condition of the

apparatus such as the counter voltages, spark chamber conditions, etc., are also recorded in case of any question on the data.

(d-vi) Monitoring of the Data Taking

During the data taking, we must make sure that the apparatus is functioning properly and that the various important ratios such as trigger per $\bar{p}$ are constant. We use the PDP-8 as well as several manual monitoring procedures to do this.

PDP-8 monitoring of data taking

The PDP-8 prints out at the end of each data run several items which it calculates or increments based on the events recorded. Among the items which it calculates is a number reflecting the wsc efficiency for each coordinate. This number is calculated by comparing the number of sparks in each coordinate with the number of sparks of the other coordinates in the same set of 4 wsc. Any abnormal drop in any of the 24 efficiency numbers indicates immediately that the wsc system is not functioning properly.

The total number of events with each binary bit is also printed out. Thus, any fluctuation in the percentage of any of the numbers also indicates a possible inefficiency.

The PDP-8 also keeps track of the format of the event records; the number of events with format errors is printed out for each run.

Manual monitoring of the data taking

We calculate the beam and trigger ratios for each run and make sure they do not fluctuate wildly. Condition of the apparatus, such as the voltages, are recorded continuously and checked. Efficiency checks are also performed on the R counters using sandwich counters

for coincidence. Any data runs which contain data taken while the apparatus was not functioning properly are discarded.

e. Evaluation of the Apparatus and Data Taking System

We will evaluate our experimental system through three criteria:

A) Rate of backward elastic events.

B) Appropriateness and efficiency of our equipment, and finally

C) Data systems.

A) Rate of Backward Elastic Events

We will first discuss the beam. The beam is described in Appendix A and in Section (b-i). The beam rates are summarized in Table 2.2. The number of $\bar{p}$'s is sufficient (for our experimental system) at high incident momentum. At the lower momenta, the number becomes much smaller. At high momenta, the pi/$\bar{p}$ ratio is quite acceptable (about 1) but deteriorates at lower momenta. Since the beam was designed to be used above 1.0 GeV/c, the fact that we have appreciable numbers of $\bar{p}$ below 1.0 GeV/c is already quite satisfying.

Our geometry has a laboratory acceptance of about 22 msr. The smallest aperture is the sensitive area of the 12th wsc, which is 3' by 1-1/2' and is about 14' from the target. Since we require a momentum spectrometer and therefore a magnet, it is difficult to shorten the distance to the target. In our case, the magnet and its shielding takes up 8'. Therefore, unless we are willing and can afford to use larger track recording devices, the geometry cannot be improved.

Another major factor is the dead time. Typically, we lost about 50% of the beam due to dead time. One way to reduce the loss is to

tighten the trigger. We have discussed this in the section on triggering (c-ii) and concluded that only slight improvement can be made. Dead time can be shortened. For example, if we use proportional wire chambers[2.39], most of the dead time can be eliminated. However, there are problems such as cost. Also the development of these chambers has only occurred since we took our data.

B) Appropriateness and Efficiency of our Equipment

As we have mentioned before, we need to identify the incident $\bar{p}$, identify the forward outgoing recoil proton by its velocity and to recognize the backward elastic event by its kinematics and topology. We must also have a trigger system to selectively trigger our wsc.

B1) Incident $\bar{p}$ identification. Our $\bar{p}$ identification system is very efficient in rejecting pions and counting $\bar{p}$'s (see b-i). Typical contamination of pions is about 0.5% and $\bar{p}$ counting efficiency is about 90% at high momenta. Thus, improvements are not necessary.

B2) Recoil proton identification by velocity. This identification is not absolutely necessary. We can do a background subtraction if there are large numbers of pions in the signal since no process will give an enhancement of pions with momentum close to the incident momentum[2.40]. However, we need to remove the pions if we were to get a good idea of the angular dependence of the dcs (differential cross section). Background subtraction for each angular bin would give reduced accuracy.

We use two methods to obtain the velocity of any forward outgoing particle -- Cherenkov radiation and time-of-flight. The gas Cherenkov

counter has a threshold of 1.1 GeV/c for pions. This is constrained by the fact that the index of refraction of the radiator is only 1.009, we can get more Cherenkov radiation and lower pion threshold if the index of refraction is higher. However, this is difficult to obtain, since under atmospheric pressures, no gas has refractive index above 1.002 while no liquid or solid has refractive index below 1.20. We have decided not to use higher pressures since doubling the pressure only lowers the threshold by 30%.

The time-of-flight system we used has a resolution of 2 nsec FWHM. It is difficult to obtain better resolution since the counters themselves are 1' long. Although we have used the position of the particle trajectory as it passes through the counter to correct for this, the improvement in resolution is not significant.

Other methods for determining the velocity of a particle includes measuring the energy of the particle[2.41]. However, this cannot be easily done to an accuracy useful for us.

B3) Kinematics -- momentum spectrometer. To determine the kinematics of the event, we use a momentum spectrometer consisting of a bending magnet with two sets of wsc to measure the deflected and undeflected trajectories. We need a good momentum measurement to discriminate against the inelastic background. Using a magnet system rather than other systems (such as range counters to measure energy) is a reasonable choice due to the superior resolution[2.41]. We have chosen wire spark chambers (wsc) to measure the position of trajectories because of the large area possible, low cost, high rates, simplicity in operation and the ability to obtain digitized results.

The major disadvantage is the inability of placing the wsc inside the magnet. This results in a great reduction of solid angles since the farthest wsc must be placed about 14' away. However, if we wish to use track recording devices which can be placed inside the magnet, we will probably run into the problem of added cost and complications in logistics (the space inside the magnet would be cramped and trouble-shooting would be difficult).

B4) Trigger system. The trigger requirements are dealt with adequately by the $\bar{p}$ counting system and the various trigger counters. We have discussed (in c-ii) ways to tighten the trigger and concluded that the system we used is quite adequate.

B5) Equipment operation. The various counters and wsc we used are quite efficient. Typical scintillation counter efficiency is about 99.5%. Typical wsc efficiency is about 99%.

Equipment breakdown occurs occasionally and the amount of beam time lost due to this factor is about 10%.

C) Data System

Our data are not analyzed on-line. The on-line computer system only records the data and monitors the data taking. The capabilities of our on-line system is limited by the memory size (4K 12-bit locations) and the fact that we may have up to 15 events per 2.4 seconds. The computer is only free during the beam off time (about 1.8 sec.). Even if memory is no problem, the PDP-8 will only be fast enough to analyze on the order of 5 events per pulse.

Thus, if we wish to have an on-line analysis system , we need a much larger computer (memory size at least 20K). At BNL, it is

possible to tie our experiment on-line with the PDP-6 computer which exists at the AGS. Since we would not be the only user, problems due to multiple usage may occur. The physical location of the PDP-6, which is not very close to our equipment, could also cause some problems.

Actually, the preliminary analysis for our experiment is done within a very short time from the data taking time (usually 5 to 10 hours) by using the CDC-6600 computer next to the AGS. Therefore, we do have almost instant feedback, which is the major advantage of the on-line analysis system.

CHAPTER III: ANALYSIS OF THE DATA

a. Introduction

The magnetic data tapes contain records of the spark positions and counter bit information for each triggered event. We must use this information to determine how many backward elastic events are among them. The analysis of the magnetic data tape information is done off-line at the Brookhaven CDC-6600 computer center in two stages[3.1]. In the first stage, as described in Section (b), we reconstruct the event trajectories from the digitized spark position information. Given the event trajectories, we can calculate various quantities such as momentum of the recoil proton, angle of scattering, position of interaction vertex and the topological quantities which measure the amount of additional scattering(s)[3.2]. These quantities, along with the forward particle velocity information from the gas Cherenkov counter and the forward particle time-of-flight system, are used in the second stage of the analysis, which is described in Section (c). This stage consists of making various selective cuts which remove background. In the case of momentum background (i.e., events satisfying all other cuts but have slightly wrong momentum), we make a background subtraction. We thus arrive at the number of backward elastic $\bar{p}p$ events. These events are separated into several angular bins.

To obtain the correct normalization, we study all sources of normalization errors in Section (d). The normalization corrections due to reconstruction inefficiency and selective cut losses are

handled by Sections (b) and (c), respectively. We use a Monte Carlo program[3.3] to calculate the angular acceptance of our apparatus. This is described in Section (e).

Having obtained a corrected number of backward elastic events and the angular acceptance of our apparatus for a particular angular bin, we can calculate the differential cross section (dcs) for this angular bin. This is covered in Section (f). We obtain the error of the dcs by combining the statistical error, Monte Carlo error and other errors associated with corrections, uncertainty, etc., in Section (f).

A summary and assessment of the analysis procedure is presented in Section (g).

b. Reconstruction of Events

(b-i) Introduction

In the first stage of the analysis, we reconstruct the event trajectories from the magnetic data tape information. The trackfinding, which is detailed in Section (b-ii), involves finding at least three sparks whose position lies on or near a straight line. The horizontal and vertical coordinates of each set of wsc are treated separately. The trackfinding is two dimensional.

The desired topology of a background elastic event, as shown in Figure 3.1a, requires the existence of (1) an incident $\bar{p}$ beam track, (2) a recoil proton track in the second set of wsc (downstream of the target), and (3) a recoil proton track in the third set of wsc downstream of the magnet (the track would have been horizontally deflected by the magnet). 35% of the reconstructed events fail to have a

track in some region (either the horizontal or vertical view of any of the 3 sets of wsc). They must be discarded since the topology, momentum or scattering angle would be unspecified without a track in each region. We study such events in Section (b-iv) and Section (b-v) and show that aside from an insignificant number, no backward elastic events are lost by rejecting such events.

30% of all events have more than 1 track in some region. We must throw away all but one of the tracks since the desired topology allows only one track per region (see Figure 3.1a). We throw away any spurious track by using various topological properties of a backward elastic event and also some counter information. This process is described in Section (b-iii).

The reconstruction process is expected to be inefficient for some number of events. We study the inefficiency in Section (b-iv) and conclude that about 5% of the backward elastic events fail to be reconstructed correctly and are lost.

As mentioned above, we discard all reconstructed events which lack a track in any region. We account for these events by studying any possible sources which may give rise to these events. The conclusion of this study, which is described in Section (b-v) is that the number of reconstruction events discarded is close to expectation.

(b-ii) The Finding of Event Tracks from the Digitized Spark Positions

For each region consisting of four horizontal or vertical coordinates, we have the numbers specifying the spark positions (a maximum of four spark positions are accepted by the readout system of each coordinate). Through the knowledge of the spatial position of

Figure 3.1: (a) Horizontal and vertical views of the topology of a desired backward elastic event showing particle trajectory (dot-dash line), wsc planes (solid lines), bending magnet. x's are the expected sparks for this event.

(b) Extrapolated x and y positions of tracks at planes $z = z_v$ (where VD is minimized) and z = magnet center. $(x,y)_{AB}$ is defined as the extrapolated (x,y) using tracks from regions A and B. Reconstructed vertex is defined as z_v.

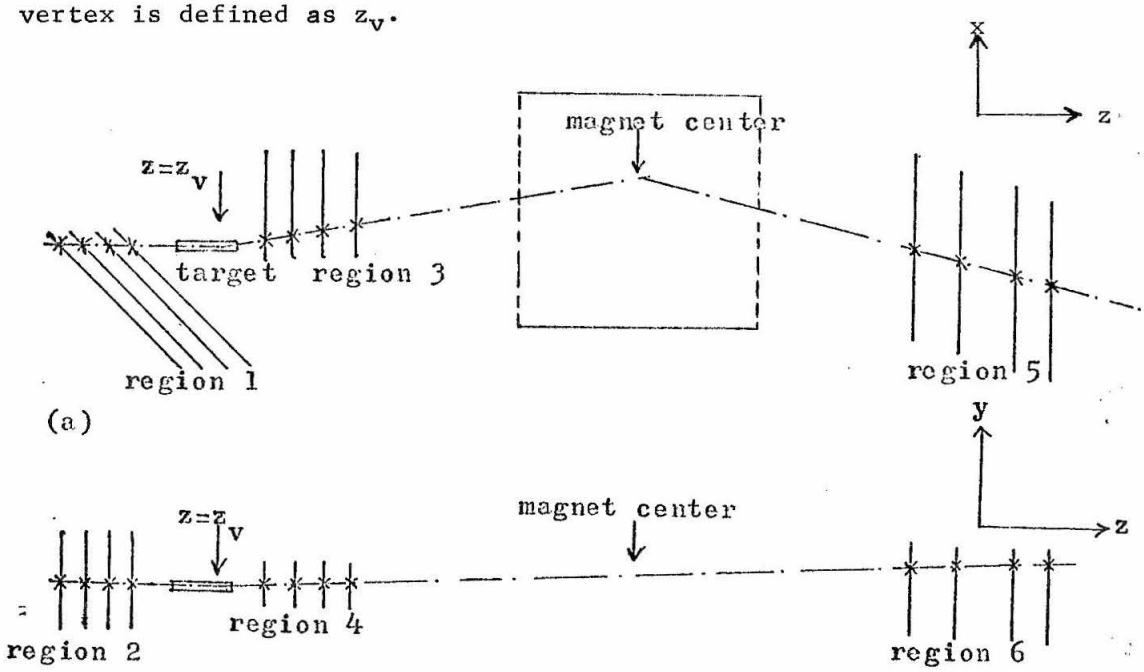

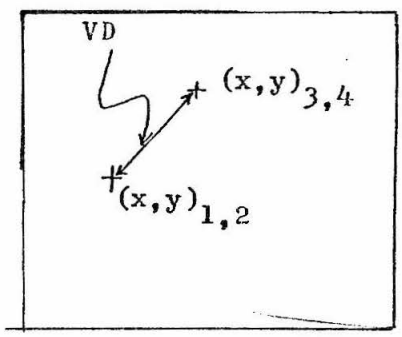

The plane $z = z_v$ where VD is minimized

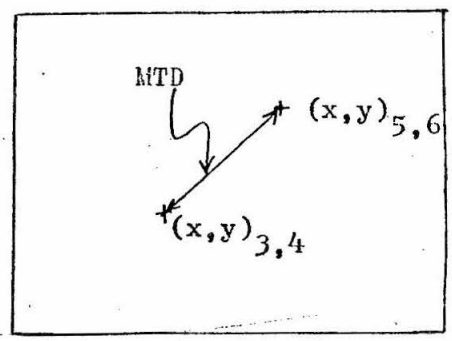

Magnet center plane

the wsc fiducials[3.4], we can derive the two-dimensional position of each spark from the digitized spark number. Since no track can leave two sparks in any one coordinate, this gives a maximum of 4^4 combinations of possible tracks.

We accept only tracks which satisfy the following:

1. A loose criterion for straightness. The reconstructed track is obtained by a least-square fit.
2. We allow at most one missing spark.
3. The track must have a slope which is topologically acceptable.

These conditions are implemented by using a procedure developed by M. Hind[3.5].

(b-iii) Procedure for Removing Spurious Tracks

The topology of a backward elastic event precludes the existence of more than one event-associated track in any region. For regions having more than one track, the spurious track is removed using topological and counter information. This applies to about 25% of the events.

Before we describe the procedure, we must say a few words about backward elastic event topology. The tracks from regions 3 and 5 (see Figure 3.1a) should meet at the center of the magnet since they belong to the same particle. No scattering between region 3 and 5 is allowed. The same is true for the tracks from regions 4 and 6. This condition should be satisfied by good events except for multiple scattering, chamber resolution, etc.. We can define a quantity to measure the degree of agreement with this condition. This quantity,

which we call Magnet Track Deviation (MTD) is defined as the deviation between $(x,y)_{3,4}$ and $(x,y)_{5,6}$ where $(x,y)_{A,B}$ is the track position at the plane of the magnet center for the tracks from regions A and B. We demonstrate this quantity in Figure 3.1b.

There must be one and only one scattering between regions 1,2 and regions 3,4. This implies that the tracks from regions 1,2 must meet those from regions 3,4 at a common point except for multiple scattering, etc. Again, we can define a quantity to measure this -- Vertex Deviation (VD), which is defined as the minimum value of the three-dimensional deviations between $(x,y,z)^{1,2}$ and $(x,y,z)^{3,4}$ (where x and y are the horizontal and vertical position for the tracks from regions 3 and 4 at z = z). The definition of VD is also shown in Figure 3.1c.

These topological quantities will be studied in detail in Section (c-ii) where we use these quantities to cut out the background. It is sufficient to say now that the typical size of MTD and VD for good events are 0.5 and 0.1 cm, respectively.

The procedure for removing spurious tracks is:

1. If there is more than one track in region 1 or 2, we reject any track with large angle (more than 70 mr) w.r.t the beam line or far away from the beam line (more than 5 cm away). This ensures that we are only dealing with the beam track which passes through the aperture counters.
2. In regions 1, 2, and 5, we can use the counter information. The counter hodoscopes Hx and Hy are situated right next to the first set of wsc (region 1 and 2) while the vertical counters R_0

to R_3 are situated next to the third set of wsc and thus can help us remove spurious tracks in regions 1, 2, and 5 (R counters cannot give any information of the vertical position of the trajectory). We extrapolate the tracks to the plane of the counters and require the appropriate counter to be hit. Extra tracks arriving outside the 50 nsec coincidence gate of the counters can thus be removed since they are not associated with the triggered event.

3. Now we use the quantity MTD (magnet track deviation) defined in the last page. Since the correct combination of tracks from regions 3,4,5, and 6 should have a small value of MTD (of order 0.5 cm), we pick the combination with the smallest MTD as the correct tracks.

4. Finally, there remains about 1% of the reconstructed events which still have spurious tracks in regions 1 and 2. The spurious tracks are rejected by accepting the two tracks in regions 1 and 2 which, when combined with the tracks in regions 3 and 4, give the vertex of interaction (the position where VD is minimized) -- see Figure 3.1) which is closest to the center of the target. This process is relatively unimportant since only 1% of the reconstructed events is affected.

This procedure enables us to obtain a unique set of tracks for each event except those discarded due to missing tracks in some regions. We can now derive the topological and kinematical properties of each event such as the momentum and angle of scattering and use them to separate backward elastic events from background.

(b-iv) Reconstruction Inefficiency

The trackfinding and spurious track removal procedures may be inefficient. We must find out about the size of this inefficiency and understand how it will affect our normalization.

A detailed analysis of the inefficiencies was undertaken. The details of this analysis and its results is fully described in Appendix C. We will, in the following few paragraphs, describe briefly the methods we used and the answer we obtained.

First, we convinced ourselves that our criteria for straightness, slope, and position of acceptable tracks are reasonable. A study of the slopes and positions of good backward elastic events indicates that our criteria are loose enough. Our criterion for straightness involves calculation of a chi-square for each combination of track sparks. Distributions of chi-square for tracks also indicate that our cut is loose enough.

Any inefficiency in trackfinding must therefore be due to missing sparks. Wsc inefficiency can be calculated based on the relative number of tracks with one spark missing and the number of tracks which have all four sparks. We must assume that the inefficiency of each wsc is not correlated with that of any other wsc. This type of inefficiency is basically an equipment inefficiency and will be handled later in the section on apparatus inefficiency.

However, it is known that efficiency for two sparks in one wsc is lower than efficiency for one spark in the same wsc[3.6]. Also, since our wsc can only accept up to 4 sparks, the efficiency for more than 4 tracks must be drastically lower than that for one track.

This correlated inefficiency is important if there are many tracks or extra sparks. Regions 3-6 have few extra sparks or tracks (typically about 10% of the events have more sparks than can be accounted for by one track). Correlated inefficiency is thus expected to be small (less than 1%). This is verified by finding very few events which have only two sparks in a region 3,4,5 or 6 indicative of a track with two missing sparks. In regions 1 and 2, more than 1/2 of the events have extra sparks. Detailed study of this region (described in Appendix C) involving scanning computer plotted pictures of spark positions[3.7] and artificially inserting a beam track when no beam track is found gives us the result that there is an inefficiency of 3% in addition to the wsc uncorrelated inefficiency.

Thus, the trackfinding inefficiency is 3% in addition to the wsc uncorrelated inefficiency.

We study the spurious track removal inefficiency by 1) using an alternate method of spurious track removal, and 2) looking at the second best combination of tracks in case we use topology to decide on the best tracks. We find a 2% inefficiency in the spurious track removal procedure we used.

These efficiency studies are done for different incident momentum, different wsc efficiencies, and different beam halo rates. No strong correlation of the inefficiency with momentum wsc uncorrected inefficiency or rate has been detected.

Thus, for our entire data, there is an over-all inefficiency in reconstruction of 5%.

(b-v) Analysis of the Triggered Events which Fail the Reconstruction Process

We claimed that the trackfinding inefficiency is the sum of the uncorrelated wsc inefficiency (which is between 1-5%) plus an additional correlated inefficiency in regions 1,2 of about 3%. If this is so, we must be able to account for the large number of triggered events (about 35%) which fail the reconstruction process (i.e., missing a track in some region).

Region 1 and 2 (at the first set of wsc)

The trigger condition requires a count in both S_2 and S_3. As seen in Figure 2.2, this necessarily implies that a particle passes through the first set of wsc. Yet, 5% of the triggered events miss a track in either region 1 or 2. This is reasonable since uncorrelated wsc inefficiency is typically 1% while there is an additional correlated wsc inefficiency of 3% in regions 1 and 2.

Regions 3 and 4 (the second set of wsc)

About 5% of triggered events miss tracks in regions 3 or 4. Now S_3 and the P counters are required in the trigger condition. Since P counters cover an area smaller than the sensitive area of the second set of wsc, one also expects that a particle should have gone through regions 3 and 4.

Typical uncorrelated wsc inefficiency for the second set of wsc is about 1%. The remaining 4% might be accounted for by scattering or the fact that S_3 is actually quite far from the second set of wsc. Scattering might give a track which is not straight enough to be acceptable. In addition, $\bar{p}$ going into $\bar{n}$ forward which annihilates in

the P counter would also fail to have a track in the second set of wsc ($\bar{p}p$ going into $\bar{n}n$ is typically 10% of the total cross section[3.8] and about 5% of the $\bar{n}$'s, if it strikes the P counters, will interact to give a final-state charged particle). Thus, we conclude that the 5% missing track events in the second set of wsc is reasonable.

Regions 5 and 6 (the third set of wsc)

Approximately 30% of the triggered events have no track in regions 5 or 6. However, the wsc does not cover 15% of the counter area. The remaining 15% of missing track events may be accounted for by 1) events where particles strike the pole face of the magnet giving tracks in regions 5 and 6 unacceptable by our slope criterion for trackfinding (observed to be about 2%). 2) $\bar{p}p$ into $\bar{n}n$ at the P counters or the pole face of the magnet where the $\bar{n}$ interacts at the R counters to give a count there (this could account for about 5% to 10% of all triggered events). 3) Events indicating beam interacting with the aluminum frame of the wsc so that the T-R counter is triggered by one of the resultant products (about 5%).

Although the reasons given are not entirely satisfactory, it would appear that most of the missing track events can be accounted for.

c. Selection of Backward Elastic $\bar{p}p$ Events

(c-i) Introduction

Having reconstructed the event trajectories, we can proceed to select the backward elastic events. To do this, we use several quantities derived from the event trajectories as well as the velocity information from the Cherenkov counter and the time-of-flight system.

The first criterion we use is the topology of the event. As

mentioned in pages 68 (Figure 3.1) and 69, the requirement that there is no additional scattering other than the backward elastic scattering forces any good backward elastic event to have small values of MTD (magnet track deviation measuring the deviation between the tracks from regions 3 and 4 and the tracks from regions 5 and 6 at the magnet center plane) and VD (vertex deviation measuring the closest approach between the incoming $\bar{p}$ track and the recoil proton track). We thus reject any event with large values of MTD or VD. The procedure for the rejection is described in (c-ii).

The second criterion used to reject background is the reconstructed vertex (which is the point of closest approach between the reconstructed $\bar{p}$ beam track and the reconstructed recoil proton track). We require this reconstructed vertex to be inside the hydrogen target. We handle this cut in Section (c-iii).

We use the velocity and momentum information as our third and fourth criterion. Knowing the momentum of the forward outgoing particle allows us to decide whether the event fits the elastic kinematics. Knowing the velocity in addition to the momentum of the forward particle enables us to decide the validity of our assumption that the forward particle is a recoil proton.

We are able to reject all background by using these criteria. We shall list briefly a summary of our reconstruction and selection procedures in terms of the amount of triggered events which pass each stage.

1. About 65% of all triggered events can be reconstructed successfully.

2. About 40% of all triggered events have MTD and VD which are acceptable.
3. About 25% of all triggered events have, in addition, a reconstructed vertex which is acceptable.
4. Finally, the number of backward elastic events (i.e., those in addition to the above, pass our velocity and momentum criterion) is about 0.5-1.5% of all triggered events.

The inefficiency in reconstruction is 5%, in MTD and VD cuts is 0%, in vertex cuts is 0% (except for those events where cos θ_{cm} is less than -0.99. The typical inefficiency for the cos θ_{cm} bin between -0.98 and -1.00 is 7%) and in velocity cuts is 2% and in momentum cuts is about 3%. Thus, the cumulative inefficiency in reconstruction and selection is slightly more than 10%.

(c-ii) Topology Selection Criterion (Cutting on MTD and VD)

As mentioned on pages 68 (Figure 3.1) and 69, we expect the values of MTD and VD to be small for backward elastic events we wish to accept. This is due to the requirement that we accept only those events with one single backward elastic scattering. The MTD and VD should be 0 except for the deviation of the reconstructed tracks from the actual event tracks due to multiple scattering and wsc resolution. In addition, the MTD is a small non-zero number even for the actual track if the entrance and exit angles of the recoil proton trajectory w.r.t to the magnet are not the same. The distribution of these quantities for good elastic events is expected to peak near 0 and drop off rapidly away from 0. Therefore, to find out where we

should make a cut, we must look at the actual distribution of MTD and VD for good backward elastic events.

Figure 3.2 shows the distribution of VD and MTD for some typical backward elastic events. We see that the standard deviations of VD and MTD are about 0.1 and 0.5 cm, respectively. The shape appears to be similar to a Poisson distribution. We have chosen 1 and 5 cm as the limits for VD and MTD, respectively and essentially no elastic events with good topology are lost by these cuts. The background level is very low and we estimate that less than 1% of the events within our cuts are events with either additional large angle scattering or events where the track in some region does not belong with the rest of the event.

About 5% of all reconstructed events fail the VD criterion. Looking at computer drawn pictures[3.9] of these events shows that these events probably have more than 1 scattering between the first and second set of wsc. About 30% of the reconstructed events fail the MTD cut. Half of these events have tracks in the regions 3,4,5 and 6 suggesting that there is an additional scattering between regions 3 and 4 and regions 5 and 6. The scattering center often appears to be the pole face of the magnet or some counter. The remaining half appears to be events which scatter in air or have more than one scattering center. This may be due to the forward particle being a low momentum particle which may be bent quite drastically by the magnetic field so as to hit the side of the magnet. In any case, very few of these events have vertical tracks in region 4 and 6 which are parallel, which is necessary for acceptable backward elastic event

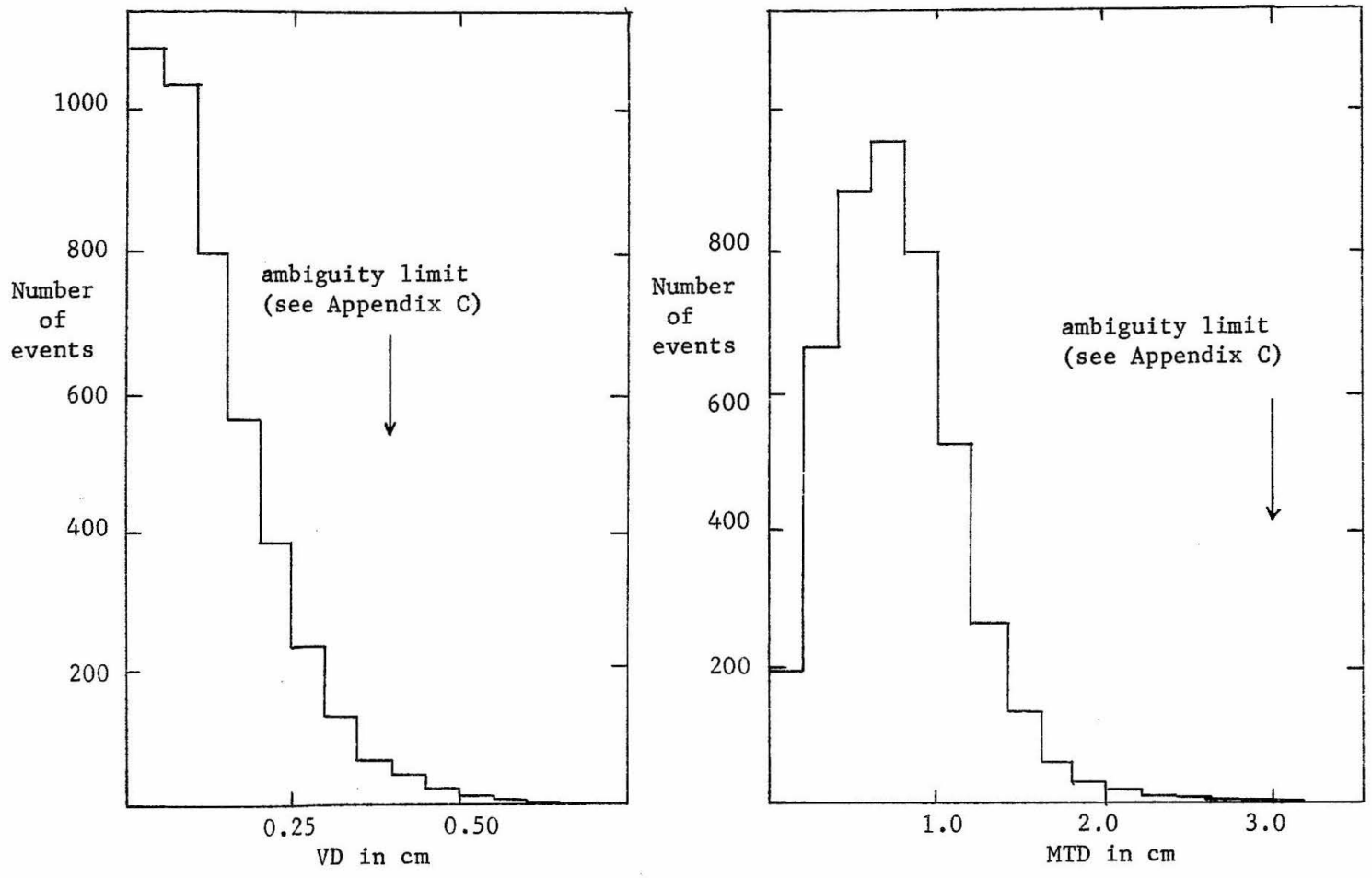

Figure 3.2: Distribution of VD and MTD for backward elastic events. Note that the MTD peaks away from 0 due to the difference in horizontal entrance and exit angles into the magnet making MTD $\neq$ 0.

topology.

The topology criterion thus removes about 35% of all reconstructed events (or 25% of all triggered events) with no significant loss (less than 1%) of backward elastic events.

(c-iii) Reconstructed Vertex Criterion

We are only interested in the backward elastic events associated with the hydrogen in the target. Thus, we must find a way of removing all other backward elastic events from our signal.

The position of the interaction vertex can be reconstructed using the tracks from regions 1-4. The z position of the reconstructed vertex is the plane of z where the tracks from regions 1 and 2 deviate the least from the tracks from regions 3 and 4. We show this in Figure 3.1b. We use this information to help us remove any backward elastic events not associated with the target.

We make a vertex cut at ± 16 cm, rejecting all events outside this cut. We can lose events if the reconstructed vertex is outside this cut while the actual vertex is inside this cut. We can gain events if it is the other way around. Since there is still a sizable amount (3.2 cm) of hydrogen target outside this cut, we expect the losses and gains to balance out. This is true if the scattering angle is large. However, for $\cos \theta_{cm}$ less than -0.998, a small change in slope or intersect due to multiple scattering or chamber resolution causes a large change in the reconstructed z position of the vertex. Thus, a large number of backward elastic events are lost which are not balanced by the number gained. In general, this causes a typical loss

in the angular bin between -0.98 and -1.0 of about 7%. This result has been obtained by comparing our usual vertex procedure with several alternative procedures detailed below.

1. We obtain the number of events inside a ± 8 cm cut and compare it with the number of events inside the ± 16 cm cut. Typically, except for the first bin (where $-1.0 = \cos \theta_{cm} = -0.98$), the two numbers are in a ratio of 1/2 to within statistics (which is typically 10%).

2. Since about 18% of the target hydrogen remains outside the ± 16 cm cut, we expect and find about 18% more backward elastic events outside our cut (except in the first bin).

3. For several momenta, we took data with target empty of hydrogen. The actual hydrogen associated events number will be the target full number minus the target empty number. It turns out that the rate of backward elastic events for an empty target is typically less than 5% of the full target rate and the statistical error is very poor (usually we have 0 or one empty target event per angular bin). Nevertheless, the results obtained with this procedure agrees with our usual procedure except in the first bin.

At each momentum, we calculate the correction in our first bin by using number 1, 2 and (if we took empty target data at that momentum) 3 procedures mentioned above. The correction is typically 7%.

About 15% of all triggered events are rejected due to a vertex outside the ± 16 cm cut. 25% of all triggered events still remain. The inefficiency of this cut is less than 1% except at the first bin. Note that we use only 32 cm of hydrogen target in our final calcu-

lation of dcs (differential cross section).

(c-iv) Velocity Criterion

The next criterion we use to select backward elastic events is the velocity criterion. We can remove most of the pion background from the recoil protons by considering the gas Cherenkov and time-of-flight information. As mentioned in Chapter II, Sections (c-iv) and (c-v), the gas Cherenkov pulse-height channel exceeds channel 24 for about 80% of the pions above 1.2 GeV/c and less than 2% of the protons while the time-of-flight system can separate protons from pions below 1.2 GeV/c. For each momentum, we select the limits of our cut in the time-of-flight system delay channel such that combined with a gas Cherenkov pulse-height channel cut at channel 24, we lost of the order of 2% of protons. For example, Figure 3.3 shows a plot of $(MM)^2$ - $(M_p)^2$ (where $(MM)^2$ is the missing mass squared assuming the $\bar{p}p$ going into a proton plus the missing mass), for events inside (3.3a) and outside (3.3b) our velocity cuts. For the backward elastic events, the missing mass is a proton so that we expect the events to peak near $(MM)^2 - (M_p)^2$. If the forward particle is a pion, we should get no peak near $(MM)^2 - (M_p)^2$.[3.10] Indeed, in Figure 3.3b, except for a small peak which is due to proton leakage, no peaking is observed. The leakage is about 2% of the peak in Figure 3.3a. Thus the loss for this velocity cut is about 2%. Loss due to the velocity cut is studied for each momentum. The losses are about 2% to within statistics. Hence, we apply a 2% correction to all momenta for this loss[3.11].

The number of remaining triggered events cut by the velocity criteria varies considerably with the momentum. At low momentum,

Figure 3.3: $(MM)^2 - M_p^2$ distributions for events (a) passing and (b) failing our velocity criterion for protons.

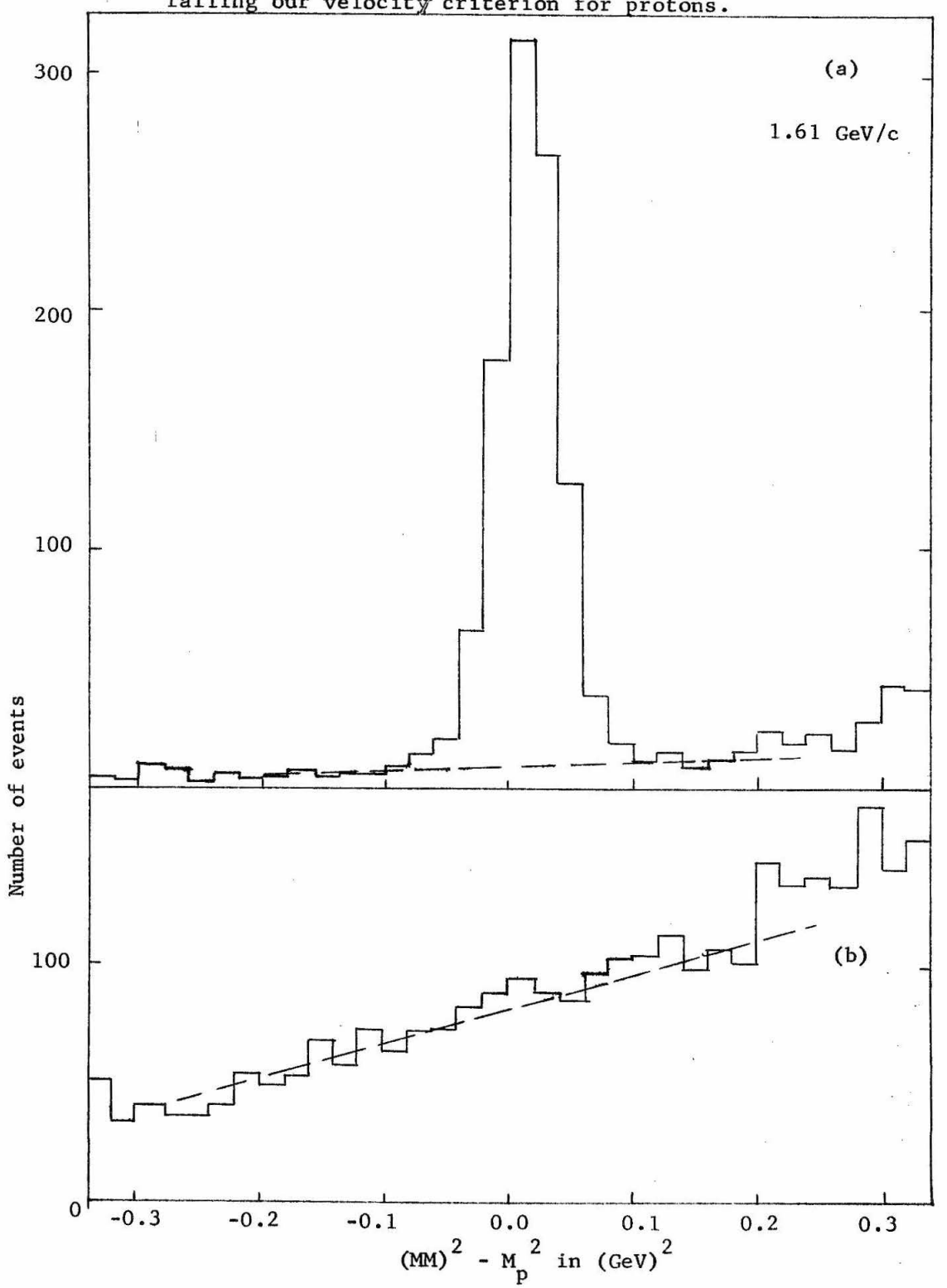

the cuts remove all but approximately 2% of the triggered events while at the higher momentum, the number of events surviving this cut could be up to 20% of all triggered events.

(c-v) Momentum Criterion

The final criterion used to select backward events utilizes the momentum of the forward particle. However, since not all the pion background is removed, we cannot use a simple cut procedure to obtain the backward elastic events. We use a background subtraction procedure.

In Chapter II, Section (b-iii), we described the way we measure the forward particle momentum. We also mentioned how we calibrate the incident $\bar{p}$ momentum. Assuming that the target particle as well as the forward particle are protons, the four-vector of the missing particle is completely determined. If the missing particle has mass near the proton mass, then the interaction must be elastic. Any inelastic strong interaction of $\bar{p}p$ producing a proton going forward must produce at least one nucleon and one pion in addition. The missing mass would then be very much larger than the proton mass. Studies show that our experimental resolution is such that we will not confuse an elastic event with an inelastic event. For future reference, we should note that the studies also indicate that inelastic missing masses would have $(MM)^2 - (M_p)^2$ (missing mass squared minus proton mass squared) larger than 0.2 GeV/c.

Figure 3.3 shows a distribution of $(MM)^2 - (M_p)^2$ for events passing all other criteria. We note that the background level is

much lower than the signal level. Thus, we can approximate the background by a linear function of $(MM)^2$ (shown as the dashed line in Figure 3.3a). The linear function is obtained by fitting the data in the bins adjacent to our signal bins. In the case of Figure 3.3a, the signal bins contain those events with $(MM)^2 - (M_p)^2$ between -0.1 and 0.1 GeV^2 and the background bins we use to obtain the linear function contain those events with $(MM)^2 - (M_p)^2$ between -0.2 and -0.1 and between 0.1 and 0.2 GeV^2. The limits of our signal bins are chosen to be at least 3 standard deviations away from the elastic peak. Thus, we expect the amount of real background elastic events mistakenly in the background bins to be very small. The amount of loss of elastic events is evaluated at each momentum. These evaluations are based on studies with narrow velocity cuts which remove as much pion background as possible. The average loss is about 1-1/2% which produces a normalization error of 3% since events in the background bins result in double subtraction. We never have to use events with $(MM)^2 - (M_p)^2$ larger than 0.2 GeV^2 as background so that inelastic proton contamination does not cause any problem. We apply a 3% correction for this loss at all momenta[3.12].

The resultant numbers of backward elastic events are obtained for each angular bin in $\cos \theta_{cm}$ of 0.02. The differential cross section can thus be obtained if we know the normalization corrections and angular acceptances of our apparatus for each angular bin.

d. Corrections to the Normalization

In order to obtain the correct normalization, we must find out

the necessary corrections. In Table 3.1, we list the sizes of all non-zero corrections at each momentum. We have lumped all corrections of less than 1% into a combined column labeled "Miscellaneous Corrections" which is estimated to be 3% at all momenta. In the following paragraphs, we will discuss all the corrections.

Reconstruction inefficiencies

As mentioned in Section (b-iv) and in Appendix C, the reconstruction inefficiency is 5% consisting of 3% correlated wsc inefficiency and 2% spurious track removal inefficiency.

Selection criteria losses

The selection cut losses are discussed in Sections (c-i) to (c-v) and we concluded that the loss due to:

1. Topological cut (cuts in MTD and VD) is less than 1%.
2. Reconstructed vertex cut is less than 1% (except for $\cos\theta_{cm}$ less than -0.98, the first bin, where the loss is typically 7%).
3. Velocity cut is 2%, and
4. Momentum subtraction procedure is 3%.

Apparatus inefficiencies

Apparatus inefficiencies could arise from inefficiencies in beam counter, trigger counter, trigger electronics, wsc system, readout-computer interface system and in tape system.

Inefficiencies in beam counter do not affect our normalization since the same counters count $\bar{p}$ flux. Inefficiencies in trigger counters have been studied using the overlap regions between two adjacent counters and the extrapolated positions of the particle

Table 3.1: Sizes of all corrections at each incident momentum in %. Only those corrections which are larger than 1% are listed separately. All corrections less than 1% are lumped into the miscellaneous correction of 3%. Actual correction applied at each momentum is larger than the sum of all corrections since (1) corrections should be applied by multiplying by (1/(1-% correction) rather than (1+% correction) since these corrections are for losses and inefficiences and (2) corrections should be applied one after the other.

Incident Momentum (GeV/c)	Recon. Ineff.	Vel. cut loss	Mom. loss	Wsc Ineff.	Counter Ineff.	Beam abs.	Misc. Corr.	Sum of all corr.	Actual corr. Applied
0.703	5.0	2.0	3.0	0.1	1.3	13.2	3.0	27.6	31.0
0.812	5.0	2.0	3.0	0.1	1.3	11.8	3.0	26.2	29.4
0.873	5.0	2.0	3.0	0.5	1.3	10.9	3.0	25.7	28.8
0.935	5.0	2.0	3.0	0.2	1.3	10.0	3.0	24.5	27.4
0.987	5.0	2.0	3.0	0.8	1.3	9.6	3.0	24.7	27.7
1.115	5.0	2.0	3.0	0.6	1.3	9.2	3.0	24.1	27.0
1.338	5.0	2.0	3.0	2.6	1.3	8.8	3.0	25.7	28.6
1.447	5.0	2.0	3.0	2.8	1.3	8.5	3.0	25.6	28.5
1.590	5.0	2.0	3.0	4.0	1.3	8.1	3.0	26.4	29.6
1.610	5.0	2.0	3.0	2.6	1.3	8.1	3.0	25.0	27.9
1.716	5.0	2.0	3.0	4.1	1.3	7.9	3.0	26.3	29.5
1.797	5.0	2.0	3.0	1.8	1.3	7.7	3.0	23.8	26.7
1.844	5.0	2.0	3.0	4.3	1.3	7.7	3.0	26.3	29.5
2.032	5.0	2.0	3.0	5.6	1.3	7.3	3.0	27.2	30.3
2.155	5.0	2.0	3.0	3.2	1.3	7.0	3.0	24.5	27.5
2.370	5.0	2.0	3.0	6.0	1.3	6.6	3.0	26.9	30.0

trajectories. The number of coincidences is compared with the number of singles and an inefficiency can be derived for each counter. Based on a study involving 30,000 triggered events, we found that the inefficiencies in P, R and T counters ranges between 0 - 0.4%, 0.0 to 0.4% and 0.5 to 4.0%, respectively. The over-all P, R, and R counter hodoscope inefficiencies are 0.1%, 0.1% and 1.1%, respectively. Thus, the trigger counter inefficiency is a total of 1.3%.

The inefficiencies in trigger electronics, readout-computer interface and tape system are found to be less than 1% each. The inefficiencies are continuously monitored and any data with inefficiencies in these systems in excess of 1% are discarded.

The inefficiencies of the wsc (wire spark chambers) can be obtained if we assumed that the inefficiencies are uncorrelated. Then the inefficiency of each chamber in a set of four wsc can be derived from the relative number of four spark tracks and three spark tracks in which a spark is missing in that particular chamber. We found that the combined inefficiency of the three sets of wsc lies in the range between 0.0% and 6.0%. They are listed in Table 3.1 for each momentum. In section (b-iv), we mentioned that there is an additional correlated wsc inefficiency in the first set of wsc. However, this is considered a reconstruction inefficiency. We have also studied the possibility of dead spots in the wsc by looking at the number of tracks and the number of missing sparks inside 2.5 by 2.5 cm bins for each wsc. We did not find any cluster of bins (4 to 10 bins) with abnormally low number of counts or high number of missing sparks. Thus, we did not detect any dead spots.

Beam and Flux Corrections

These corrections include beam absorption corrections, wrong momentum and wrong particle (i.e., non-$\bar{p}$) contamination corrections and corrections due to some beam particles not going through all of the target.

A certain amount of beam particles are absorbed (i.e., suffer interactions) in going through the target. Thus, the effective beam going through the entire target is less than the beam counted by the beam counter system. The amount of beam absorption can be calculated from well-known total cross section and elastic cross section data[3.13]. Typically, inelastic interactions absorb the beam while only large angle elastic scattering absorbs the beam effectively[3.14]. The correction necessary due to beam absorption is given for each momentum in Table 3.1 and is typically 8%.

Beam contamination by non-$\bar{p}$'s is discussed in Section (b) of Chapter II where we discussed the beam counting system. The contamination level is less than 1%. Beam contamination by wrong momentum $\bar{p}$ has been studied and found to be of the 1% level. However, this contamination is the major cause of our momentum selection cut inefficiency since if we misjudge the incident momentum by a sufficient amount, any backward elastic event would not have good enough kinematics to be accepted as a backward elastic event. Thus, this contamination has already been corrected for by the correction for the momentum selection procedure.

Less than 1% of the beam would miss any part of the target if the beam particle does not interact. This is ensured by the

placement of the three aperturing counters.

Trigger condition inefficiency

The trigger condition has a veto requirement (see Chapter II Section (c)) which may veto some of the real backward elastic events. The veto is triggered when there is a forward negative particle with momentum close to the incident momentum. This is possible since the final state $\bar{p}$ will annihilate and thus may release some high momentum pi minuses. However, since the annihilation is essentially at rest, any pions emitted will probably be released isotropically. Then, the veto would be satisfied only if the pion goes forward inside a solid angle of 1/30 sr or 1/360 of the entire solid angle. Since the average number of pi minus released by $\bar{p}p$ at rest is about 1 or 2, the probability of the veto condition being satisfied for a backward elastic event is less than 1%.

Miscellaneous Corrections

Several of the corrections mentioned above are less than 1%. They are not listed separately in Table 3.1 The combined correction due to all these small corrections is estimated to be 3% and is not a function of incident momentum.

e. Monte Carlo of the Apparatus Acceptance

In order to calculate the differential cross section, we need to know how much solid angle for each angular bin is accepted by our apparatus. We only accept backward elastic events which have appropriate particles passing through the various trigger counters and the sensitive areas of the wsc. We use a Monte Carlo program to

generate events and follow the trajectories to see if they go through the necessary apparatus[3.3].

Interactions are generated inside the hydrogen target with the interaction vertex distributed according to beam characteristics. The z vertex (along the beam line) is distributed randomly inside the target except for a bias to simulate absorption of beam. The x and y distributions are gaussian with the parameters obtained from calibrating the beam[3.15].

We follow the path of each recoil proton from the generated event, correcting for multiple scattering and nuclear interaction. Any event having recoil proton trajectory failing to pass through a required area is rejected. Other events which will have unacceptable reconstructed kinematic or topological quantities due to large angle nuclear scattering are also discarded.

For $\cos \theta_{cm}$ bin of 0.02, we generate M events with random $\cos \theta_{cm}$ inside that bin. The φ is also generated randomly inside some limit φ_0 chosen such that any event with abs(φ) greater than φ_0 cannot possibly be accepted by our apertures. This is true for $\cos \theta_{cm}$ away from -1.0 since our apparatus acceptance is skewed -- it covers large positive x regions but does not cover large negative x regions. If N events succeeded, the proportion of the solid angle of the angular bin which we accept is then (N/M time φ_0 (in radians)/ 3.1416.

Two separate programs[3.16] have been written to check for consistency and the results are in agreement. Similarly, a ray trace program[3.17] also gives results agreeing with the Monte Carlo

program results.

In Figure 3.4 we show a typical acceptance percentage curve at one incident momentum. The acceptance is typically 40% for the first bin (cos θ_{cm} between -1.0 and -0.98) and drops off to a 10% shoulder at the fourth or fifth bin. Then, the percentages drop rapidly to zero in two or three bins. We have decided to discard all bins which have an acceptance percentage of less than 5% since the percentages for such bins are unreliable due to the reasons discussed below.

Errors and uncertainties may be introduced into this procedure. Angular biases are easily introduced if our inputs (beam characteristics, position of apparatus, etc.) are wrong. This bias is especially critical for the first and the last few bins we accept. We have determined that the error needed to shift the percentages for the first and the last few bins by about 5% can be any one of the following:

1. Beam momentum 1%
2. Beam position 1/4"
3. Beam slope 2 mr
4. Magnet field strength 1%
5. Horizontal position of the apparatus 1/2".

For example, the dashed line in Figure 3.4 is the percentage acceptance curve with the momentum of the beam shifted by 1%. The percentages of the intermediate bins (2nd to 4th usually) are not strongly affected by these errors.

The positions of the apparatus were measured accurately and the beam characteristics and the magnet field strength were continuously monitored. Thus, we believe that the values quoted above are upper

Figure 3.4: Typical % acceptance curve as a function of cos θ_{cm} at one incident momentum based on results of the Monte Carlo program. Dashed curve is the result of a one percent shift in momentum or magnet field strength

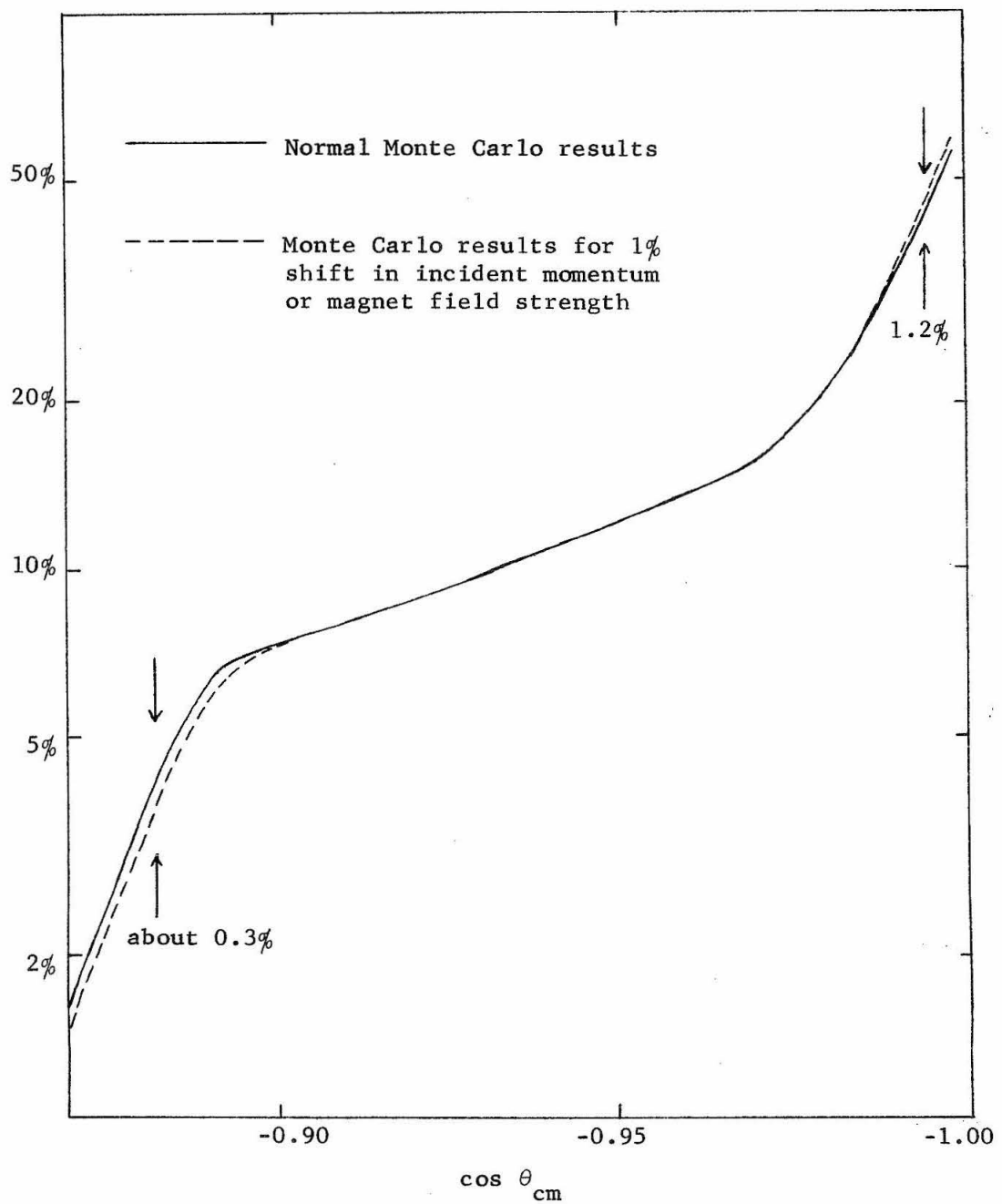

limits to the variation or inaccuracy of these quantities. We conclude that the uncertainties or error introduced into the solid angle acceptance is 5% for the first bin and for the bins with percentage acceptance less than 10%. It should be noted that the statistics of the Monte Carlo events for each angular bin is about 2% and we have smoothed the percentages acceptance at each momentum by making adjustments of 1-2%.

f. Calculation of the dcs (Differential Cross Sections) and Errors

We now proceed to calculate the final dcs (differential cross sections) S(x) and error E(x) for the angular bin centered at $\cos \theta_{cm} = x$ for each momentum.

dcs

For this bin, we have the number of backward elastic events N(x), the combined correction factor COR(x) which is in general near 30% (see Section (d)), and ACC(x), the percentage of solid angle accepted by our apparatus. Let D be the density of hydrogen in the target (which is 0.0708 gm/cm^3 in our case[3.18]), F be the net flux of $\bar{p}$'s from which we obtained the backward elastic events, A_0 be the Avogardro's number, and L be the length of target which we used (32 cm), then the dcs is

$$S(x) = 100*N(x)* (1 + COR(x))/(ACC(x)*D*F*A_0*L)$$

The factor of 100 comes from the fact that we have angular bin size of $\cos \theta_{cm}$ of 0.02 which is 1/100 of the entire solid angle.

The result is in cm^2/sr (or mb/sr within a factor of 10^{27}) and

can be converted into mb/GeV^2 by multiplying it with an incident momentum dependent factor of $3.1416/k^2$ where k is the center-of-mass momentum.

Errors

In the final dcs, we quote with it an error which is a combination of statistical and systematic errors.

The statistical errors vary between 7 and 20%. They are based on the number of backward elastic events in each bin[3.19].

All of our normalization corrections with the exceptions of beam absorption and the uncorrelated wsc inefficiency carry with them uncertainties and errors which are of the same size as the corrections themselves. For most of the corrections, the sizes are 1% or less. Thus, the errors associated with them can be ignored since the statistical error is at least 7%. The corrections which are larger than 1% include the momentum cut loss (3%), velocity cut loss (2%), reconstruction inefficiencies (3% and 2%), and, for the first bin only, the vertex cut loss (7%). The combined error is 5.1% and 8.7% (for the first bin).

The Monte Carlo of apparatus acceptance carries with it possible errors which are 5% for the first bin and bins with acceptance percentages less than 10%.

Thus, the combined non-statistical errors are:

1. For the first bin, 10.0%.
2. For bins with acceptance percentages less than 10%, 7.2%.
3. For the remaining bins, 5.1%.

When this is combined with the statistical errors, the final

errors are between 10 to 20%.

g. Summary and Assessment of the Analysis Procedure

Summary

We present in the following a brief summary of the analysis procedure. Figure 3.5 shows a flow diagram of this procedure.

1. For each triggered event, information recorded includes the digitized wsc spark positions and the counter bits (containing the signals from the gas Cherenkov counter and the time-of-flight system).
2. The event trajectories are reconstructed from the digitized wsc spark positions. We demand that there is an incident $\bar{p}$ beam track, a forward recoil proton track and a deflected (by the magnet) recoil proton track. In case of spurious tracks, counter information and topological considerations are used to remove the spurious tracks.
3. Reconstructed events having sufficient tracks are tested for the topological criteria. Events indicating additional scattering are rejected.
4. Events with reconstruction vertex outside a certain limit ($\pm$ 16 cm) are discarded.
5. Events with forward particles failing our velocity criterion are cut.
6. Remaining events are used in a background subtraction procedure (as a function of missing mass squared) to obtain the net number of backward elastic events.
7. Corrections to the normalization are calculated and applied.
8. Percentage of solid angle accepted by our apparatus is calculated

Figure 3.5: Flow chart of the analysis procedure. All percentages are approximate. The percentages of corrections are obtained by studies on inefficiencies and losses.

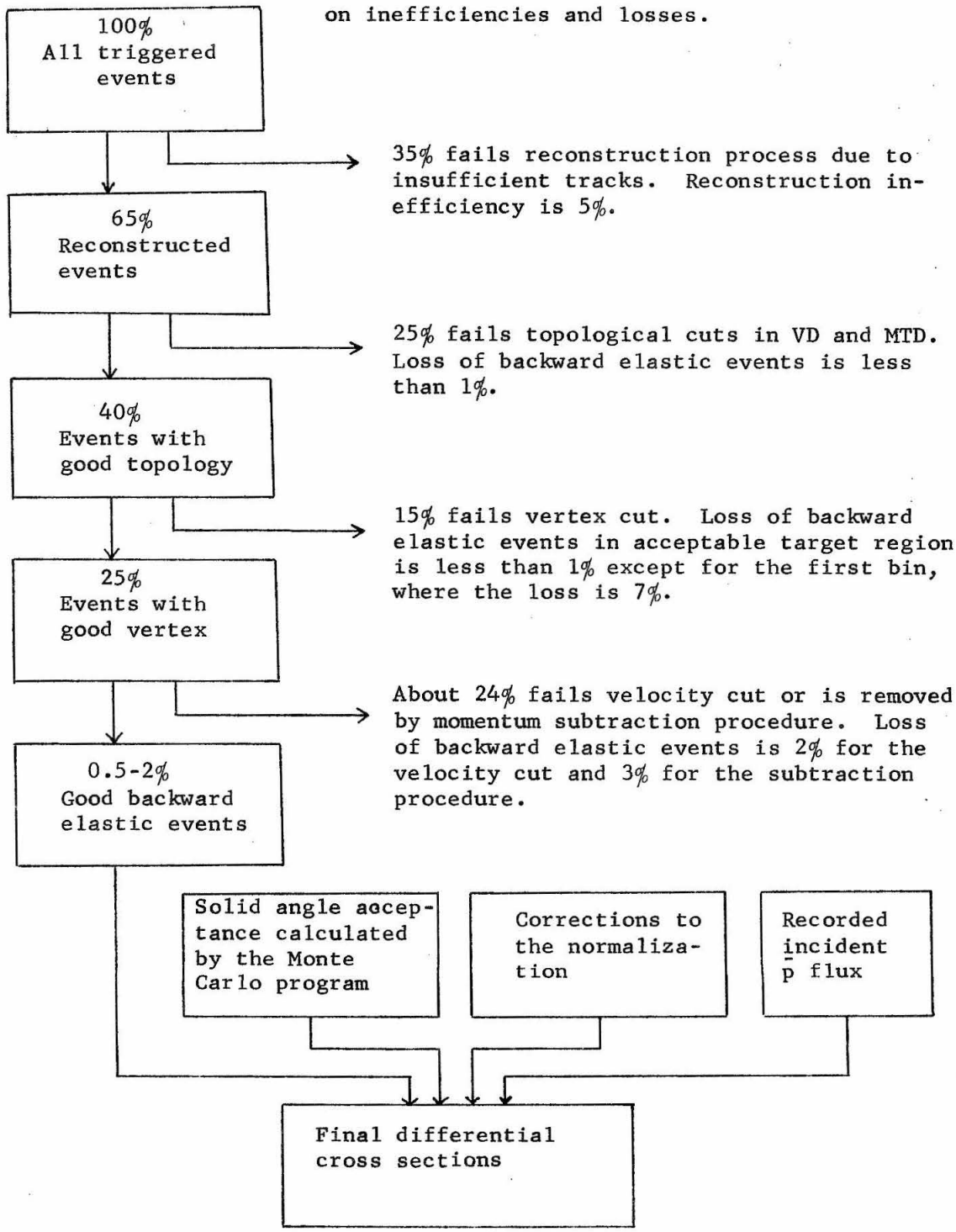

by a Monte Carlo program.

9. Differential cross section and errors are then obtained using the number of backward elastic events, percentage acceptance and normalization corrections.

Finally, Table 3.2 contains a list of quantities describing the nature and size of our data at each momentum. We give, for each momentum, the total $\bar{p}$ flux used, the number of backward elastic events, and the total solid angle accepted.

Assessment

1. Is our analysis procedure necessary and sufficient? Are there alternate methods which are more efficient in obtaining the desired results?

To answer these questions, we should first define what we want to obtain. We are interested in obtaining the differential cross section for $\bar{p}p$ backward elastic scattering on hydrogen. Thus, it is necessary that we determine the scattering angle, whether a triggered event is a backward elastic event and whether the interaction is associated with the hydrogen in the target.

In order to determine the scattering angle, we need to determine the incident $\bar{p}$ beam track and the recoil proton track. Thus, we need to record the positions of these tracks and to reconstruct these tracks. This we have done.

Now, we must find a procedure to separate backward elastic events from the background events which trigger our apparatus. As mentioned in Chapter II, the likely annihilation of the final state

Table 3.2: Properties of the analysis and data at each momentum. Momentum background is the level found by the background subtraction procedure.

Incident Momentum (GeV/c)	$\bar{p}$ flux (in 10^6)	Total cm Solid ang. (in msr.)	Number of Elastic ev.	Momentum Background (in %)	Total Correc. (in %)	Corrected No. Elas. ev. per 10^6 $\bar{p}$-msr
0.703	7.05	90.0	180	17.8	31.0	0.371
0.812	9.12	93.7	120	17.5	29.4	0.182
0.873	20.0	96.8	194	20.6	28.8	0.129
0.935	9.51	98.7	56	32.2	27.4	0.076
0.987	26.7	100.5	199	32.7	27.7	0.095
1.115	29.8	105.6	302	6.0	27.0	0.122
1.338	38.8	113.8	517	33.8	28.6	0.151
1.447	41.8	117.0	664	15.5	28.5	0.174
1.590	63.2	122.5	839	23.5	29.6	0.140
1.610	63.3	123.7	956	10.9	27.9	0.156
1.716	78.2	126.3	1082	11.8	29.5	0.142
1.797	60.3	130.0	636	20.3	26.7	0.103
1.844	73.7	131.2	809	12.0	29.5	0.108
2.032	73.5	137.0	426	17.6	30.3	0.055
2.155	81.5	145.1	367	29.7	27.5	0.040
2.370	48.4	151.7	129	37.2	30.0	0.023

antiproton is not useful since it cannot be easily distinguished from a $\bar{p}p$ annihilation in flight event. Thus, we must use the information we have on the recoil proton. We have used kinematics and the velocity of the recoil proton to help us remove inelastic interaction events. It is necessary to use the velocity criterion to remove as many forward pions as possible since it is possible for the pion background to show an enhancement (or suppression) at momentum close to the recoil proton momentum[3.20]. When we determine that the forward particle is indeed a proton, it is still necessary to reject all inelastically produced forward protons. This is done by considering the kinematics of the event. The kinematics for inelastic events with a proton in the forward direction is sufficiently different from elastic kinematics that all such background can be cleanly removed. Thus, we can use a background subtraction method to remove the small amount (about 15%) of pions which was not removed by the velocity criterion. Thus, we have identified a backward elastic event.

It should be mentioned that we reject all events which, according to the reconstructed tracks, show more than one scattering. Such events will disable our scattering angle or momentum determination[3.21].

Finally, we should reject all backward elastic events not associated with the hydrogen in the target. We found that our reconstructed vertex is a good indication of the actual vertex. Thus we make a vertex cut well inside the target and reject all events outside this cut. This procedure has been studied and is found to be

efficient except for a slight inefficiency in the straight forward direction which we correct for. Thus, we have handled all the necessary methods in obtaining our results. Our procedure is sufficient in determining the number of backward elastic events since there is no way for a significant number of non-elastic events to simulate both the recoil proton momentum and velocity.

Alternate procedures include those which involve different equipment (which we investigated in the last section of Chapter II). However, any method to obtain the differential cross section of $\bar{p}p$ backward scattering must do the things mentioned above. Thus, the main ideas of the analysis cannot be changed. We have made all possible corrections such as correcting for the ionization loss of the momentum in order to improve the quality of our analysis.

One major area in which the efficiency of our procedure can be improved is in the computing. Our two analysis programs, the reconstruction and the selection programs, each take up about 30K memory storage and requires 50 msec approximately to process each event. Since the CDC-6600 charges according to program size and the total amount of time the program is using the computer, the peripheral processing time used to read the computer tape or write the library tape turns out to be quite expensive. The additional cost is comparable to the central processing of the events. We should have used a more efficient tape handling procedure, such as double buffering[3.22].

Another way to reduce cost is to use a smaller computer to do the preliminary analysis (reconstruction)[3.23]. We could also have tightened the trigger. This would reduce the number of triggered

events to be processed. However, as we mentioned in the section on the triggering system, significant reduction in trigger rate is impossible.

CHAPTER IV: RESULTS-- $\bar{p}p$ BACKWARD ELASTIC DIFFERENTIAL CROSS SECTIONS

a. Differential Cross Sections for Each Angular Bin

We now give the dcs (differential cross section) for backward elastic $\bar{p}p$ scattering which was obtained in our experiment. We present in this section the dcs for each angular bin at each incident momentum. The angular bin size we used is 0.02 in cos θ_{cm} which corresponds to 0.004 to 0.03 GeV^2 in du. In the next section (b), we extrapolate the 180^odcs & slope at each momentum. In Section (c), we compare our data with other existing data in or near the regions which we cover. Section (d) contains a discussion of the major features observed in our data and the extrapolated data at 180^o.

In this Chapter, we use "μb" for microbarns, "p" for incident $\bar{p}$ beam momentum and "E" for center-of-mass energy which is equaled to $(s)^{1/2}$.

Table 4.1 and Table 4.2 give the dcs in μb/sr and μb/GeV^2, respectively. We have listed the central values of cos θ_{cm}, -u and -t for each bin. These values are close to, but not exactly the median or weighted average of cos θ_{cm}, -u and -t for the bins. The difference is small (typically less than 0.0005 in cos θ_{cm}).

Figure 4.1 plots the data in μb/sr at each momentum vs. cos θ_{cm}. Figure 4.2 plots the data in μb/GeV^2 at each momentum vs. u. They are both log vs. linear plots.

b. The 180^o dcs and Slope Extrapolated from our Data

The behavior of the dcs and its slope at 180^o is of great

Table 4.1: Dcs obtained from our experiment in μb/sr. P is incident momentum, E is sqrt(s), TO is T at 180^{o} and UO is TO/200. Errors are given underneath the dcs. P in (GeV/c), E in GeV and TO, UO in $(GeV)^{2}$.

-T is	TO-UO	TO-3UO	TO-5UO	TO-7UO	TO-9UO	TO-11UO	TO-13UO
-U is	UO	3UO	5UO	7UO	9UO	11UO	13UO
Cos cm is	-0.99	-0.97	-0.95	-0.93	-0.91	-0.89	-0.87
P = 0.703 UO = 0.00220	225.3	329.3	361.1	279.3	284.5	0.0	0.0
E = 1.990 TO = 0.43938	43.1	57.9	68.4	70.8	89.3	0.0	0.0
P = 0.812 UO = 0.00284	87.1	112.8	149.1	179.1	211.8	182.4	0.0
E = 2.022 TO = 0.56778	25.4	31.4	39.0	46.1	52.7	52.1	0.0
P = 0.873 UO = 0.00322	73.3	89.2	86.0	145.8	123.0	85.4	0.0
E = 2.041 TO = 0.64424	16.4	17.5	22.3	30.1	29.8	26.8	0.0
P = 0.935 UO = 0.00362	44.8	49.3	78.2	86.4	40.7	0.0	0.0
E = 2.061 TO = 0.72495	16.9	19.9	24.7	31.1	32.3	0.0	0.0
P = 0.987 UO = 0.00397	83.9	68.1	55.5	55.4	105.3	47.2	0.0
E = 2.077 TO = 0.79476	14.7	14.7	16.3	16.4	25.0	21.4	0.0
P = 1.115 UO = 0.00487	102.9	101.9	90.7	101.6	46.1	74.0	0.0
E = 2.120 TO = 0.97386	15.5	14.2	14.6	16.9	12.3	17.8	0.0
P = 1.338 UO = 0.00653	146.6	137.0	97.3	109.1	101.7	73.8	0.0
E = 2.197 TO = 1.30589	19.9	17.4	16.4	18.5	19.9	23.3	0.0
P = 1.447 UO = 0.00738	179.2	134.8	113.1	97.5	73.2	68.4	0.0
E = 2.235 TO = 1.47548	21.1	15.4	15.2	15.1	15.1	19.9	0.0
P = 1.590 UO = 0.00852	136.9	140.9	93.4	80.1	76.1	0.0	0.0
E = 2.286 TO = 1.70370	16.0	13.7	13.1	14.7	16.4	0.0	0.0
P = 1.610 UO = 0.00868	153.5	113.5	108.3	81.2	86.7	84.6	0.0
E = 2.293 TO = 1.73607	17.2	11.3	12.2	11.3	13.2	14.6	0.0
P = 1.716 UO = 0.00955	137.0	112.4	106.5	79.0	75.9	90.7	0.0
E = 2.330 TO = 1.90929	15.5	10.5	10.5	10.2	11.3	12.5	0.0
P = 1.797 UO = 0.01022	91.4	90.8	67.5	80.6	58.8	70.0	33.8
E = 2.359 TO = 2.04335	11.4	10.1	10.1	12.0	11.4	12.5	14.7
P = 1.844 UO = 0.01061	101.1	92.1	63.2	92.3	67.6	48.6	47.3
E = 2.375 TO = 2.12174	11.9	9.4	8.5	10.4	10.4	9.7	11.2
P = 2.032 UO = 0.01220	58.4	38.0	34.1	41.0	31.6	28.3	19.7
E = 2.441 YO = 2.43919	7.6	6.0	5.9	6.8	7.6	6.8	6.7
P = 2.155 UO = 0.01325	49.3	28.8	26.4	12.6	22.5	16.2	13.4
E = 2.484 TO = 2.64980	6.4	5.4	5.2	5.2	6.1	6.6	7.5
P = 2.370 UO = 0.01511	30.3	17.4	14.4	7.9	9.2	12.2	18.2
E = 2.558 TO = 3.02240	5.7	5.5	4.9	4.6	6.5	7.3	7.4

Table 4.2: Dcs obtained from our experiment in μb/GeVsq. P is incident momentum, E is sqrt (s), TO is T at 180^{o} and UO is TO/200. Errors are given underneath the dcs. P in (GeV/c), E in GeV, and TO,UO in $(GeV)^{2}$.

-T is	TO-UO	TO-3UO	TO-5UO	TO-7UO	TO-9UO	TO-11UO	TO-13UO
-U is	UO	3UO	5UO	7UO	9UO	11UO	13UO
cos cm is	-0.99	-0.97	-0.95	-0.93	-0.91	-0.89	-0.87
P = 0.703 UO = 0.00220	6443.5	9417.7	10326.7	7987.0	8317.8	0.0	0.0
E = 1.990 TO = 0.43938	1233.2	1657.0	1955.1	2023.9	2555.5	0.0	0.0
P = 0.812 UO = 0.00284	1928.8	2496.2	3299.9	3962.8	4688.0	4037.0	0.0
E = 2.022 TO = 0.56778	561.8	694.6	862.8	1021.2	1166.1	1154.0	0.0
P = 0.873 UO = 0.00322	1429.9	1739.2	1677.8	2843.6	2399.7	1665.9	0.0
E = 2.041 TO = 0.64424	319.7	340.8	434.5	586.8	581.3	533.9	0.0
P = 0.935 UO = 0.00362	777.2	854.3	1355.3	1498.2	705.7	0.0	0.0
E = 2.061 TO = 0.72495	293.7	344.5	428.2	538.4	560.2	0.0	0.0
P = 0.987 UO = 0.00397	1327.0	1077.0	877.2	875.9	1665.2	746.2	0.0
E = 2.077 TO = 0.79476	233.0	232.6	257.2	259.2	394.7	338.0	0.0
P = 1.115 UO = 0.00487	1328.4	1314.6	1169.9	1310.4	594.3	954.7	0.0
E = 2.120 TO = 0.97386	200.2	182.7	188.0	217.5	159.0	229.3	0.0
P = 1.338 UO = 0.00653	1411.1	1318.1	935.8	1049.7	978.8	710.5	0.0
E = 2.197 TO = 1.30589	191.6	167.2	157.9	177.9	191.5	224.5	0.0
P = 1.447 UO = 0.00738	1526.6	1148.0	963.1	830.2	623.8	582.6	0.0
E = 2.235 TO = 1.47548	179.5	130.9	129.5	129.0	128.5	169.4	0.0
P = 1.590 UO = 0.00852	1010.0	1039.5	689.2	591.2	561.0	0.0	0.0
E = 2.286 TO = 1.70370	117.8	101.1	96.6	108.4	120.6	0.0	0.0
P = 1.610 UO = 0.00868	1110.8	821.8	784.0	587.7	627.8	612.3	0.0
E = 2.293 TO = 1.73607	124.5	82.0	88.4	81.6	95.3	106.0	0.0
P = 1.716 UO = 0.00955	901.8	740.0	701.1	519.8	499.5	596.7	0.0
E = 2.330 TO = 1.90929	101.7	69.0	69.3	66.9	74.3	82.4	0.0
P = 1.797 UO = 0.01022	562.3	558.2	415.0	496.0	361.9	430.2	208.1
E = 2.359 TO = 2.04334	70.1	62.2	62.0	73.6	69.9	76.8	90.4
P = 1.844 UO = 0.01061	599.0	545.2	374.2	546.7	400.5	287.9	280.1
E = 2.375 TO = 2.12174	70.5	55.7	50.2	61.8	61.9	57.6	66.4
P = 2.032 UO = 0.01220	300.9	196.0	175.8	211.1	163.0	145.7	101.7
E = 2.441 TO = 2.43919	39.2	31.0	30.6	35.0	39.2	34.9	34.7
P = 2.155 UO = 0.01325	234.0	136.8	125.1	60.0	106.6	76.7	63.3
E = 2.484 TO = 2.64980	30.2	25.5	24.7	24.5	29.1	31.5	35.7
P = 2.370 UO = 0.01511	126.0	72.2	59.7	32.9	28.2	50.9	75.6
E = 2.558 TO = 3.02240	23.6	22.8	20.2	19.0	27.1	30.2	30.8

Figure 4.1: Our experimental data in μb/sr. (Solid line in the linear fit).

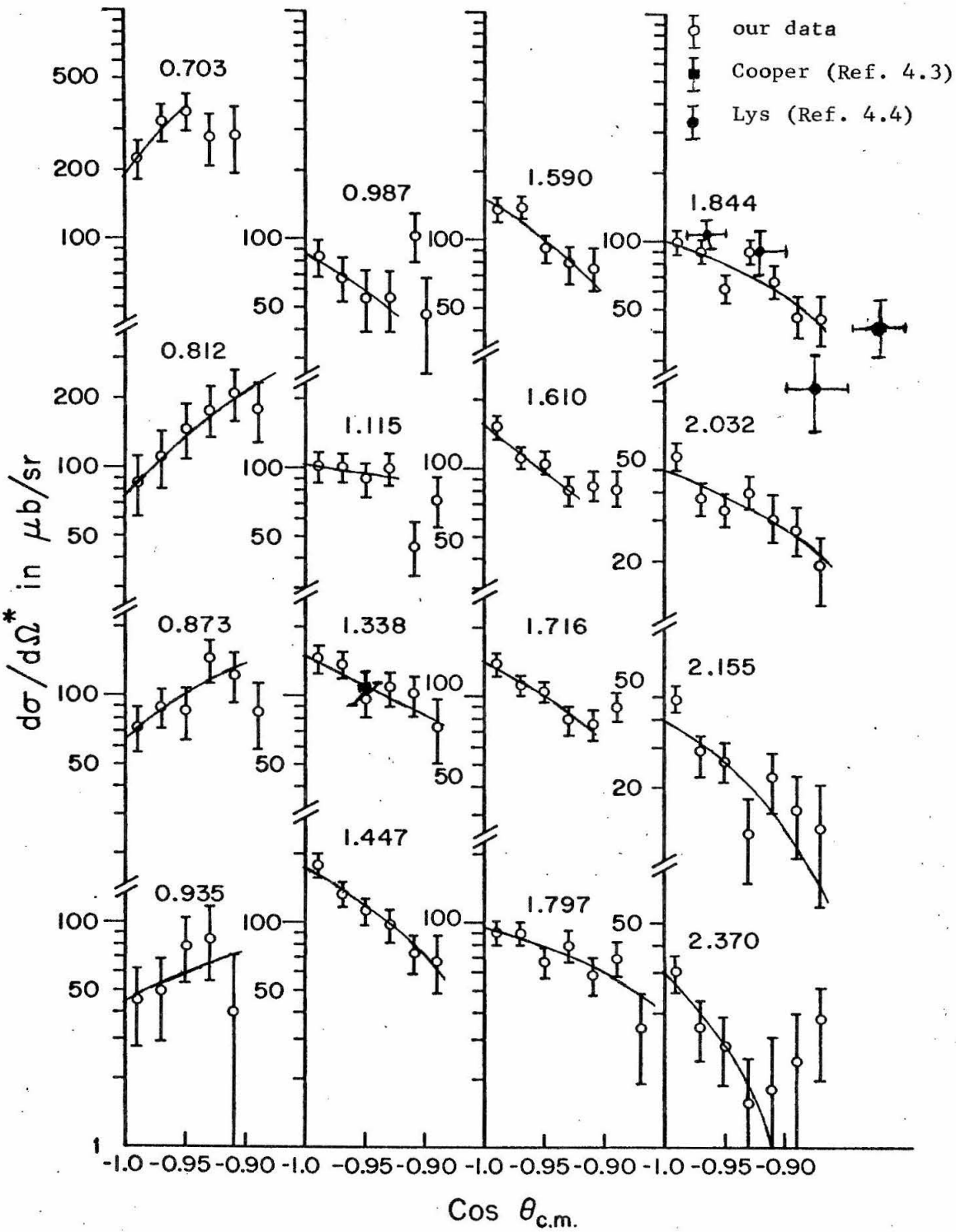

Figure 4.2 Our experimental data in μb/sr

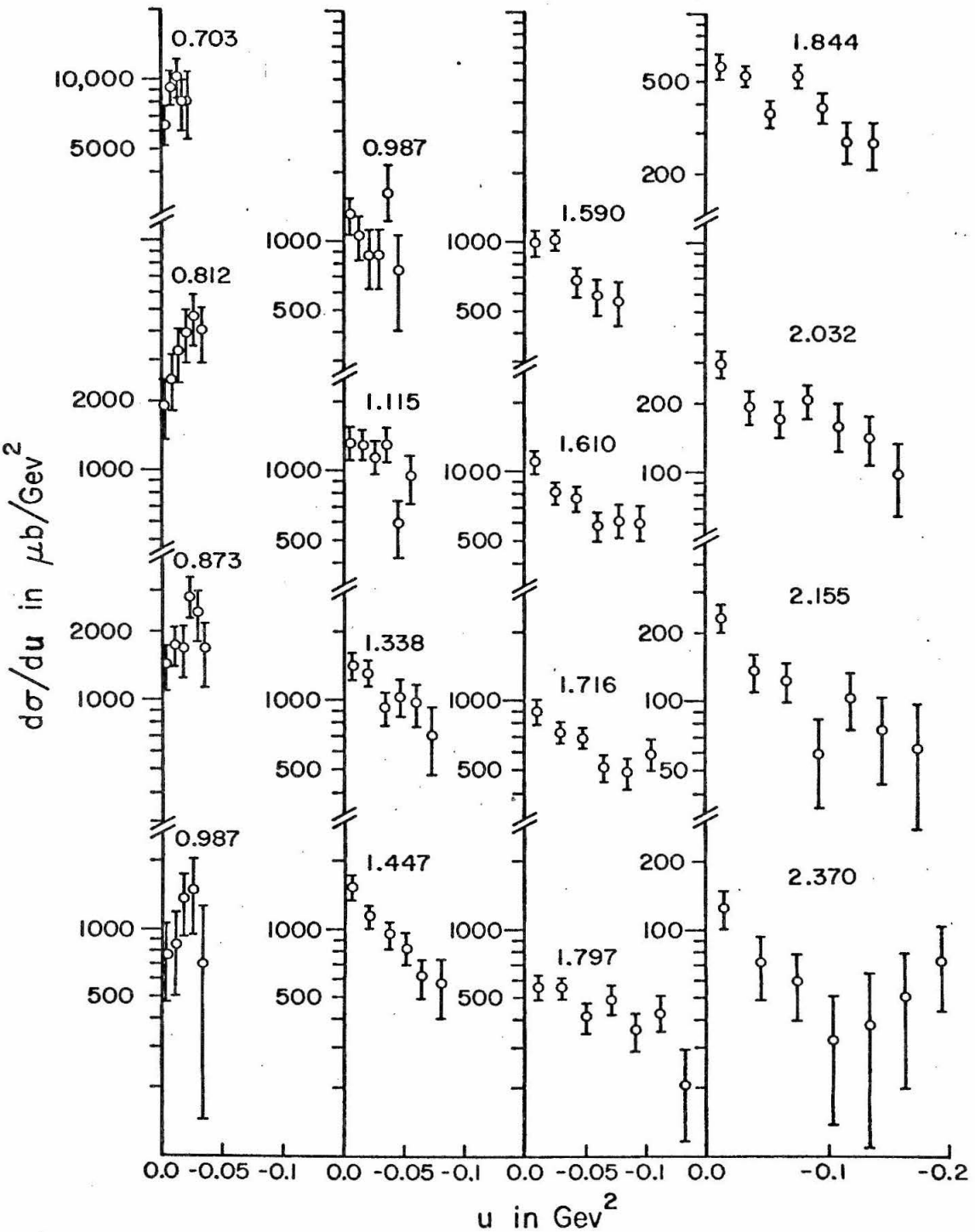

interest. At each momentum, we extrapolate these quantities from our data.

At each momentum, we have 5 to 7 angular data points. Thus, we decide to fit using only two parameters. We fit our data to both a linear function ($a + bx$ where x is $1 + \cos \theta_{cm}$) and an exponential function ($a\, e^{bx}$) using standard least-square fitting procedure[4.1]. Usually, all our data points at a momentum are used. However, in the case that the fit is poor (confidence level less than 50%), we investigate the fit neglecting one or two largest angle bins. If the fit is improved significantly, we use the results of the better fit.

The results of the linear and exponential fits are qualitatively similar. Compared with the linear fit, the exponential fit gives larger (smaller) slopes when there is backward peaking (dipping) which is expected due to the nature of the exponential function. The extrapolated dcs at 180^{o} is about the same for both fits. We have investigated the results of fitting with fewer data points and also with a quadratic function fit. The extrapolated 180^{o} dcs and slope do not vary very much, especially where the fit is good.

Table 4.3 and 4.4 give the fitted values of the 180^{o} dcs and slope for the linear and exponential fit, respectively. Figures 4.3 and 4.4 plot the 180^{o} slope and dcs of the linear fit as well as their ratio as a function of momentum in $\mu b/sr$ and $\mu b/GeV^2$, respectively. Figure 4.5 plots the 180^{o} slope and dcs for the exponential fit in $\mu b/GeV^2$. The linear fit has been drawn as solid lines in Figure 4.1.

Table 4.3 : Extrapolated 180^{o} dcs and Slope for Linear Fit $(A + B(1 + \cos \theta_{cm}))$

Pinc	E	-T	A	B	B/A	A	B	B/A	Chi sq.
(GeV/c)	(GeV)	(GeVsq)	(μb/sr)			($\mu b/GeV^2$)	($\mu b/GeV^4$)	(GeV^{-2})	Chi per.
0.703	1.990	0.4394	195.5	3648.8	18.66	5592.3	475026.6	84.94	0.26
0.0	0.0	0.0	55.9	1958.2	10.01	1600.1	254929.8	45.59	0.26
0.812	2.022	0.5678	78.2	1242.2	15.88	1731.3	96845.5	55.94	0.73
0.0	0.0	0.0	24.5	462.4	5.91	541.5	36050.8	20.82	0.18
0.873	2.041	0.6442	65.0	738.8	11.36	1268.7	44734.2	35.26	1.54
0.0	0.0	0.0	16.4	363.2	5.58	319.7	21993.8	17.34	0.51
0.935	2.061	0.7250	45.5	282.1	6.21	787.9	13488.3	17.12	2.00
0.0	0.0	0.0	17.3	384.8	8.47	300.3	18400.0	23.35	0.67
0.987	2.077	0.7948	85.7	-499.8	-5.83	1355.5	-19885.4	-14.67	0.26
0.0	0.0	0.0	15.3	348.0	4.06	241.8	13845.1	10.21	0.13
1.115	2.120	0.9739	102.8	-96.6	-0.94	1326.1	-2560.5	-1.93	0.38
0.0	0.0	0.0	15.8	356.9	3.47	203.5	9457.3	7.13	0.19
1.338	2.197	1.3059	148.7	-642.0	-4.32	1430.4	-9461.2	-6.61	2.04
0.0	0.0	0.0	15.8	245.7	1.65	152.0	3621.7	2.53	0.51
1.447	2.235	1.4755	172.0	-1054.4	-6.13	1465.2	-12173.0	-8.31	1.47
0.0	0.0	0.0	15.0	220.5	1.28	127.8	2545.7	1.74	0.37
1.590	2.286	1.7037	152.8	-952.0	-6.23	1127.4	-8243.2	-7.31	2.91
0.0	0.0	0.0	13.8	248.3	1.62	102.0	2150.1	1.91	0.97
1.610	2.293	1.7361	153.6	-1028.1	-6.69	1111.8	-8573.2	-7.71	1.26
0.0	0.0	0.0	14.9	301.9	1.97	107.8	2517.6	2.26	0.63
1.716	2.330	1.9093	139.3	-759.1	-5.45	916.9	-5233.6	-5.71	1.20
0.0	0.0	0.0	11.7	195.7	1.40	76.9	1348.9	1.47	0.40

1.797	2.359	2.0433	96.9	-376.7	-3.89	595.9	-2267.6	-3.81	4.50
0.0	0.0	0.0	8.5	115.6	1.19	52.3	696.0	1.17	0.90
1.844	2.375	2.1217	101.3	-421.7	-4.16	599.8	-2354.6	-3.93	8.75
0.0	0.0	0.0	7.9	100.9	1.00	47.0	563.3	0.94	1.75
2.032	2.441	2.4392	51.0	-227.6	-4.46	262.9	961.5	-3.66	4.47
0.0	0.0	0.0	5.1	64.7	1.27	26.4	273.3	1.04	0.89
2.155	2.484	2.6498	40.1	-246.5	-6.14	190.3	-882.2	-4.64	9.16
0.0	0.0	0.0	4.6	61.6	1.53	21.6	220.5	1.16	1.83
2.370	2.558	3.0224	29.0	-274.1	-9.46	120.5	-754.1	-6.26	1.66
0.0	0.0	0.0	5.1	91.3	3.15	21.4	251.2	2.09	0.55

Table 4.4: Extrapolated 180^{o} dcs and Slope for Exponential Fit -- A*exp(B(1 + cos θ_{cm})) or A*exp(BU); B* is the Slope using only 3 Points

Pinc (GeV/c)	E (GeV)	-T (Gevsq)	A (μb/sr)	B		A (μb/GeV^2)	B GeV^{-2}	B* GeV^{-2}	Chi sq. Chi per.
0.703	1.990	0.4394	211.3	11.8	0.0	6044.0	-53.5	-53.5	0.41
0.0	0.0	0.0	48.4	6.7	0.0	1385.7	30.6	30.6	0.41
0.812	2.022	0.5678	90.2	8.4	0.0	1996.2	-29.5	-47.4	1.29
0.0	0.0	0.0	21.1	3.4	0.0	466.3	11.8	34.4	0.32
0.873	2.041	0.6442	68.7	8.0	0.0	1339.3	-24.7	-13.5	1.64
0.0	0.0	0.0	13.6	3.6	0.0	266.2	11.1	26.4	0.55
0.935	2.061	0.7250	44.1	8.0	0.0	765.1	-22.2	-39.6	2.90
0.0	0.0	0.0	16.4	7.4	0.0	284.6	20.4	33.8	0.97
0.987	2.077	0.7948	88.6	-7.8	0.0	1401.5	19.5	26.1	0.18
0.0	0.0	0.0	17.5	5.3	0.0	276.7	13.3	20.6	0.09
1.115	2.120	0.9739	102.8	-0.9	0.0	1326.6	1.8	6.4	0.38
0.0	0.0	0.0	15.8	3.5	0.0	204.0	7.2	11.3	0.19
1.338	2.197	1.3059	154.9	-5.7	0.0	1490.1	8.8	14.8	1.93
0.0	0.0	0.0	18.8	2.2	0.0	181.2	3.4	8.2	0.48
1.447	2.235	1.4755	190.6	-10.1	0.0	1623.6	13.7	15.8	0.47
0.0	0.0	0.0	20.6	2.1	0.0	175.0	2.8	6.0	0.12
1.590	2.286	1.7037	163.8	-9.1	0.0	1208.5	10.7	10.1	2.92
0.0	0.0	0.0	18.1	2.5	0.0	133.4	2.9	5.3	0.97
1.610	2.293	1.7361	162.6	-9.6	0.0	1177.1	11.0	10.0	1.09
0.0	0.0	0.0	18.8	2.7	0.0	135.9	3.2	4.6	0.54
1.716	2.330	1.9093	146.3	-7.6	0.0	962.6	8.0	6.4	1.03
0.0	0.0	0.0	14.7	2.0	0.0	96.8	2.1	3.9	0.34

Table 4.4 (continued)

1.797	2.359	2.0433	97.7	-4.3	0.0	600.7	4.2	6.9	5.18
0.0	0.0	0.0	10.1	1.7	0.0	62.3	1.7	4.7	1.04
1.844	2.375	2.1217	107.5	-5.5	0.0	636.5	5.2	10.7	9.40
0.0	0.0	0.0	10.2	1.5	0.0	60.1	1.4	4.2	1.88
2.032	2.441	2.4392	56.2	-6.8	0.0	289.7	5.6	11.6	4.39
0.0	0.0	0.0	6.6	1.9	0.0	34.2	1.6	4.4	0.88
2.155	2.484	2.6498	49.6	-11.4	0.0	235.3	8.6	12.8	6.48
0.0	0.0	0.0	6.4	2.6	0.0	30.2	1.9	4.3	1.30
2.370	2.558	3.0224	35.1	-18.5	0.0	145.9	12.3	13.2	0.59
0.0	0.0	0.0	7.6	6.2	0.0	31.5	4.1	6.2	0.20

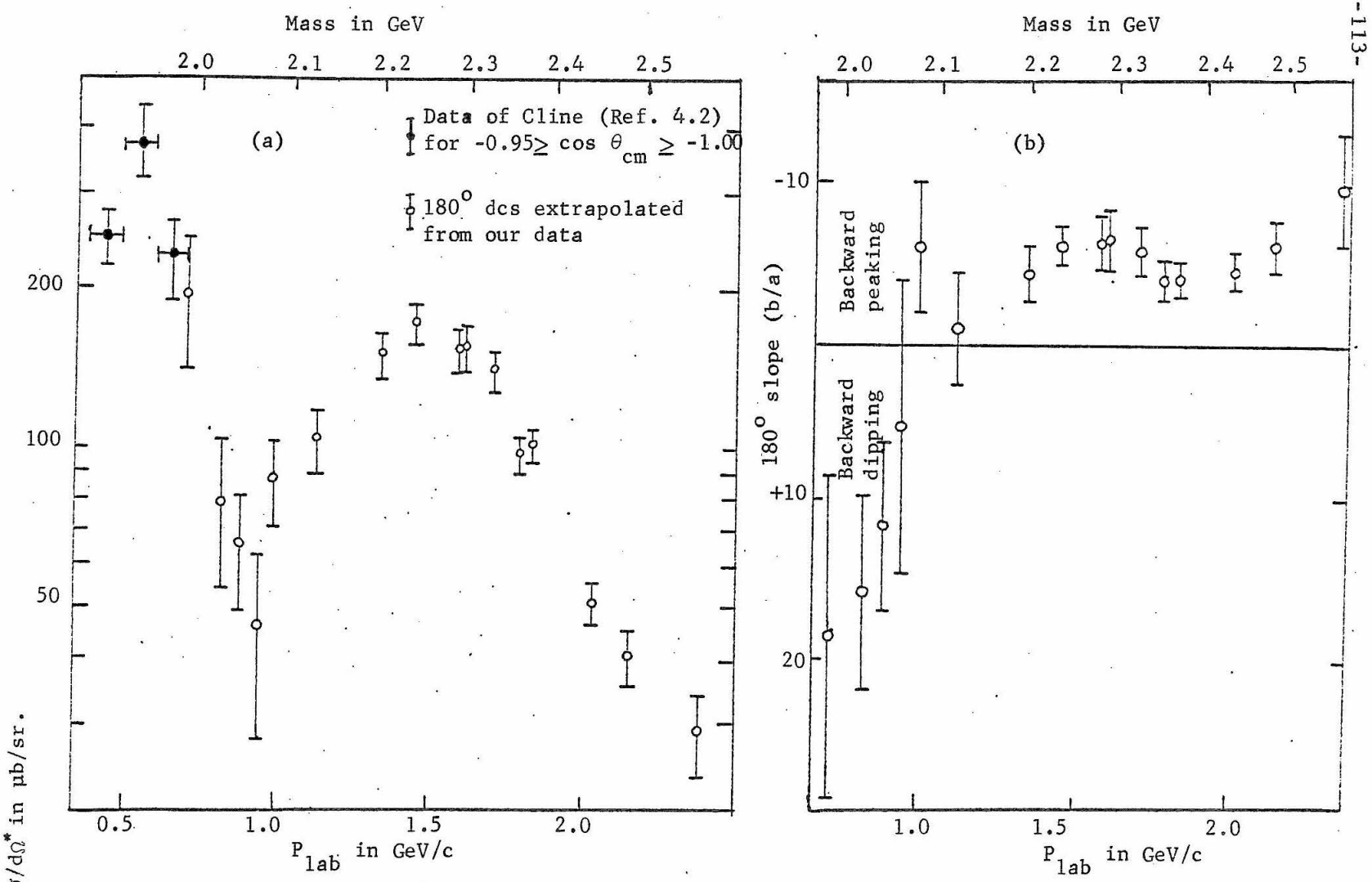

Figure 4.3: Extrapolated 180° dcs and slope (b/a) using linear fit (dcs = a + bx where x is $1 + \cos \theta_{cm}$).

Figure 4.4: Linearly extrapolated 180^{o} dcs (in $\mu b/GeV^{2}$) and slope (in GeV^{-2}) (where dcs = A + B u).

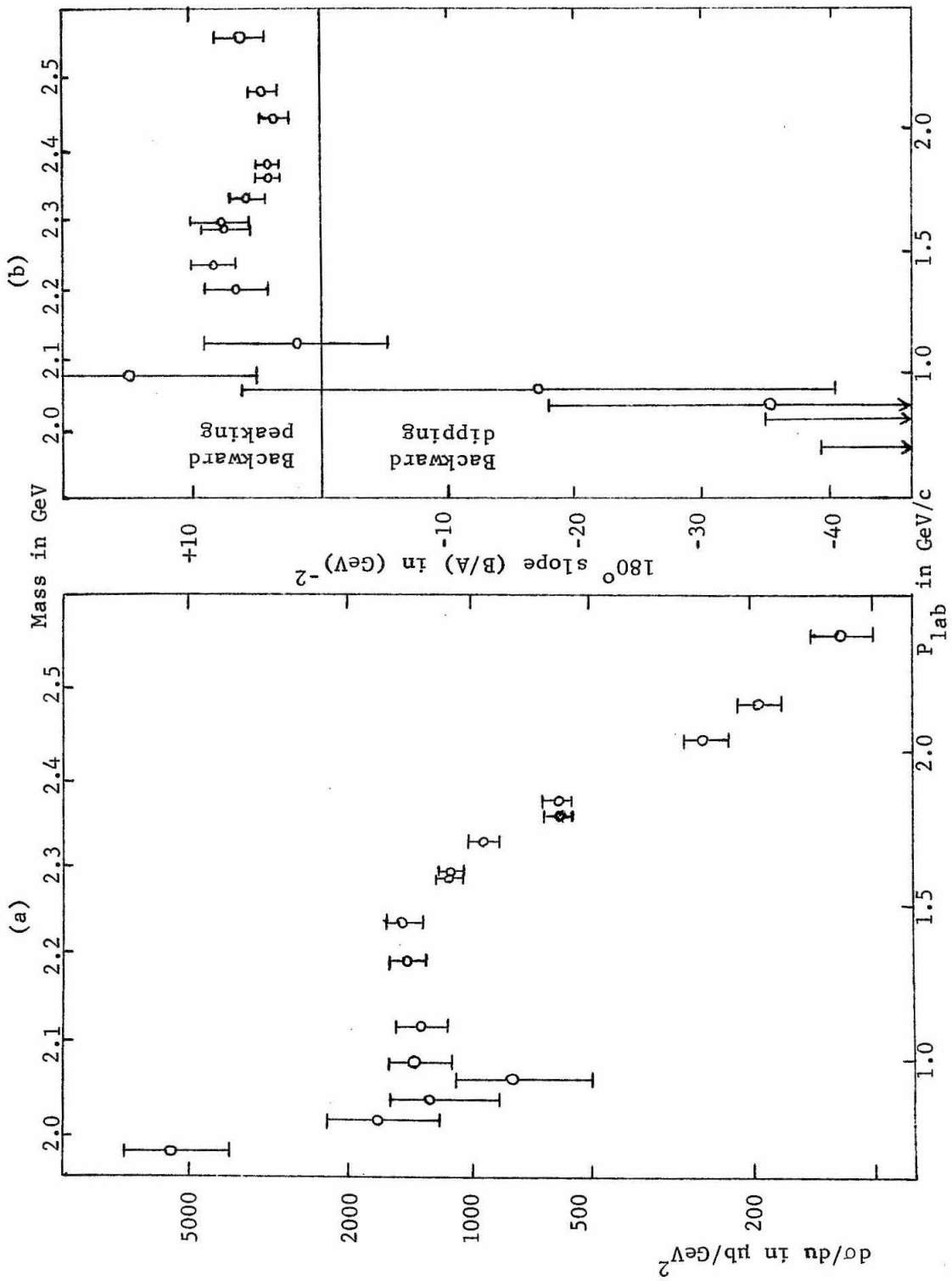

Figure 4.5: Exponential extrapolated 180^{o} dcs (in $\mu b/GeV^{2}$) and slope (in GeV^{-2}) (where dcs = $A\, e^{Bu}$). In (a), the line is a s^{-9} dependence line. In (b), the dashed line is a ln(s) dependence line.

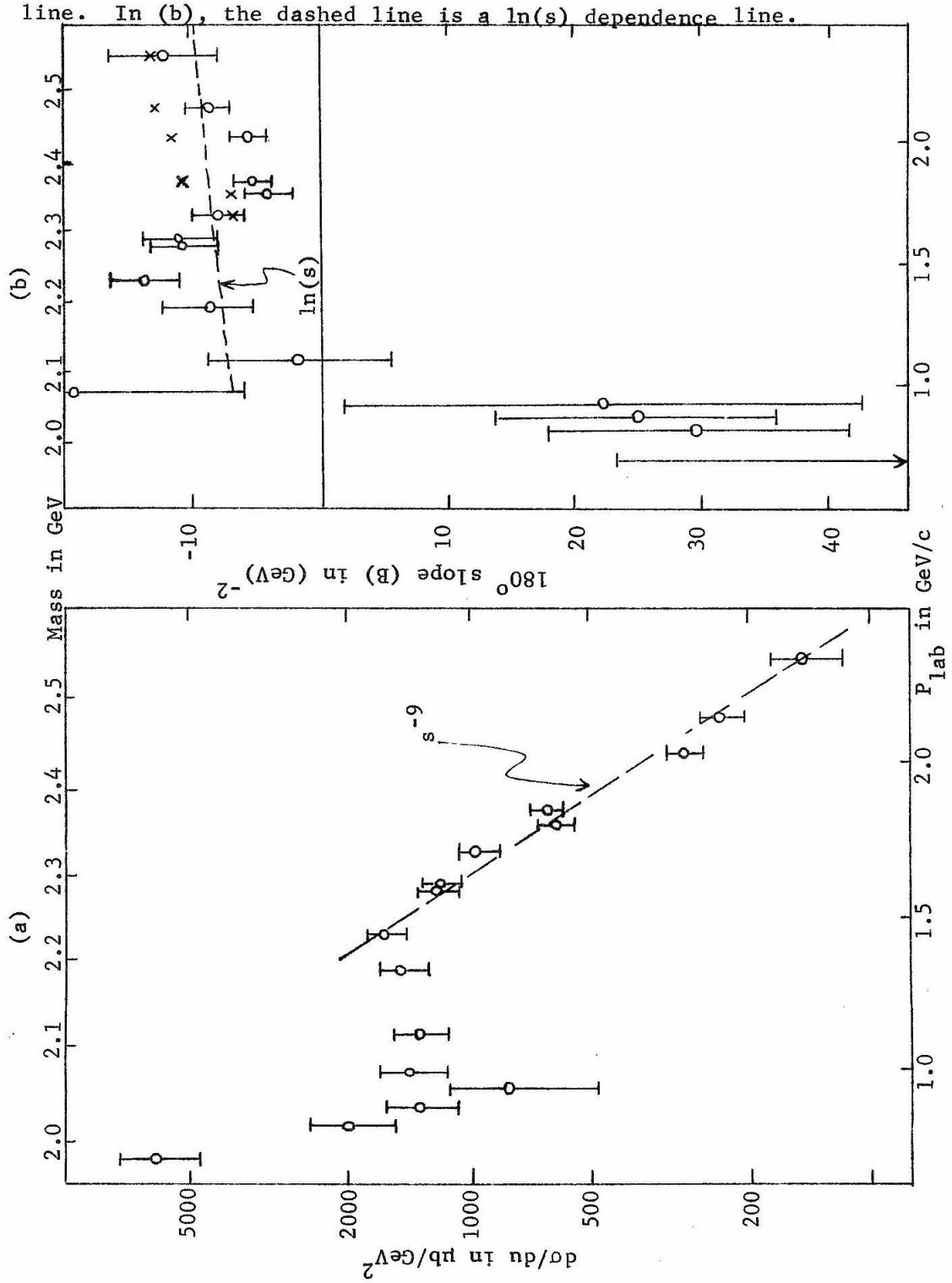

c. Comparison of our Data with Other Existing Data

To check the reliability of our data, we compare our data with other existing data of $\bar{p}p$ elastic backward scattering. These data have been plotted along with our data in Figure 4.1 and 4.3.

Cline et al.[4.2] studied the elastic cross sections in the backward hemisphere from 0.3 to 0.7 GeV/c incident $\bar{p}$ momentum. Their data points in the angular bin closest to 180^{o} (cos θ_{cm} between -0.95 and -1.00) have been included in Figure 4.3. Their data appear to be consistent with ours. The sharp drop of the 180^{o} dcs as momentum increases appears evident in both sets of data.

Cooper et al.[4.3] measured the backward hemisphere $\bar{p}p$ elastic scattering near 1.3 GeV/c. Their data point nearest 180^{o} (covering cos θ_{cm} between -.90 and -1.00 has been included in Figure 4.1. The normalization is in agreement.

Lys et al.[4.4] measured the backward elastic $\bar{p}p$ scattering near 1.8 GeV/c. Their data, included in Figure 4.1 along with our 1.797 GeV/c data, are in agreement with our data.

Additional bubble chamber data on $\bar{p}p$ backward elastic scattering[4.5] is expected to be forthcoming soon.

It should be noted that all of the results mentioned above are bubble chamber results and thus lack statistics. Also, the angular slope of the dcs near 180^{o} cannot be determined with any confidence from these data to check the slope we obtained.

Purely on the basis of these comparisons, it would appear that the reliability of our data is of the order of 10%, which is the approximate size of the errors we quote.

d. Features of our Data

As a function of momentum, we see several structures in the extrapolated 180^{o} dcs.

1. A dip centered near 0.95 GeV/c (2.07 GeV in E) which is about 300 MeV/c (or 100 MeV) wide. The 180^{o} dcs drops sharply from about 300 μb/sr near 0.6 GeV/c (based on the data of Cline[4.2]) to about 50 μb/sr near 0.95 GeV/c. It rises slowly to about 200 μb/sr near 1.45 GeV/c.

2. A broad hump centered at 1.45 GeV/c (2.24 GeV in E). This hump is about 800 MeV/c (or 250 MeV). These two structures could be manifestations of the same mechanism since they are close to each other.

The slope of the dcs at 180^{o} is correlated with the above structures. At momentum below the position of the dip, there are evidences of backward dipping. At momentum above the position of the dip, there are backward peakings up till our highest momentum. The backward peaking above 0.95 GeV/c is confirmed by the data of Cooper[4.3] and Lys[4.4].

There does not appear to be any significant smaller structures in either the 180^{o} dcs or its slope. At each incident momentum, we also look for correlation between the number of backward elastic events and the momentum by finding the number of events whose incident $\bar{p}$ passes through particular mass slit counters[4.6]. No significant dependence is observed.

Our dcs in the angular range $\cos\theta_{cm}$ between -0.88 and -1.0 do not reveal any strong structures aside from backward peaking or dipping.

There are indications at several low momentum points of the backward dipping turning over at larger angles (see Figure 4.1). This evidence is, however, not conclusive. We have also looked for any dips or bumps in our angular dcs which are statistically significant or which occur at particular cos θ_{cm} or at particular values of u for more than one momentum. To do this, we investigate our data with smaller angular binning (cos θ_{cm} bins of 0.01). No such structures aside from backward peaking or dipping are observed.

CHAPTER V: RESONANCES: AN INTERPRETATION OF THE DATA

a. Introduction and the Probable Absence of Strong Regge u Channel Effects

Chapter I has mentioned the possibility of resonance contributions in the direct s channel to backward elastic scattering of $\bar{p}p$. In this chapter, we attempt to study whether the behavior of our data is understandable as being the result of resonance which couples to $\bar{p}p$.

In Section (b-i) we discuss the possible coupling of $\bar{p}p$ to any boson resonances. Section (b-ii) describes the characteristics of elastic scattering of $\bar{p}p$ in the presence of a resonance in the direct s channel. We list in Section (c-i) the resonance candidates which have been suggested by other data. In Section (c-ii), we describe several theoretical models which predict the number and position of various resonances which couple to $\bar{p}p$.

We attempt to correlate our data to the resonance situation in Sections (d-i) (covering narrow -- less than 50 MeV-- resonances) and (d-ii) (covering broad resonances). We conclude this chapter with Section (e), which summarizes the resonance situation.

Before we proceed in a resonance interpretation of our data, we would like to make a few comments on the possibility of our data being dominated by a single Regge trajectory in the exchange u channel. In that case, $d\sigma/du$, as mentioned in Chapter I, should (a) have a $\exp(2*\ln(s)*b*u)$ dependence at each momentum, and (b) have 180^{o} $d\sigma/du$ be $s^{2\alpha(0)-2}$ as a function of momentum. Figure 4.5 shows the ex-

ponentially extrapolated 180^{o} $d\sigma/du$ and slope. Below 1.4 GeV/c, no evidence for Regge dominance is seen. Above 1.4 GeV/c, the 180^{o} $d\sigma/du$ appears to follow s^{-9} fairly closely. This could indicate that the backward scattering is dominated by a trajectory with $\alpha(0)$ approximately -3.5 [5.1]. However, the slope of the fit, shown in Figure 4.5, does not seem to follow the ln(s) dependence which is indicative of single Regge u channel dominance.

The normal exponential fit uses almost all our angular data covering a u region of up to 0.2 GeV^2. It is possible that u channel effects are dominant only for u less than 0.2 GeV^2. Thus,we investigate an alternative exponential fit using only 3 smallest angle data points at each momentum. This covers a region of u less than 0.07 GeV^2. The extrapolated 180^{o} $d\sigma/du$ is within the error bars of the extrapolated values for the normal exponential fit. However, the extrapolated slopes above 1.7 GeV/c become much larger. We show the alternative slopes as x's in Figure 4.5. The slopes above 1.4 GeV/c are now consistent with an ln(s) momentum dependence (shown as a line in Figure 4.5). The slopes are typically 10 $(GeV)^{-2}$ possibly indicating that the b of the dominating trajectory is about 3 $(GeV)^{-2}$ [5.1] (the trajectory is $\alpha(0) + b\,u$).

Thus, we conclude that our data are consistent with a strong u channel contribution from a single Regge trajectory only in the region of u less than 0.07 GeV^2 above incident momentum of 1.4 GeV/c. Even in that region, our data are inconclusive. Other interpretations, such as those discussed in this chapter, can explain the features in

our data suggesting Regge behavior. Since there are good theoretical reasons to believe Regge behavior to be weak (B = Q = 2 particles are not expected), we can probably ascribe all the features observed in our data to resonance effects.

b. Resonances and the $\bar{p}p$ System: Theoretical Considerations

(b-i) The Coupling of Resonances to the $\bar{p}p$ System

Given the existence of a boson resonance X with definite quantum numbers (mass M, spin J, parity P, charge conjugation C, isospin I, etc.), several statements can be made about its coupling to the $\bar{p}p$ system. In particular, the coupling is constrained by 1) threshold constraints, 2) isospin constraints, 3) spin-parity-charge conjugation constraints, and possible 4) angular momentum barrier constraints:

1) Threshold constraints. X can couple to the $\bar{p}p$ physical system only if its mass is greater than $2 M_p$. However, if the mass is slightly below threshold, the tail of the resonance could influence the $\bar{p}p$ behavior above threshold.

2) Isospin constraints. Since both $\bar{p}$ and p have isospin 1/2, the $\bar{p}p$ system can couple to X only if X has isospin 0 or 1.

3) Spin-Parity-Charge conjugation constraints. For a boson resonance X with spin J, the parity and charge conjugation of X is restricted if X is to couple to $\bar{p}p$. Following the usual convention, we shall define the parity P (or charge conjugation C) to be normal if P(C) is $(-1)^J$ and abnormal if P(C) is $(-1)^{J+1}$.

Both $\bar{p}$ and p are spin 1/2 fermions. For a fermion-antifermion

system, $P = (-1)^{L+1}$ and $C = (-1)^{L+S}$ where L is the relative angular momentum and S is the total spin[5.2]. Thus, the $\bar{p}p$ system can only couple to the following three of the four possible combinations of P and C:

1. Singlet-(S)- S = 0 implying J = L, P abnormal and C normal.
2. Normal Triplet -(NT)- S = 1 and J = L ± 1 implying both P and C are normal.
3. Abnormal Triplet -(AT)- S = 1 and J = L implying both P and C are abnormal.

Thus, if X has normal P and abnormal C, it cannot couple to $\bar{p}p$. It should be noted that the simple quark model (which we will cover in Section (c-ii)) prohibits the existence of bosons with such a combination of P and C assuming all bosons to be made out of quark-antiquark pairs. This is true since quarks are fermions.

4) Angular momentum barrier constraints. The coupling of X to the $\bar{p}p$ system may be suppressed totally or strongly by the angular momentum barrier[5.3].

One would expect that the $\bar{p}p$ interaction would be characterized by a distance corresponding to the proton radius. This is what one expects if optical type interaction is dominant. The interaction distance for $\bar{p}p$ can be obtained by considering the forward diffraction peak. One finds an interaction distance of about 1.0 Fermi. Then, the maximum angular momentum state that the $\bar{p}p$ system could couple to strongly would be kr + 1 (k is the cm momentum, r is the interaction distance). However, at all momenta this number is below the J of the leading trajectory (see

Figure 5.1a, a plot of the leading boson trajectory and the curve kr + 1 against s). Thus, if the recurrences on the leading trajectories do exist, their coupling to $\bar{p}p$ could be reduced by the angular momentum barrier. This possibility is not in conflict with the observed strong coupling of pi-N system with the nucleon resonances (see Figure 5.1b).

As far as the strength of the coupling of boson resonances to $\bar{p}p$ is concerned, we would expect K_{el}(elasticity) to be of the order of 0.1 or less. A massive boson resonance can decay into many channels and thus is not expected to couple to $\bar{p}p$ very strongly.

Another item which affects the search of boson resonances in the $\bar{p}p$ system is the possibility that there are many resonances at nearly the same energy. The effects of any single resonance may thus be obscured. For example, in the theory of the daughter trajectories, the number of resonances at the same region of energy would be of the order of 10 (see Section (c-ii)).

(b-ii) Features of Resonance Contribution to Elastic $\bar{p}p$ Scattering

We now investigate the behavior of the elastic amplitude, elastic total cross section and the total cross section caused by the presence in the direct s channel of a resonance with spin J, parity P, charge conjugation C, elasticity K_{el} and mass M (corresponding to cm momentum k for the $\bar{p}p$ system)[5.4]. Except for the last few paragraphs of this section, we shall only concern ourselves with the pure resonance contribution and ignore any interference effects.

Recall that the $\bar{p}p$ system, for a particular J, occurs in three

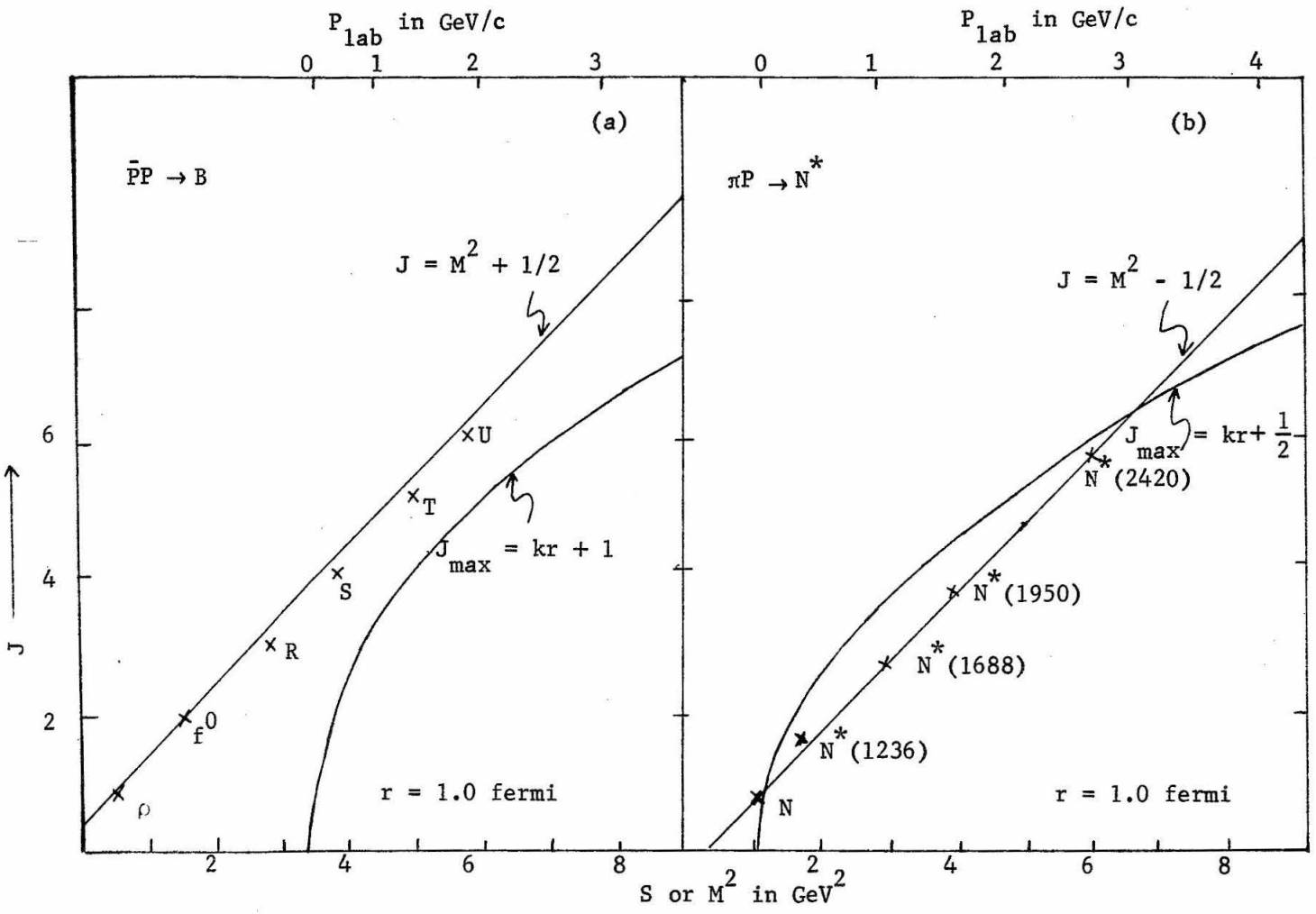

Figure 5.1: Angular momentum barrier for the (a) $\bar{p}p$ and (b) πN systems

combinations of P and C -- the Singlet, Normal Triplet and Abnormal Triplet (see the previous section). Since elastic scattering of $\bar{p}p$ is a strong interaction, P and C are conserved and no transition between these states is possible. Thus, each state must be treated separately.

We shall first obtain the values of the total elastic cross section S_{el} and the total cross section S_{tot} for a definite isospin-parity-charge conjugation state. In this case, we obtain, at incident momentum corresponding to the peak of the resonance,

$$S_{el}^{I,s} = (4\pi/k^2)\ \frac{1}{2}\ (J + \tfrac{1}{2})\ (K_{el})^2 \qquad (5.1a)$$

$$S_{tot}^{I,s} = (4\pi/k^2)\ \frac{1}{2}\ (J + \tfrac{1}{2})\ K_{el} \qquad (5.1b)$$

The $\bar{p}p$ state is equally in I = 0 and I = 1 states. Hence, isospin gives an additional factor of 1/2 in S_{tot} and 1/4 in S_{el} ($\sqrt{1/2}$ from each vertex). Also, the $\bar{p}p$ initial state is 1/4 Singlet, 1/4 AT (abnormal triplet) and 1/2 NT (normal tripler)[5.5] for unpolarized incident beam and target. Thus,

$$S_{el}(\bar{p}p;\ S\text{--singlet}) = S_{el}(\bar{p}p;AT) = (1/16)S_{el}^{I,s} \qquad (5.2a)$$

$$S_{el}(\bar{p}p;NT) = (1/8)S_{el}^{I,s} \qquad (5.2b)$$

$$S_{tot}(\bar{p}p;S) = S_{tot}(\bar{P}p;AT) = 1/2\ S_{tot}(\bar{p}p;NT) = (1/8)S_{tot}^{I,s} \qquad (5.2c)$$

where $S_{tot}(\bar{p}p;S)$ is the S_{tot} for a singlet resonance.

Having determined the size of the total elastic cross section due to pure resonance contribution, we now study the angular shape of the dcs or the elastic amplitude. The normalization of the dcs can

be obtained by integrating the dcs and comparing it to the total elastic cross section.

For each spin state s, m_s, and m_s' (s is the combined spin, m_s the initial z component and m_s' the final z component of the spin), there is an elastic amplitude(5.6)

$$A_{s,m_s,m_s'}(\theta,\varphi) = \sum_{L,L'} i^{L-L'} \pi^{1/2} (2L+1)^{1/2} \frac{1}{2}\left((d_{fi} - S_{fi}^{I=0}) + (d_{fi} - S_{fi}^{I=1})\right)(Ls0m_s|LsJm_s)(L'sm'm_s'|L'sJm_s)\, Y_{L'}^{m'}(\theta,\varphi) \tag{5.3}$$

where d_{fi} is a delta function of the final and initial states, S_{fi}^{I} is the S matrix of the final and initial state for isospin I.

For each of the three permissible spin-parity-charge conjugation states, the shape of the dcs is proportional to the sum of the spin amplitudes absolute squared. It is different for each of the three cases.

Case (1) - Singlet -- s = 0, L = L' = J and therefore $m_s = m_s' = 0$.

In this case, there is only one spin amplitude -- the one with $s = m_s = m_s' = 0$ and it has only one non-zero term with L = L' = J. The amplitude is proportional to Y_J^0 only. The shape of the dcs is

$$F_s(\theta) = |Y_J^0(\theta)|^2 \tag{5.4}$$

and is equivalent to the spinless case. We show this shape for several J's in Figure 5.2.

Case (2) - AT (Abnormal Triplet) -- s = 1, L = L' = J.

In this case, there are 9 spin amplitudes -- m_s and m_s' can be either -1, 0 or 1. Each spin amplitude has only one term where

Figure 5.2: Shape of the dcs for pure J-P-C states. For the normal triplet states, there is a free parameter $G = G_{L=J+1}/G_{L=J-1}$.

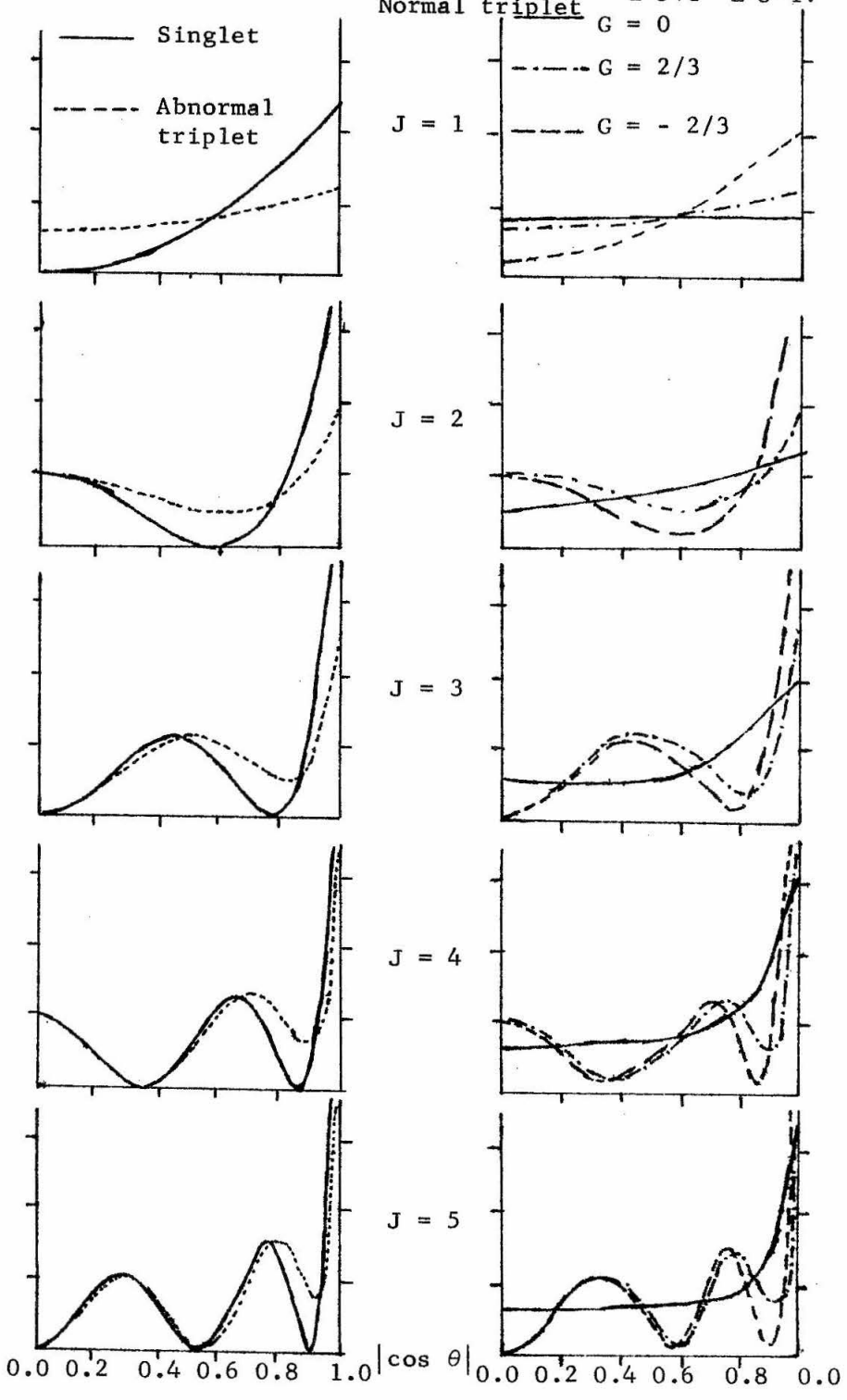

$L = L' = J$. Actually, $(J100|J1J0)$ is zero. Therefore, the amplitudes with $m_s = 0$ do not contribute and only 6 amplitudes are non-zero. The shape of the dcs is

$$F_{AT'}(\theta) = \sum_{m_s, m_s'} |(J10m_s|J1Jm_s)(J1m'm_s'|J1Jm_s)\ Y_J^{m'}(\theta,\varphi)|^2 \qquad (5.5)$$

which simplifies to a sum proportional to

$$F_{AT}(\theta) = 2(J+1)J|Y_J^0|^2 + 4|Y_J^1|^2 + 2(J-1)(J+2)|Y_J^2|^2 \qquad (5.6)$$

Of course, this is valid only for J larger than 1. In these cases, for the same value of J and K_{el}, the coefficient of the $|Y_J^0|^2$ term is exactly 1/2 of the corresponding term for the singlet case. The shape of this function, shown in Figure 5.2 for several values of J, is similar to a pure $|Y_J^0|^2$ shape (at 0^o or 180^o, the AT is 1/2 of the S).

Case (3) - <u>NT (Normal Triplet)</u> -- $s = 1$, $L = J \pm 1$, $L' = J \pm 1$.

In this case, each spin amplitude has 4 terms for the 4 combinations of L and L' and there are 9 spin amplitudes. The dcs is proportional to

$$F_{NT}(\theta) = \sum_{m_s, m_s'} \Big| \sum_{L, L'=J\pm1} (L10m_s|L1Jm_s)(L'1m'm_s'|L'1Jm_s)\ Y_{L'}^{m'}(\theta,\varphi)\, i^{L-L'} (2L+1)^{1/2}\ G_L G_{L'} \Big|^2 \qquad (5.7)$$

where G_L and $G_{L'}$ are the relative coupling of the resonance to the L and L' states. They are not necessarily the same for $L = J + 1$ and $J - 1$ due to, for example, angular momentum barrier which may

favor the L = J - 1 state.

Thus, we get 9 terms containing $Y_{J\pm1}^{m'}$ for m' = 0, ± 1 or ± 2. The shape of the dcs is dependent on the free parameter $G \equiv G_{L=J+1}/G_{L=J-1}$. We show $F_{NT}(\theta)$ for several values of J and G in Figure 5.2. For values of G near ±1, the shape of F_{NT} approximates the shape of F_S. For G near 0, the Y_L^1 and Y_L^2 terms dominate and F_{NT} deviates significiantly from F_S. The dcs at 0^o and 180^o, for the same normalization of S_{el}, ranges between 1/4 and 1 of the F_S value. Since the $\bar{p}p$ system has twice as much probability of being in the NT state, the dcs at 0^o or 180^o for the NT case, for the same value of J and K_{el} of the resonance, would be between 1/2 to twice the corresponding value for the S case.

In the presence of background or other resonances, there may be interference terms as well as pure resonance and background terms. The behavior would then be more difficult to decipher. However, if there is a particular resonance which couples strongly to $\bar{p}p$ and which has a high J, the dcs should show peaking at extreme angles. The peaking at backward angles should disappear as we move away from the resonance mass. We can search for this type of behavior.

The spin of the possible resonance can be suggested by the slope of the backward elastic cross section near 180^o. However, there are several difficulties. For a definite assumption of J, the slope will depend on the spin-parity-charge conjugation of the resonance. Interference and background terms may also obscure the spin determination. Nevertheless, if we assume any backward peaking to be caused by dominance of a single resonance, we can establish a

minimum value of its spin. The sharpest possible peaking is produced by a pure Y_J^0 amplitude.

For any suggested resonances whose spin and elasticity (or the product $K_{el}(J + 1/2)$) are known, we can see if our 180^o data are consistent with their existence. To do this, we use the analogue of the optical theorem to relate the 180^o resonance amplitude with $K_{el}(J + 1/2)$ (which is proportional to the total cross section). There are, however, may degrees of freedom in this calculation since the result depends on whether the resonances are in singlet, abnormal triplet or normal triplet states.

c. Other Experimental and Theoretical Evidences for Boson Resonances

(c-i) Other Experimental Evidence

We shall now discuss the experimental status (excluding our data) of the resonances which have quantum numbers capable of being coupled to $\bar{p}p$. Table 5 lists the boson resonances candidates found in three experiments. These experiments found statistically significant bumps which can be interpreted as resonances and they are also capable of giving the width of each bump. We shall label these experiments by A, B, and C. Other experiments with poorer statistics also see structures interpretable as resonance effects.

A) CERN missing mass spectrometer experiments[5.7]. This is the first series of experiments which covered the boson mass region 0.5 to 2.5 GeV for I larger than 0. For incident π^- beam, the recoil proton at fairly small t (-0.1 to -0.4 GeV^2) is detected and momentum analyzed. They discovered 4 statistically signi-

Table 5.1: Boson resonance candidates above twice the proton mass. A similar table appears in the wallet sheets and data booklet by the "Particle Data Group" including all boson resonance candidates above 1.7 GeV. Those candidates marked with an * could be kinematic enhancements[5.10].

Mass (MeV)	Width (MeV)	I	Experiment	Comments
1929 ± 14	35	1	A	The "S" meson
2086 ± 38*	150	1	B	
2190 ± 10	85	1	C	Enhancement in $\sigma_T^{I=1}$ is 6 mb. possibly due to N* threshold (one pion production rises in this region from 0 to about 5 mb - see Cooper[5.14]. $\bar{p}p$ to $\bar{n}n$ data of Bricman[5.18] sees weaker structure.
2195 ± 15	13	1	A	The "T" meson. Possibly seen by Kalbfleisch[5.15].
2260 ± 18*	25	1	B	
2345 ± 10	140	0	C	Enhancement in $\sigma_T^{I=0}$ is 3 mb.
2370 ± 17*	57	1	B	
2382 ± 24	30	1	A	The "U" meson. Possibly seen by Michigan and Michigan St.[5.16].
2380 ± 10	140	1	C	Enhancement in $\sigma_T^{I=1}$ is 2 mb. Evidence for this is also seen in $\bar{p}p$ to $\bar{n}n$[5.18]. Could be caused by N*(1400) threshold.
2500 ± 32*	87	1	B	
2620 ± 20	85	1	A	
2800 ± 20	46	1	A	
2880 ± 20	15	1	A	

ficant bumps with mass above the split A_2 which they labeled R (a triplet), S, T, and U. The last three have masses greater than 2 M_p. In a continuation, they covered the region above 2.5 GeV[5.7].

B) BNL $\bar{p}p$ and $\bar{p}d$ total cross-section measurements[5.8]. They covered the mass region 2.05 to 2.7 GeV and found bumps which can be resolved into 2 I = 1 and 1 I = 0 bumps. They were able to give the enhancements to the total cross section for these bumps as well as the mass and widths. However, the positions of these bumps occur near N* thresholds (see 3) in the next page). They cannot resolve any narrow resonance with widths of the order of 5 MeV.

C) BNL-Carnegie-Mellon missing mass spectrometer[5.9]. They measured the same process as the CERN experiment except that they detect the recoil proton at small u. They found four statistically significant bumps above twice the proton mass. However, there is a strong possibility that these bumps are caused by kinematic enhancements[5.10]. If these bumps are indeed caused by resonances, then the two spectrometers disagree quite significantly (see Table 5.1).

Other experiments measuring the $\bar{p}p$ system include:

1. Two sets of data studying processes with $\bar{p}p$ in the final state in addition to other final state particles[5.11,5.12]. These bubble chamber data suffer from poor statistics and definite conclusions cannot be drawn. However, the data of Diamond[5.12] does suggest a possible enhancement in the combined mass of $\bar{p}p$ near the T meson

region (2190 MeV).

2. In the S meson region (1924 MeV), Cline[5.13], in a bubble chamber experiment, studied the $\bar{p}p$ backward hemisphere elastic scattering and claimed to see two structures. The statistics are poor.

3. In the T meson region (2190 MeV), Cooper[5.14] found that a sizable portion of the bump in the total cross section can be accounted for by the one pion inelastic channel (indicative of N^* threshold production). They failed to see any sharp structures in the topological cross sections. However, the possibility of a broad resonance in the T meson region is not ruled out. Kalbfleisch [5.15] reported a narrow enhancement in the $\rho\rho\pi$ channel near the T meson supporting the possibility of a narrow resonance there.

4. Michigan and Michigan St.[5.16] both studied the U meson region in bubble chamber exposures and reported enhancements in the $KK3\pi$ channel there (narrow and supposedly highly inelastic). In addition, Lys in Michigan[5.17] claimed to see an onset of backward peaking in $\bar{p}p$ elastic scattering near 1.8 GeV/c (2380 MeV). Poor statistics, however, weaken their claim.

5. A group at CERN measured the process $\bar{p}p \rightarrow \bar{n}n$ covering 2.05 to 2.7 GeV, including the T and U regions[5.18]. They again see structures in both T and U regions. The structure in the T meson region appears to disagree with the total cross-section enhancement if both are assumed to come from the same resonance with a reasonable assumption of J. The structure in the U region is consistent with a resonance producing the enhancement observed in the total cross section. This

provides additional evidence that the bump in the total cross section in the T region is probably due mostly to N* threshold.

6. Folded angular cross sections of $\bar{p}p$ into charged pi or charged kaon pairs have been obtained by combining two experiments[5.19,5.20] which covered the region 2.0 to 2.55 GeV. There is evidence in the charged pion data of strong J = 3 and J = 5 partial waves suggesting possible resonances in these spin waves. The behavior of these cross sections near the U meson region (2380 MeV) is verified by the Michigan bubble chamber exposure[5.21]. It is interesting to note that Goldhaber[5.22] using a quark-antiquark model (discussed in the next section) predicted the existence of a J = 3 and a J = 5 resonance near 2.2 GeV which should couple to both $\bar{p}p$ and charged pion pairs. The two possible resonances suggested by the charged pion data occur near the T meson region (for the J = 3) and the U meson region (for the J = 5) and their widths are quite broad[5.20]. However, these values are obtained from a fitting program and the solution may not be unique.

In conclusion, although there is some evidence for resonances in the $\bar{p}p$ system, none have been well established.

(c-ii) Theoretical Models Predicting Boson Resonances

The CERN missing mass data showing the possible existence of heavy mesons has lead to a number of theoretical models attempting to predict the exact number, position (in the mass^2 vs. J plot) and characteristics of heavy boson resonances. We shall briefly describe two such models, the quark-antiquark model[5.22] and the daughter

trajectory model.[5.23]

$q\bar{q}$ (quark-antiquark) model

According to the quark model of Gell-Mann and Zweig[5.24], some of the bosons established experimentally can be classified into being members of octets and singlets with the same J, P, and C. Thus, three octets and singlets with $J^{PC} = 0^{-+}$, 1^{--} and 2^{++} have been well established[5.25]. In this model, the 0^{-+} and 1^{--} mesons are assumed to be the two S wave combinations of $q\bar{q}$ (each having spin 1/2). Further combinations can be made if we accept the formation of $qq\bar{q}\bar{q}$, if we allow higher L states, or if we accept radial excitations. For example, the 2^{++} can be viewed as the P wave triplet J = L + 1 combination of $q\bar{q}$. We have chosen to discuss the simple quark model[5.22] where mesons are formed by $q\bar{q}$ only and only spin excitations are allowed (i.e., no radial excitation is allowed).

In this model, mesons must occur only in octets and singlets with strangeness and I both less than or equal to 1. In addition, just like the $\bar{p}p$ system, states with normal P and abnormal C are not allowed (see page 121). Thus, for each L larger than 0, there should be 4 multiplets (3 triplet and 1 singlet). For example, the states with L = 1 are 0^{++}, 1^{++}, 1^{+-} and 2^{++}.

States with different L are expected to have different mass^2's. In addition, the four multiplets for each L are expected to be further split by either spin-orbit terms or tensor terms. However, if we assume that the rotational excitation splitting is more than the spin-orbit or tensor splitting, then we expect the multiplets for each L will cluster around certain mass^2 values. In practice, this

assumption appears to be correct. A comparison of the mass^2 of several mesons tentatively classified as L = 1 states suggests that they cluster around mass^2 of about 1 GeV^2. Also, spin-orbit splitting appears to dominate over tensor splitting[5.26]. Thus, we expect to see clusters of resonances. If spin-orbit splitting does dominate over tensor splitting, the mass^2 splitting due to the spin-orbit interaction is definite -- (-2L-2), -2, 2L and 0 for the triplet J = L - 1, J = L, J = L + 1 and singlet states, respectively.

Experimentally, no "exotic" mesons (i.e., mesons which cannot be made out of $q\bar{q}$) have been confirmed. In addition, all predicted mesons for L = 0 and many predicted mesons for L = 1 have been found. The high mass boson candidates found in the CERN missing mass experiment[5.7] fall on the ρ, A_2 trajectory and thus may be identified as higher J states associated with the $q\bar{q}$ model. Also, the 3^{--} and 5^{--} states found in $\bar{p}p \rightarrow \pi^+\pi^-$ [5.20] are predicted by this model and occur at approximately correct values of mass^2 [5.27].

In Figure 5.3 we present a graph of all the predicted $q\bar{q}$ states with mass^2 vs. J and mass^2 vs. L. The position of the known states are put where the mass^2 actually exists.

In conclusion, we should mention that there might be radial excitations which may create high mass states with low spins. Thus, the existence of such states will not force us to abandon the $q\bar{q}$ model. The prediction of the absence of "exotic" mesons is an integral part of the $q\bar{q}$ model and there are many recent attempts to find such mesons.

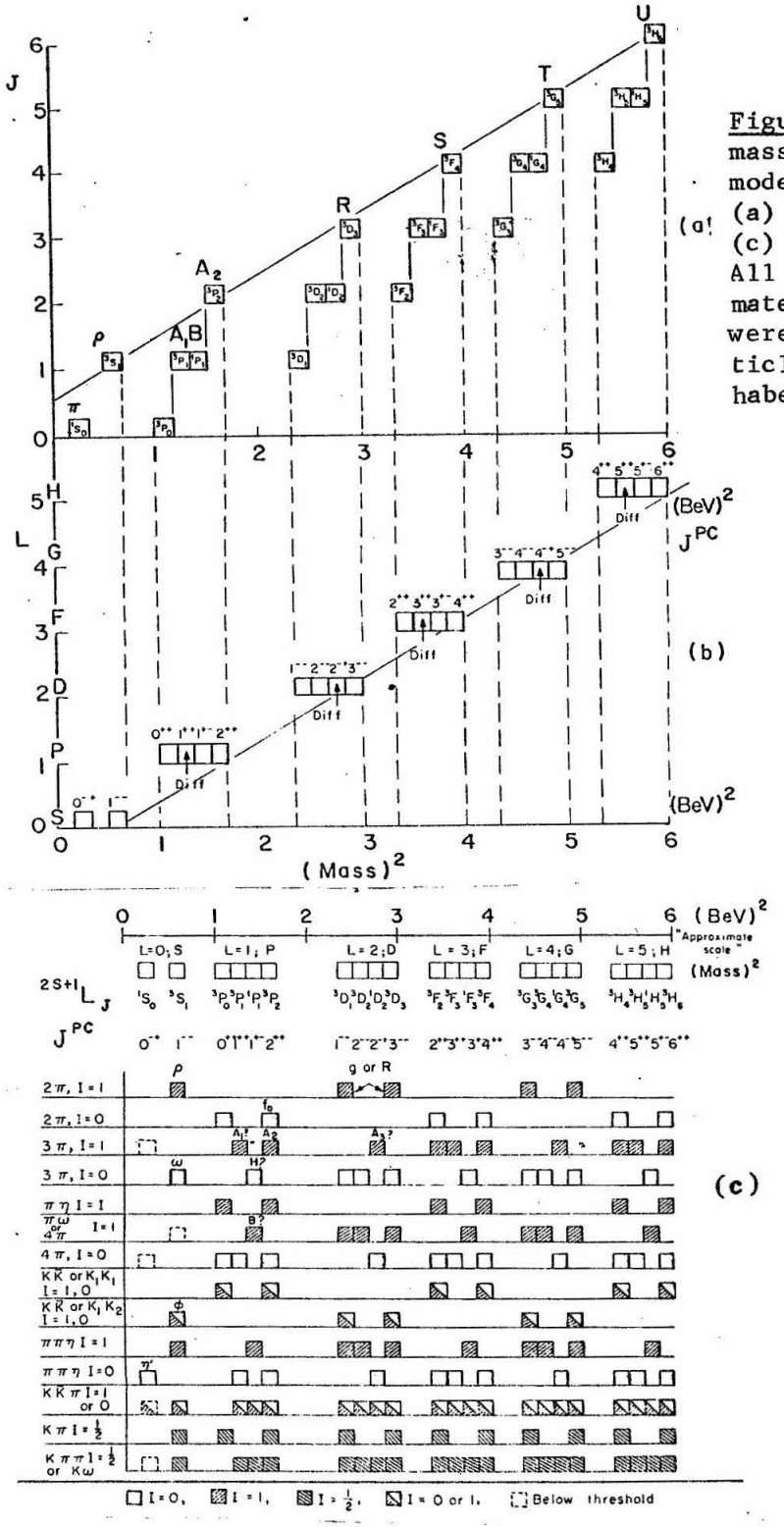

Figure 5.3: Expected $q\bar{q}$ mass states of the $q\bar{q}$ model plotted against (a) J, and (b) L, and (c) allowed decay modes. All masses are approximate. These figures were taken from an article by G. & S. Goldhaber (Ref. 5.22).

Daughter trajectory model

In many models of high energy physics, the existence of a single trajectory is unacceptable[5.23]. At t = 0, there must be compensating terms with $J = J_0 - 1$, $J = J_0 - 2$, etc., where J_0 is the trajectory at t = 0. These terms could arise from "daughter trajectories" which sit below the established leading trajectories and are usually expected to be parallel to the leading trajectories. If this picture is correct, at the position of mass^2 of a member of the leading trajectory with spin J, are are J daughters with spin J - 1, J - 2, ...0. Thus, we may expect the existence of at least the mesons states depicted in Figure 5.4. Established non-strange mesons have been placed on the appropriate spots in Figure 5.4. As can be observed, the number of different states is at least 10 above the $\bar{p}p$ threshold at each "cluster". The masses of the states at each cluster are expected to be the same if the assumption of daughters being parallel to the leading trajectory is correct. Hence, our hope of deciphering the individual resonance appears to be rather difficult if this is indeed the case. The $q\bar{q}$ model could also allow "daughter"-like trajectories if radial excitations are allowed[5.28].

Thus, both models predict many resonances which cluster together. The $q\bar{q}$ model predicts 12 states at each L (1 I = 0 and 1 I = 1 state for each octet plus 1 singlet state) while the daughter trajectory model predicts 10 or more states at each cluster above the $\bar{p}p$ threshold. Hence, if either one of these models is correct, we can see the individual resonances only if there is a dominant resonance or if a particular resonance is very narrow. Phase shift analysis can

Figure 5.4: States expected in the daughter trajectory model where circles are states possibly seen and x's are expected states. For each x or circle, there is a I = 0 and a I = 1 state (e.g., the A_2 and f^0). Thus, in the region of S, 10 states are expected.

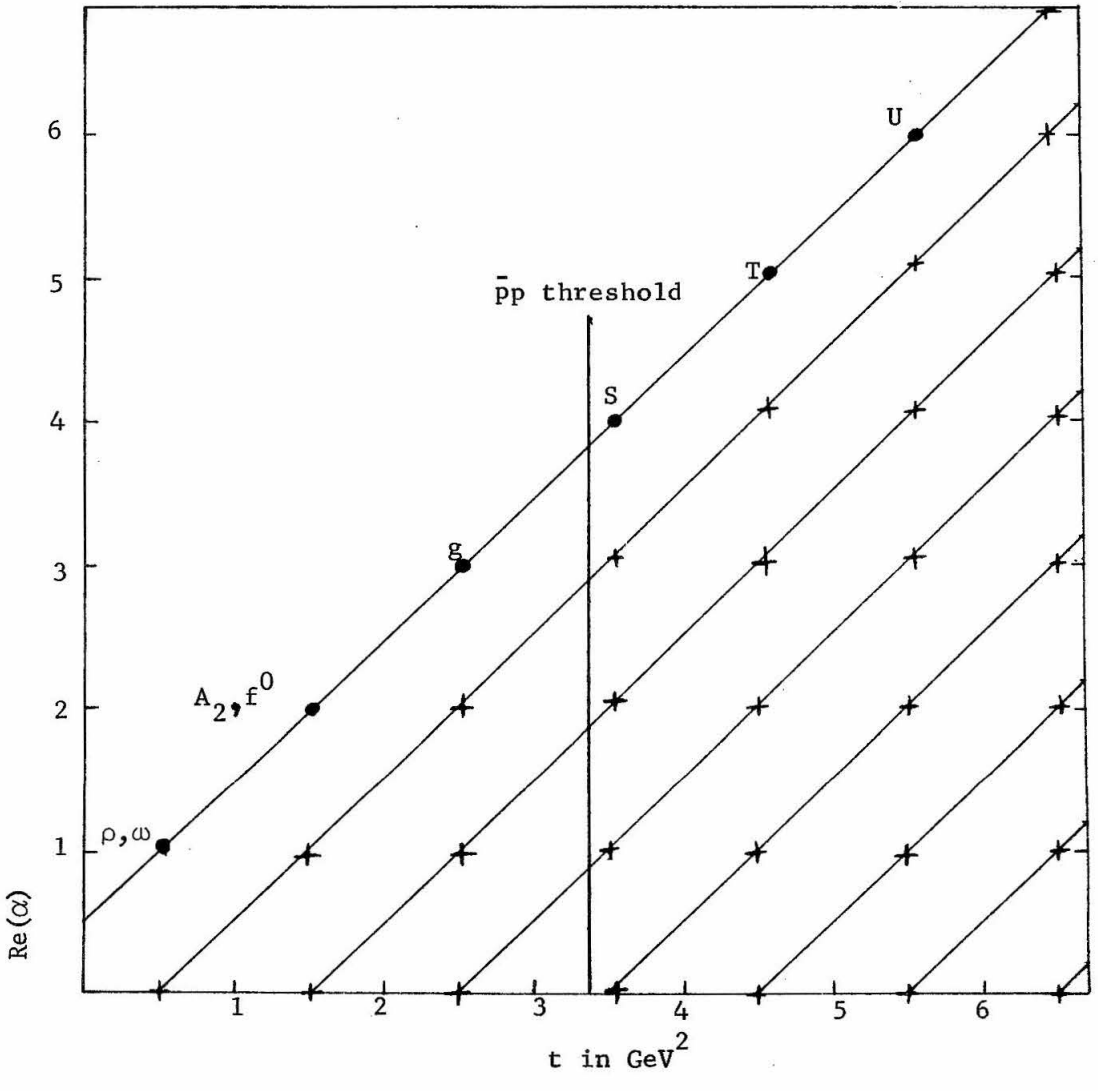

eventually be done to decipher the individual states. Polarization measurements are needed to do this, however.

d. What our Data Say about Resonances in the Direct Channel

(d-i) Narrow Resonances

In the direct channel, we cover the mass range 1.99-2.48 GeV. Thus, we are sensitive to bosons in this range of energy. How can we see resonances? If the 180^{o} dcs as a function of momentum shows a structure of Breit-Wigner shape accompanying backward peaking, this would be a clear indication of the existence of a direct channel resonance. Otherwise, any sharp structure in either the 180^{o} dcs or slope may indicate resonances. The possible absence of the characteristic Breit-Wigner shape in the dcs and the backward peaking may be attributed to interferences. In a region where no sharp structure is observed, we may set an approximate upper limit on the value of $1/2(J + 1/2)K_{el}$ of any possible resonance in that region.

We shall first study the possible existence of narrow (widths less than about 50 MeV) resonances. Many resonance candidates listed in Table 5.1 have such narrow widths.

Our 180^{o} dcs and slope (see Figure 4.3) show no narrow structures. Our points at 2.197 GeV (near the T meson) and at 2.375 GeV (near the U meson) do not show significantly larger 180^{o} dcs or sharper backward peaking compared to adjacent points. The only sharp structure in the 180^{o} dcs is a 100 MeV wide dip near 2.06 GeV. All our 180^{o} dcs can be fitted on a smooth curve to within one standard deviation. Although our 180^{o} slope shows backward peaking above

2.07 GeV, the slope does not appear to be much sharper at any particular energy. Thus, no evidence for narrow resonances which couple strongly to $\bar{p}p$ is seen.

Furthermore, at each momentum we can divide our data into bins in which the incident momentum differs by 3-4%[5.29]. We are sensitive to a 20% variation in dcs between different momentum bins at each of our incident momenta. No such variation is observed. Let us now set approximate upper limits for $1/2(J + 1/2)K_{el}$ for any narrow resonances compatible with our data.

It is possible to have a resonance strongly coupled to $\bar{p}p$ not showing up in the elastic dcs. This may occur due to interference with the background. However, any interference which cancels the effect of such a resonance requires a special phase relationship between the resonance and background amplitudes. This is not expected to hold for more than a small fraction of resonances, Thus we shall assume that this is not the case in the following discussion where we determine an upper limit for $1/2(J + 1/2)K_{el}$.

The enhancement of dip in the dcs caused by the resonance amplitude at 180^{o} is proportional to the square of $1/2(J + 1/2)K_{el}$ [5.30].

Our data are taken at approximately 40 MeV intervals. We do not see any narrow bumps or dips in excess of 10% of our 180^{o} dcs. Thus, none of the data points show effects larger than 15 μb/sr. For resonances with widths between 20 MeV and 50 MeV, we can set an upper limit of 0.2 for $1/2(J + 1/2)K_{el}$. This is so since at least one of our data points must be within one half-width away from the resonance and thus our data are compatible with a maximum resonance dcs of 40 μb/sr.

For resonances with widths about 10 MeV, our data are compatible with an upper limit of 0.3 for $1/2(J + 1/2)K_{el}$ for these resonances. This is so since the resonance may be 2 or more half-widths away from one of our data points and thus resonance dcs of 100 μb/sr is allowed.

The T and U mesons[5.7] and several mesons suggested by $\bar{p}p$ data[5.15,5.16] are believed to have widths of the order of 10 MeV and thus, if they really couple to $\bar{p}p$, probably have $1/2(J + 1/2)K_{el}$ less than 0.3.

One additional comment needs to be made. If there are many narrow resonances which are clustered close to each other, we would not be able to see the individual resonance effects. However, since each resonance amplitude (for J larger than 0) peaks sharply at 180^{o}, one expects to see backward peaking caused by a combination of these resonances. Interference should not destroy the backward peaking since only resonances in the same J-P-C state interfere with each other. Indeed, above 2.1 GeV, there is backward peaking which appears to hold up to our highest momentum point. Thus, this may indicate possible existence of numerous resonances above 2.1 GeV. Note that both the $q\bar{q}$ and the daughter trajectories models described in Section (c-ii) predict the existence of about 20 resonances between 2.1 and 2.5 GeV capable of coupling to $\bar{p}p$ (see Figures 5.3 and 5.4).

(d-ii) Broad Resonances

Our data revealed two broad structures (by broad, we mean resonances or structures with widths larger than about 50 MeV). There is a 100 MeV wide dip near 2.05 GeV. The slope near 180^{o} turns over from backward dipping into backward peaking as the energy passes

2.05 GeV. The second structure is a 250 MeV wide bump in the 180^{o} dcs centered near 2.25 GeV. Backward peaking exists over the entire range of the bump but it does not appear to go away at energy above the bump.

If each structure comes from one resonance, then the dip being about 100 μb/sr deep, implies that the resonance associated with it has a $1/2(J + 1/2)K_{el}$ of about 0.3. The resonance associated with the bump is also expected to have similar value since the bump is about 100 μb/sr. These structures are not identifiable with either the total cross section bumps[5.8] at 2190 MeV, 2345 MeV and 2380 MeV or the $\bar{p}p$ into charged pion pair structures[5.20] which occur at 2.12 GeV (250 MeV wide) and 2.29 GeV (165 MeV wide).

It is possible that the dip is actually caused by an absence of resonance near 2.05 GeV. Indeed, our data combined with the data of Cline[5.13] (shown in Figure 5.3) indicate a bump in the S region (1924 MeV) below the dip in our data.

Our bump at 2.25 GeV is consistent with a combination of the three suggested resonances in the total $\bar{p}p$ cross section measuremenets. In the following paragraphs and in Figure 5.5, we show an attempt to fit our 180^{o} dcs in the region of our bump with only the three resonances and their values of $1/2(J + 1/2)K_{el}$.

Fitting of our bump structure using the total cross section "resonances"

Assuming that the 180^{o} dcs is entirely due to the effects of the three resonances suggested by the total cross section data[5.8], we can calculate the 180^{o} dcs with the only following freedom:

1. We have to assume the P-C state of each resonance (i.e., singlet,

AT or NT. See pages 121 and 125-129). If two or more resonances are in the same P-C state, interference between the two resonance amplitudes occurs. Also, the size of the 180^{o} amplitude is dependent on the choice of the P-C state.

2. For any resonance in the P-C state of NT (normal triplet), the 180^{o} amplitude has an additional free parameter which varies between 1 and 2. For the other P-C state, the 180^{o} amplitude is completely determined by $1/2(J + 1/2)K_{el}$, except for the sign, which depends on whether J is even or odd.

3. In the case of two resonances interfering, the relative J is important since $Y_J^0(180^{o})$ is proportional to $(-1)^J$.

Each resonance amplitude at 180^{o} is C times $(1/4k)\ 1/2(J + 1/2)K_{el}$ times the Breit-Wigner momentum dependent function[5.8], where k is the cm momentum, C is a factor dependent of the choice of P-C state. C is 1 for the singlet state, $(2)^{-1/2}$ for the AT (abnormal triplet state) and between $(2)^{-1/2}$ and $(2)^{1/2}$ for NT (normal triplet) state.

Figure 5.5 shows the predicted dcs at 180^{o} for particular combinations of assumptions. We see that the fit to our data in the region of the broad bump is quite adequate. Note that it is crucial to have the low mass resonance and one (and only one) of the high mass resonances in the same P-C state so that the constructive interference will prevent a dip between 2.19 GeV and 2.34 GeV. Otherwise, the combination is not unique.

There is evidence that part of the 2.19 GeV bump is due to N* threshold[5.14]. Thus, the $1/2(J + 1/2)K_{el}$ for the possible resonance at 2.19 GeV may be reduced from the value of 0.4. However, we can

Figure 5.5: Resonance prediction in the 180^{o} dcs using the total cross section resonance candidates and their values of $X = 1/2(J + 1/2)K_{el}$. The open circles are our data extrapolated to 180^{o}. The solid line is the prediction for either one of the following combinations I, II, or III.

Mass(GeV)	Width(MeV)	X	I	II	III*
2.19	85	0.4*	NT,C = 1	Singlet	NT,C = 1.33
2.34	140	0.3	NT,C = 1	Singlet	NT,C = 1
2.38	140	0.2	Singlet	NT,C = 1	Singlet

For the three combinations, $(-1)^{J}$ is assumed to be opposite for the 2.19 and 2.34. *For combination III, X of 2.19 is assumed to be 0.3 instead.

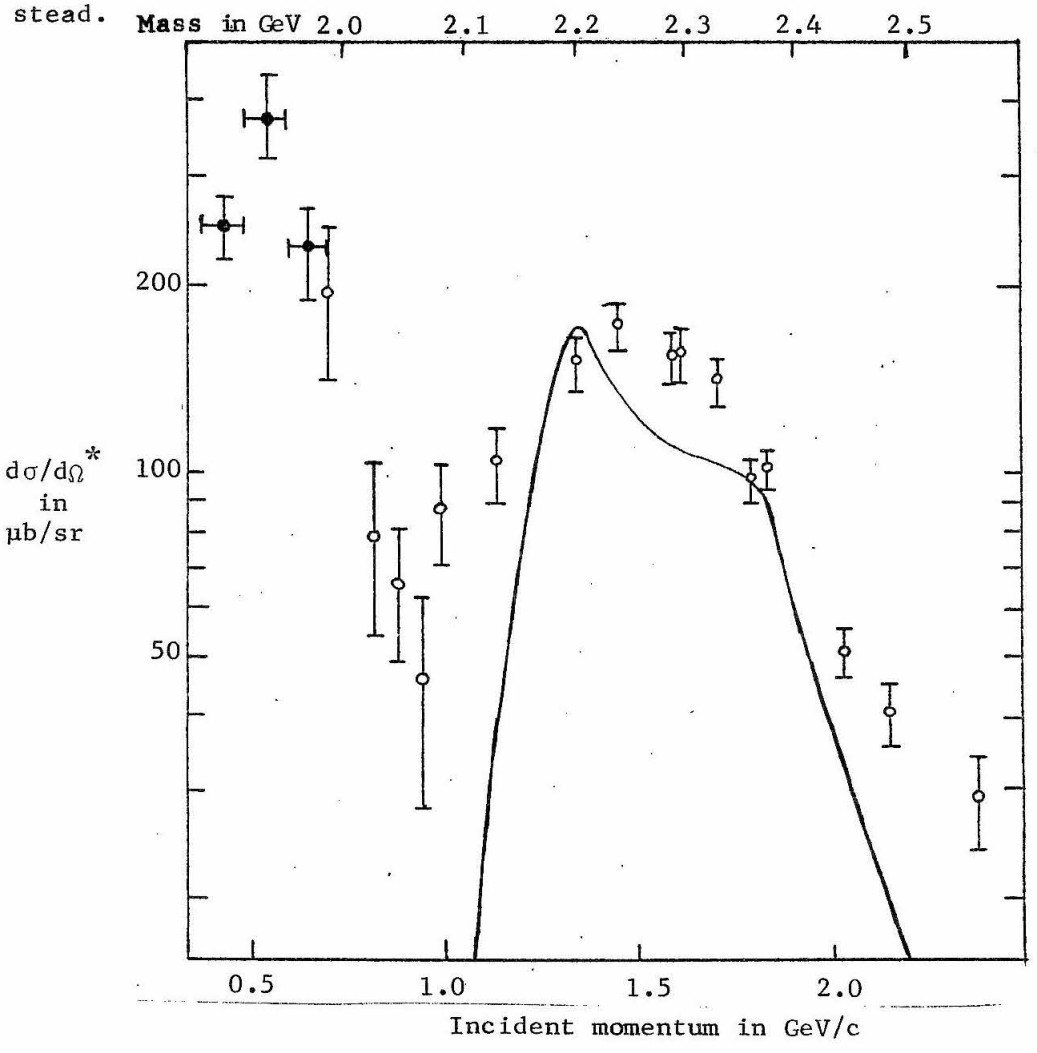

still obtain the fitted curve in Figure 5.5 if $1/2(J + 1/2)K_{el}$ is 0.3 (see combination III).

If we were to add some background amplitudes as well as possible amplitudes for resonances below our mass range, we see that we may be able to approximate our 180^{o} dcs fairly well. The resonance interpretation of the broad bump is also supported by the persistent backward peaking. The slope near 180^{o} suggests that some of the resonances, if they exist, have J's larger than 1.

Although the existence of the three total cross section resonances is consistent with our data, the amount of freedom in our fit is sufficient to make any definite statement difficult.

We summarize our findings about broad resonances as follows:

1. Our data suggest weakly two possible resonance structures -- a 100 MeV wide "resonance" at 2.05 GeV and a 250 MeV wide "resonance" at 2.25 GeV. Both resonance structures suggest a value of 0.3 for $1/2(J + 1/2)K_{el}$. However, the evidence is weak since the first resonance candidate is suggested by a dip while the second is suggested by a bump which does not look like a Breit-Wigner bump. Also, though backward peaking accompanies the bump, the peaking does not go away at energies above the bump.

2. The structures in $\bar{p}p$ into pion pairs[5.20], if they exist as resonances, could not couple very strongly to $\bar{p}p$.

3. Our data in the region of the broad bump can be fitted by the combination of the three total cross section resonance candidates. The number of assumptions for this fit is sufficient to make it difficult for us to say that our data support the existence of these

three resonances.

e. Conclusion on Resonances

We do not provide any strong support for the existence of any single resonance previously suggested. The only resonance candidates whose coupling to $\bar{p}p$ was at all determined were the total cross-section bumps[5.8]. We cannot rule out the existence of these resonances and the strength of the suggested couplings are not incompatible with our data.

We believe that the coupling of any other resonance to $\bar{p}p$ is limited to $1/2(J + 1/2)K_{el}$ of below 0.3 although this may not be true if still other resonances lie close to that resonance. If we assume that J is of the order of 5, the elasticity K_{el} is thus limited to below 10%. This small elasticity is not unexpected since any massive boson would have numerous other decay channels. In particular, the multipion and multi-K-pion channels would be expected to dominate (from phase space factors if not from other factors).

Under the $q\bar{q}$ and daughter trajectories models, bosons are expected to exist in clusters. This would be compatible with the dip at 2.05 GeV in the 180° dcs found in our data since it lies between the S and T clusters. However, one would then expect a similar dip between the T and U clusters near 2.26 GeV. This is not observed. Thus, these models do not appear to be as fruitful as one might expect.

Our experimental data thus revealed that it is hopeless to try to see definite resonance behavior of individual resonance states in backward elastic scattering. Either there are too many resonances close together or the resonance couplings are too weak for unmistakable

resonance behavior to be seen.

Thus, to understand the resonance situation, it would appear that we must study the individual inelastic channels of $\bar{p}p$, do a phase shift analysis using polarization as well as elastic data, or do combined $\bar{p}p$ mass plots of reactions with $\bar{p}$ and p in final state.

CHAPTER VI: DIFFRACTION, AN ALTERNATIVE INTERPRETATION OF THE DATA

a. Introduction and Motivation for this Interpretation

It may be possible to ascribe the dominant behavior of the $\bar{p}p$ elastic cross section to diffraction. Since diffraction is basically quite different from resonance effects (duality connects resonance effects with exchange process but not diffraction although it is considered Pomeran exchange[6.1]). It is interesting to see if the major features of $\bar{p}p$ elastic scattering can be explained by diffraction alone. In this section, we shall give a brief history and motivation for diffraction dominance in $\bar{p}p$ elastic scattering. Sections (b-i) to (b-iii) will describe a particular optical model and its prediction for the elastic cross section, expecially in the region of our data. Section (c-i) covers a brief survey of other diffraction-type models and section (c-ii) contains a discussion of the general features expected from diffraction dominance. Section (c-iii) contains an assessment of the diffraction dominance interpretation of the $\bar{p}p$ elastic scattering with suggestions for future experimentation to test this interpretation.

Forward elastic differential cross section measurements exist in abundance[6.2] and they have been successfully fitted with diffraction-type models[6.3]. Figure 6.1 contains some $\bar{p}p$ forward elastic data showing the strong diffraction peak. In general, the models which many phenomenologists used[6.3] consist of summing partial waves up to L approximately equal to kR (k is cm momentum and R is the radius of the diffraction sphere). A gradual cutoff utilizing an additional para-

Figure 6.1: $\bar{p}p$ elastic dcs in the forward diffraction region. The open circles and triangles are data of Coombes et al., Phys. Rev. 112, 1303 (1958) while the x's are data of Berryhill and Cline (page 335, Proceedings of the 14th International Conf. on High Energy Physics, Vienna, 1968 (CERN)). The lines are the spin-orbit optical model curves, which are described in Section (b).

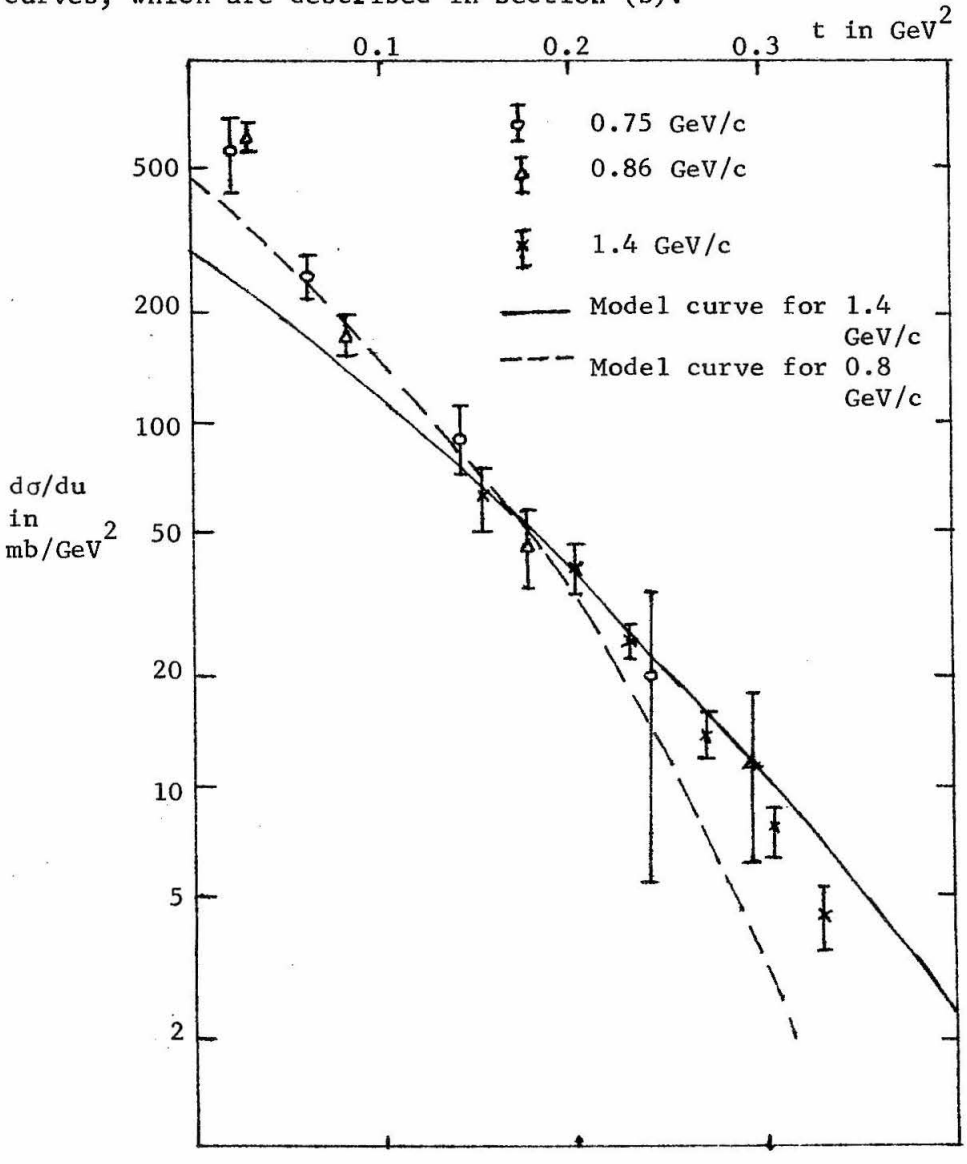

meter called "skin depth" is sometimes used. Many models also have opacity factors which allow some of the lower partial waves to be transmitted through the sphere. The sum over $P_L(\cos\theta)$ is converted to an integral over $J_0((2L + 1) \sin 1/2\ \theta)$ from which one obtains a dcs of $R^2\ (J_1(kR \sin\theta)/\sin\theta)^2$. It should be stressed that the conversion of the sum into an integral involves McDonald's expansion of Legendre Polynomial $P_L(\cos\theta) = J_0(x) + \sin^2 1/2\ \theta\ (J_1(x)/2x - xJ_2(x)J_3(x)/6) + \sin^4 1/2\ \theta(\ ) + \ldots$ (where x is $(2L + 1) \sin 1/2\ \theta$) where only the first term is kept. Thus, the approximation is only valid for small angles.

Figure 6.1 shows the forward $\bar{p}p$ elastic data fitted with a type of diffraction model (see Section (b)). Antishrinking (i.e., decrease in the slope of the peak as momentum increases) of the diffraction exists. The current data suggest that the radius in the diffraction model drops from about 1.6 Fermi at low momentum to about 1.2 Fermi at incident momentum much higher than 1.0 GeV/c[6.4]. So it is well established that diffraction dominates the behavior in small angle $\bar{p}p$ elastic scattering.

Data at $-t = 0.5\ \text{GeV}^2$ region indicate that there is dip in the dcs which appears to be at approximately the same t position independent of incident momentum (although at lower momentum, the dip appears at slightly smaller t value)[6.5]. It is believed that this is the first diffraction minimum[6.6]. Hence, diffraction scattering could still dominate in this region of not-so-small angle scattering. One might therefore ask whether diffraction dominates the entire angular range in $\bar{p}p$ elastic scattering.

Other supporting evidence for diffraction dominance in large angle $\bar{p}p$ elastic consists of:

1. The sharp dip in 180^{o} dcs which we observed near $P_{incident}(\bar{p})$ = 0.95 GeV/c might well be the second diffraction minimum coming into the physical region. The slope of the dcs near 180^{o} in this momentum region is consistent with the incidence of a diffraction minimum since there is backward dipping before the minimum appears and backward peaking at incident momentum above the occurence of the minimum. This concept is schematically illustrated in Figure 6.2a

2. Preliminary unnormalized data of $\bar{p}p$ elastic scattering in the backward hemisphere in the incident $\bar{p}$ momentum region between 0.3 and 0.75 GeV/c by Cline[6.7] appears to be consistent with diffraction dominance. The shape of the dcs, plotted in Figure 6.2b, indicates the possible incidence of the second diffraction maximum into the physical region. The maximum does not remain in constant t. This is consistent with diffraction models since the t values of maxima and minima should increase with momentum[6.6] when they occur at low momentum.

3. Elastic scattering data of $\bar{p}p$ at wide angles by Daum et al.[6.8] show bumps and dips at each momentum. These structures appeared to remain at approximately the same values of t and can be interpreted as diffraction structures.

Some of these data, combined with some other $\bar{p}p$ elastic scattering data[6.9], are shown in Figure 6.3, a 3-dimensional compilation. Observe the bumps and dips which appear to dominate the entire angular range.

Figure 6.2: (a) Schematic drawing of elastic dcs as a function of -t for diffraction model. (a1) momentum below incidence of diffraction dip, (a2) at incidence, (a3) above incidence of diffraction dip showing backward peaking.

(b) Schematic curve of data of Cline[6.7] as a function of t showing the first diffraction dip.

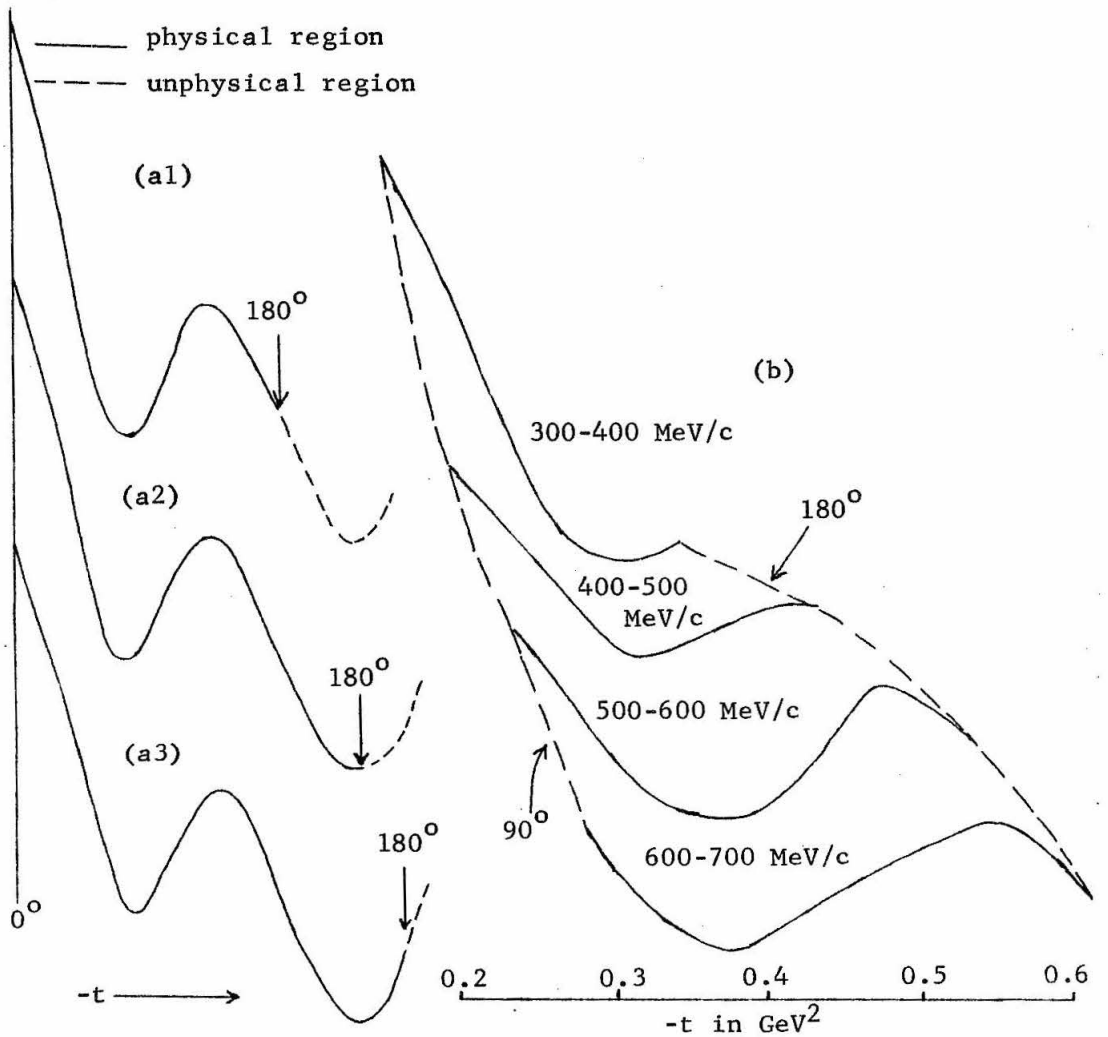

Figure 6.3: A three-dimensional compilation of $\bar{p}p$ elastic data. No. 1 is Cline's data[6.7], 2 is the data of Barish[6.9], 3 is the data of Berryhill[6.9], and 4 is a combination of Daum's and our data.

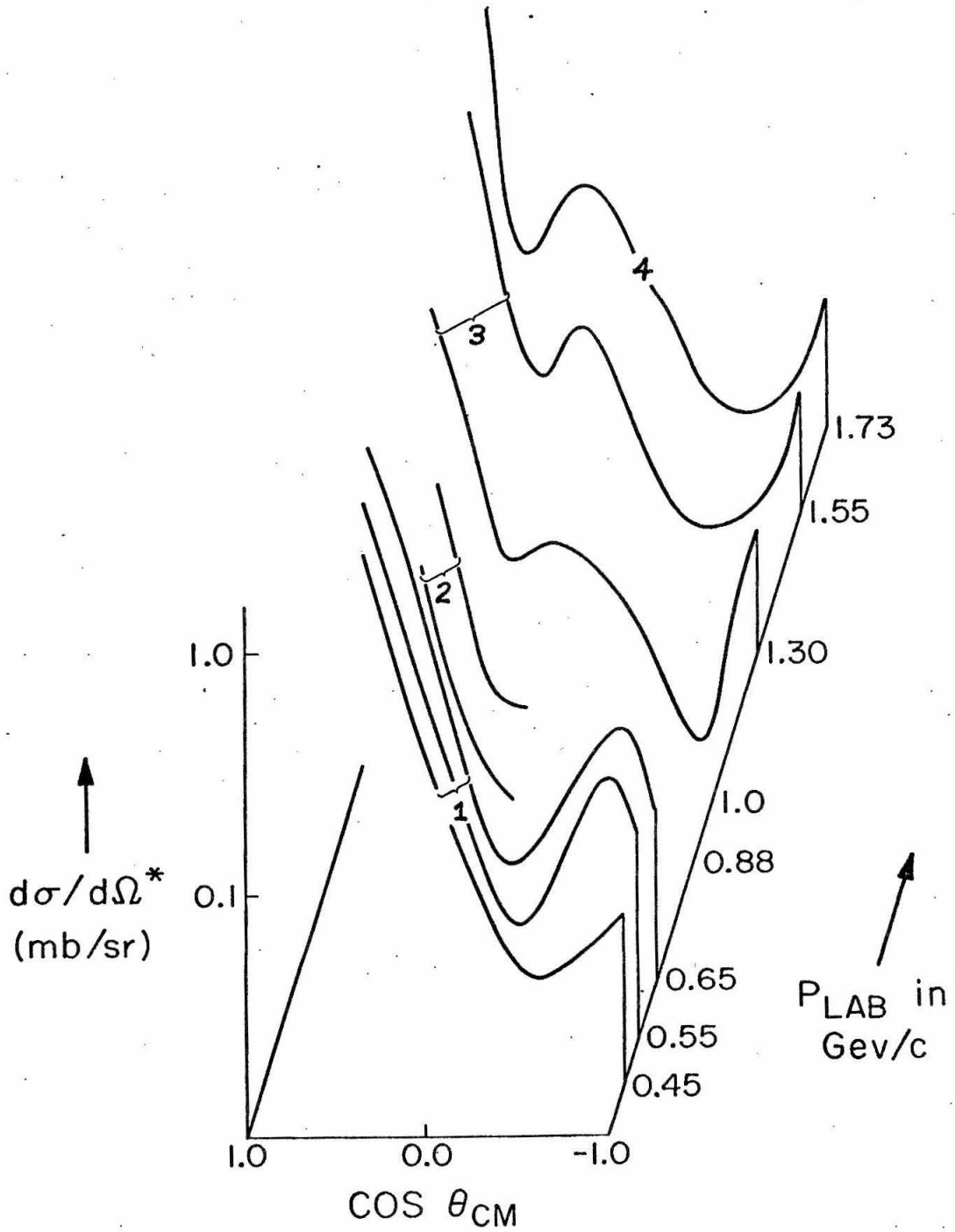

Diffraction dominance could also be motivated from the theoretical standpoint. The existence of strong annihilation channels even at threshold would be a strong incentive for taking this view[6.10]. The probable absence of u channel exchange effects also enhances the possibility of diffraction dominance.

b. Spin-Orbit Optical Model

(b-i) Formulation of the Model

The spin-orbit optical model which we will discuss in this section is a diffused black sphere optical model with spin orbit terms. In deciding on this model, we are motivated by the following considerations:

1. The model should be as simple as is compatible with the data. We have thus used only diffraction terms. No background terms possibly indicating resonance or exchange effects are included. The number of free parameters are kept at a minimum.

2. Since we are dealing with large angle scattering, the small angle approximation used in diffraction fit to the forward peak (see pages 149-151) can no longer be used here. Thus, we should use a model which involves partial wave sums.

3. Since both incident and target particles have spin, we must consider the possibility of spin-orbit and spin-spin contributions. Polarization measurements of $\bar{p}p$ elastic scattering[6.8] reveal appreciable polarization indicative of significant spin dependent contributions. In addition, spinless diffraction models have zeros in the predicted cross section which are not observed in $\bar{p}p$ elastic scattering (see

Figure 6.3). Spin dependent terms would enable these zeros to become minima instead although non-diffractive background could also do this. We have decided to neglect the spin-spin terms and only consider spinless and spin-orbit terms. It may be argued that spin-spin terms, involving the spins of both particles, would not contribute as much to the dcs as the spin-orbit terms.

It remains for us to parameterize the spinless and spin-orbit partial waves. We have decided to use a model similar to the one used by Daum et al.[6.8], which in turn is a modification of an idea by Frahn and Venter[6.10]. The Daum model fitted their $\bar{p}p$ elastic dcs between 1.73 and 2.97 GeV/c fairly well although their polarization measurements at the backward hemisphere appears to be in slight disagreement with the prediction of the model[6.8].

We now formulate the spin-orbit optical model, which is a black (i.e., complete absorption of lower partial waves) diffused (i.e., gradual cutoff of higher partial waves) sphere model. In the absence of spin-spin contributions, the scattering matrix can be expressed in the form[6.12]

$$M = f(\theta) + g(\theta)\ (\vec{s}_1 + \vec{s}_2)\cdot\hat{n} \qquad (6\text{-}1)$$

where f and g are the usual non-flip and spin-flip amplitudes, $\vec{s}_1$ and $\vec{s}_2$ are the spin vectors and $\hat{n}$ is a unit vector perpendicular to both initial and final $\bar{p}$ momenta. The dcs can then be expressed as

$$dcs = |f|^2 + 2|g|^2 \qquad (6.2)$$

The two amplitudes can be expanded in terms of the four partial wave amplitudes (3 triplet and one singlet) for each L of which only

two are independent

$$f(\theta) = (k)^{-1} \sum_{L=0}^{\infty} ((L + 1)R_{L+} + LR_{L-}) P_L(\cos \theta) \quad (6\text{-}3)$$

$$g(\theta) = (i/2k) \sum_{L=1}^{\infty} (R_{L+} - R_{L-}) P_L^{1}(\cos \theta) \quad (6\text{-}4)$$

where $R_{L\pm}$ are the triplet amplitudes for angular momentum L and spin $J = L \pm 1$. We have parameterized the values of $R_{L\pm}$ as

$$\text{Re } (R_{L\pm}) = \frac{1}{2} h(L) \quad (6\text{-}5a)$$

$$\text{Im } (R_{L\pm}) = \frac{1}{2} u^{\pm} d(h(L))/dL \quad (6\text{-}5b)$$

where

$$h(L) = (1 + \exp ((L - kR)/kD))^{-1} \quad (6\text{-}5c)$$

k is the center-of-mass momentum, $u^{\pm}$ are the spin parameters characterizing the $J = L \pm 1$ spin terms, R is the radius and D is the skin depth (which is about the size of the region where h(L) falls from 1 to 0).

Combining (6-5) with (6-3) and (6-4), we obtain

$$f_i \equiv \text{Im } (f) = (i/k) \sum_{L=0}^{\infty} (L + \tfrac{1}{2}) P_L(\cos \theta)/(1 + A) \quad (6\text{-}6a)$$

$$f_r \equiv \text{Re}(f) = - (1/k) \sum_{L=0}^{\infty} ((L + \tfrac{1}{2})u + u'/2) P_L(\cos \theta)A/(kD(1 + A)^2) \quad (6\text{-}6b)$$

$$g_i \equiv \text{Im}(g) = - (1/k) \sum_{L=1}^{\infty} (u'/2) P_L^{1}(\cos \theta) A/(kD(1 + A)^2) \quad (6\text{-}6c)$$

$$g_r \equiv \text{Re}(g) = 0 \quad (606d)$$

where $u \equiv (u^+ + u^-)/2$, $u' \equiv (u^+ - u^-)/2$ and $A \equiv \exp((L = kR)/kD)$.

The f_i term involves a summation of P_L's with coefficient $(L + 1/2)$ times $h(L) \equiv (1 + A)^{-1}$. $h(L)$ is a function which is 1 for L less than $k(R - D)$, practically 0 for L greater than $k(R + D)$ and falls rapidly from 1 to 0 between the two limits. The f_i term is essentially identical with the spinless amplitude of a radius R and skin depth D.

Both f_r and g_i involve sums where the coefficient includes the term $d(h(L))/dL \equiv A/(kD(1 + A)^2)$. This term is practically 0 for L outside the region between $k(R - D)$ and $k(R + D)$ and peaks at $L = kR$. We have parameterized in this fashion since it is believed generally that the spin effects are important only at the "skin" of the sphere[6.13]. Since both f_r and g_i are dependent on u and u', these terms represent the spin-orbit contributions.

At small angles, the f_i term dominates and the result of this model agrees quite well with the usual diffraction model. Away from the forward region, the f_r and g_i terms become comparable in size to f_i for u or u' of the order of 0.2. We shall see in the next two sections how this model agrees with our data and other existing data.

(b-ii) Spin-Orbit Optical Model and our Data

We have attempted to find out what results this model gives in the region of our data. We allow 5 free parameters:
R, D_0 and D_k where $D = D_0 + D_k/k$, u and u'.

Figure 6.4a shows our extrapolated (linear) 180° dcs as a function of incident momentum. Figure 6.4b shows our extrapolated

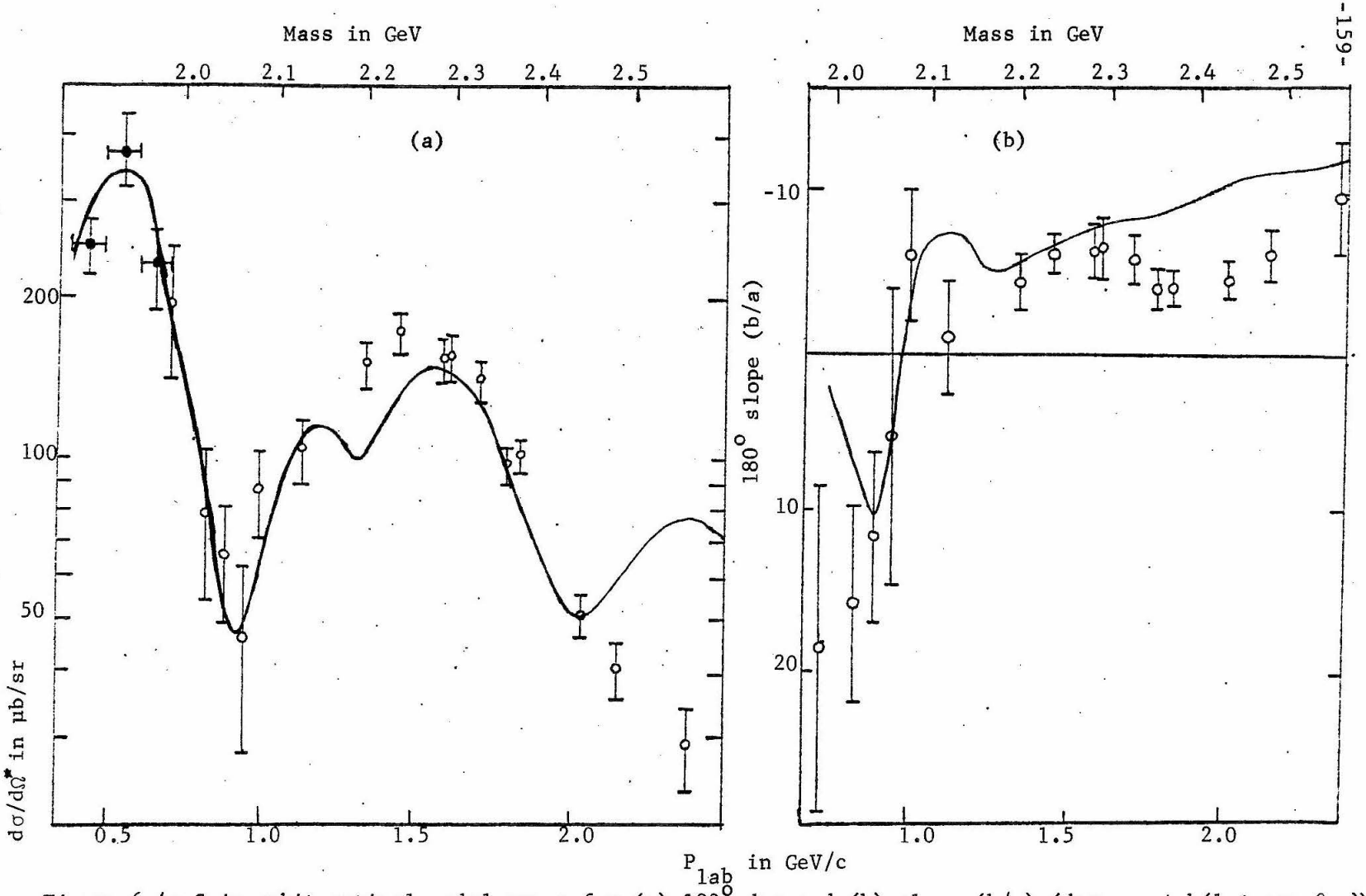

Figure 6.4: Spin-orbit optical model curve for (a) 180^{o} dcs and (b) slope (b/a) (dcs = a + b(1 + cos θ_{cm})) compared with our extrapolated data (open circles) and Cline's data at cos θ_{cm} between -0.95 and -1.0 (closed circles, Ref. 6.7).

Figure 6.5: Our experimental data in μb/sr with optical model curves.

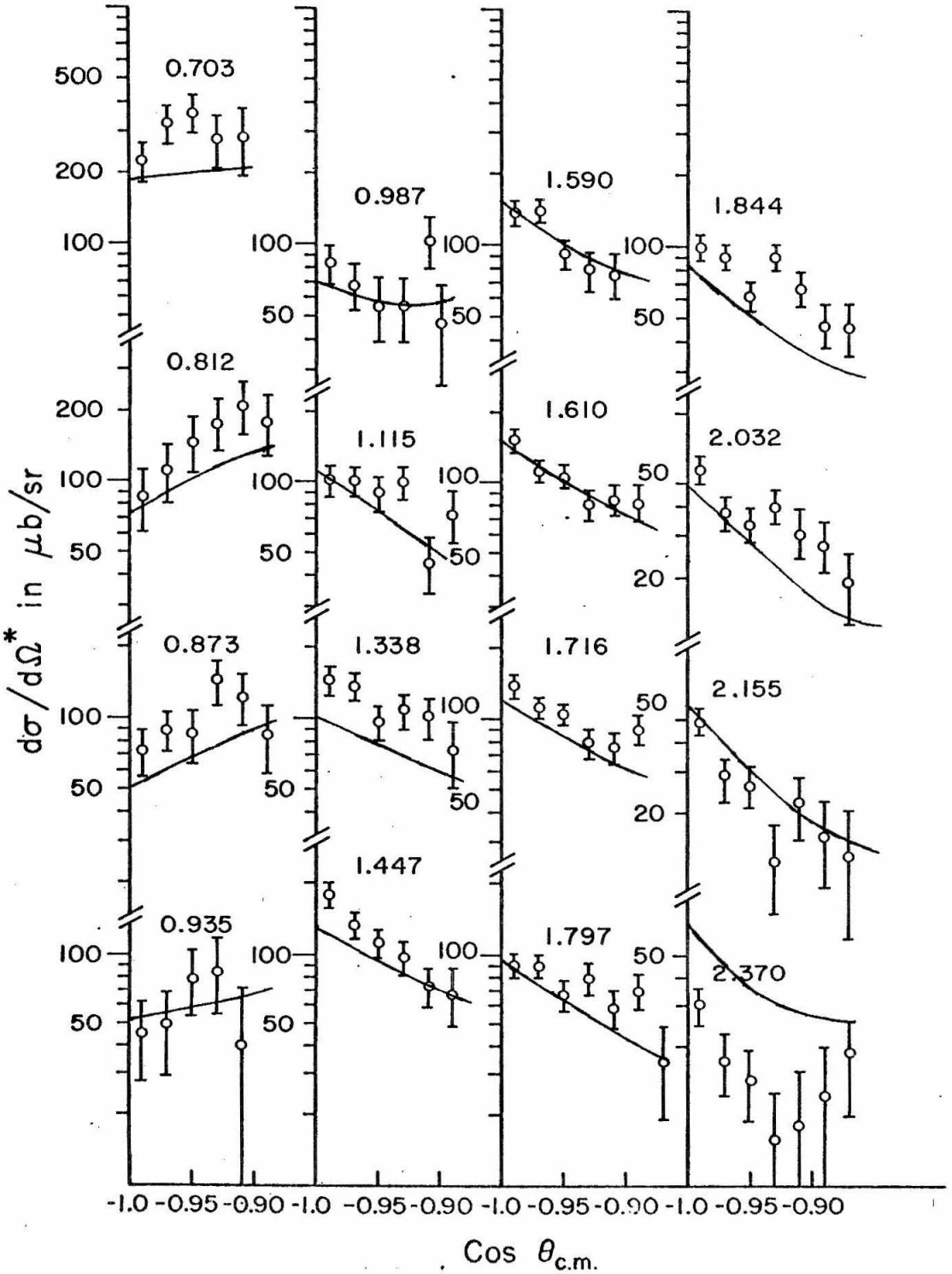

slope at 180^{o}. Figure 6.5 shows our data at several incident momentum. The solid lines in these figures are the spin-orbit optical model curves for the following values of the parameters:

1. R = 0.88 Fermi. This is constrained by the assumption that the dip at 0.95 GeV/c is the second diffraction dip in the f_i term (i.e., the spinless term).

2. D_0 = 0.03 Fermi and D_k = 0.065 Fermi-GeV/c. This is necessary to give the peak at 0.5 GeV/c (Cline's data)[6.7] and 180^{o} the correct normalization and to give the correct normalization in the 180^{o} dcs in the T and U region (1.4 and 1.8 GeV/c, respectively).

3. u = 0.09 for P_{inc} ($\bar{p}$) less than 1.25 GeV/c = 0.40 otherwise. The spin dependent terms have dips where the spinless term (f_i) has bumps and vice versa. Thus, the value of u below 1.25 GeV/c is determined by the deviation of the dip at 0.95 GeV/c from 0. f_i also has a dip at 1.5 GeV/c which is not observed in our data. Thus, u must be much higher at 1.5 GeV/c to fill in the dip. In practice, u must be about 0.4 at 1.5 GeV/c to give the correct normalization. Between 1.0 and 1.4 GeV/c, the size of u is unimportant. We have used a step function although a gradual increase is also acceptable. Above 2.0 GeV/c, if u is decreased, the 180^{o} dcs would be somewhat smaller and agree better with our data.

4. u' = 0.5. The size of this parameter is unimportant. If this value is reduced by a factor of 2, u can be changed slightly to compensate and the result will be essentially the same.

From the figures, we see that the optical model curves fit the

data quite well. In particular, the bump at 0.5 GeV/c and the dip at 0.95 GeV/c in the 180^{o} dcs are reproduced accurately. However, there is a slight dip at 1.3 GeV/c which may be inconsistent with our data (the dip in the model curve is about 20%). If we restrict the radius to be the same for f_i, f_r and g_i and allow only spin-orbit terms of the form we used, this slight dip cannot be removed. This is due to the fact that it is in between the bump in f_i and bump in f_r. This dip can be removed if we allow spin-spin terms or if we allow different radius for the spinless and spin-orbit terms. However, this would imply the addition of several free parameters and complicate the model, which we prefer not to do.

The angular shape of the data (see Figure 6.4b and 6.5) is also reproduced fairly well. The model curves give backward dipping below and backward peaking above 0.95 GeV/c.

Thus, this simple model with 4 energy-independent parameters and one variable parameter (which takes on only two values) reproduces the results of our experiment to a good degree. In the next section, we shall compare the prediction of this model with other $\bar{p}p$ elastic data and see how it fares.

(b-iii) Assessment of the Spin-Orbit Optical Model - Does it Reproduce Other $\bar{P}P$ Elastic and Polarization Data?

For the same values of the parameters we use to reproduce our data, we try to see how closely the model prediction matches other data. We consider three $\bar{p}p$ elastic regions: 1) forward diffraction region, 2) low energy elastic data region, and 3) other elastic data

regions and also polarization data of $\bar{p}p$ elastic scattering.

Forward diffraction peak region

As we mentioned in Section (a), the optical model, with just a spinless term, fits the forward diffraction peak very well with the assumption of a radius of about 1.2 Fermi. In our model, the spin-orbit contribution enhances the forward diffraction slightly. However, the radius of 0.88 Fermi which is necessary to match the 180^{o} dcs is incompatible with the data on forward diffraction peaks (the spin-orbit optical model curve for 0.88 Fermi is drawn as a dashed line in Figure 6.1, which contains the forward diffraction peak data). The spin-orbit optical model curves are too gentle and the 0^{o} dcs is too low. Thus, it would appear that if our model is to reproduce the behavior at both 0^{o} and 180^{o}, we may have to vary the radius as a function of angles. Nevertheless, the qualitative features of the forward diffraction peak are reproduced by our model.

Low energy elastic data region

The existing $\bar{p}p$ elastic data in this region consist of some forward diffraction peak data discussed above and the backward hemisphere elastic measurements of Cline[6.7] which cover 0.3 to 0.75 GeV/c (data at higher momentum is forthcoming). Cline's data are sketched in Figure 6.6a along with the result of our spin-orbit optical model, which is drawn in dashed lines. Qualitatively, the fit is quite good. However, it would appear that a better fit would result if the bump-dip structures are moved to slightly smaller t values. This is consistent with increasing the radius slightly to about 0.95 or 1.0 Fermi. Thus, the data in this region also suggest

Figure 6.6: The spin-orbit model curve (solid lines) compared with

(a) Cline's low momentum $\bar{p}p$ elastic data (Ref. 6.7).

(b) Berryhill's data at 1.4 GeV/c (Ref. 6.9 and page 335 of Proc. Int. Conf. on HEP, Vienna, 1968 (CERN)).

(c) $\bar{p}p$ polarization measurements at 1.73 GeV/c (Ref. 6.8).

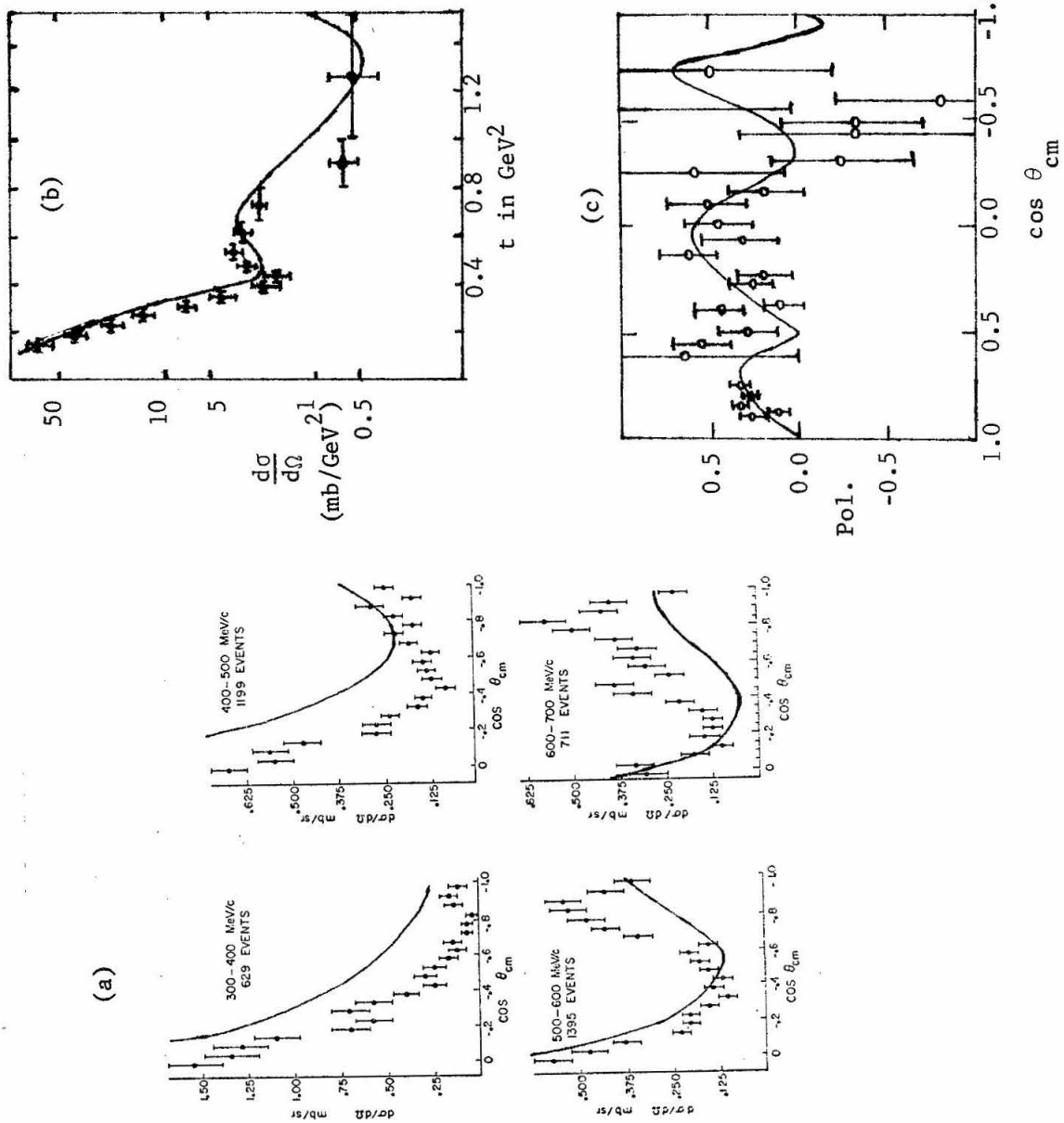

a slight variation of radius with angle.

Other elastic data regions

We shall concern ourselves with only the intermediate momentum region (incident momentum less than 3 GeV/c) which includes data by Barish[6.9], Berryhill[6.9] and Daum[6.8]. Data at higher momentum exist, but are not useful beyond the first diffraction dip due to poor statistics. The intermediate region data have been included in Figure 6.3. In Figure 6.6b, we show a plot of the data by Berryhill with the results of our spin-orbit optical model. We see that the structures apparent in the data are reproduced quite well by the model curve. Again, a slightly better fit would result if we increased the radius so that the dip and peak occur at smaller t values.

Polarization data

Daum et al.[6.8] also measured the polarization of $\bar{p}p$ elastic scattering using a polarized proton target. Thus, we can compare the results of our model with the polarized data since the polarization, in this case is

$$\text{Pol.} = 2\ \text{Re}\ (fg^*)/\text{dcs}. \qquad (6.7)$$

We show the polarization data and our optical model results in Figure 6.6c. We see that the fit is qualitatively quite reasonable in the forward region but deteriorates towards the backward hemisphere. The size of the polarization is of the same magnitude as the optical model results. Even if there is disagreement in the size,

we can adjust the value of u' which affects the polarization drastically but only affects the dcs slightly.

The major prediction of the model as far as polarization is concerned is the prediction of zeroes at the position where the elastic dcs shows dips. These zeroes are caused by zeroes in f_i since Re $(fg^*) = f_i g_i + f_r g_r$ and g_r is identically 0 in our model. The polarization data do suggest zeroes or minima at the appropriate places although the data are not sufficiently good to be decisive. If these dips are actually minima rather than zeroes, this would probably imply that spin-spin terms (which contributes to g_r) are not negligible. The fact that the zeroes or minima appear as predicted by the spin-orbit optical model indicates, however, that spin-orbit terms do dominate over the spin-spin terms.

Another result of our model is that the polarization should be positive only (slight negative polarization is allowed only near 180^o). This is verified reasonably in the forward hemisphere.

Daum et al. fitted their data with a similar model but allowed the parameters to vary at each momentum without energy dependent constraints. However, their model results are similar to ours.

In conclusion, the spin-orbit optical model fits the data qualitatively quite well. The shapes of the structures in the elastic scattering and polarization data of $\bar{p}p$ are reproduced by the model. However, quantitative fit would require varying some of the parameters which we have kept fixed. For example, the forward diffraction data requires a larger radius than was used by us to fit the 180^o dcs. Also, data near 90^o suggest that the radius may have to be in-

creased in that angular region to shift the dips to the observed values. Polarization data may also be better fitted if spin-spin terms are introduced.

However, any attempt to make a more sophisticated model would destroy the simplicity and beauty of this model. In addition, the current state of the data -- especially the polarization data -- is such that a detail fitting with a complicated model with many additional free parameters is unwarranted.

Considering that over the entire range of momentum below 3.0 GeV/c we used only 4 energy-independent and 1 energy-dependent parameters, the fact that the spin-orbit optical model qualitatively fits the data is quite impressive. Thus, diffraction dominance of the $\bar{p}p$ elastic scattering appears to be justifiable.

c. Diffraction Dominance and $\bar{p}p$ Elastic Scattering

(c-i) Brief Survey of Other Diffraction Type Models

Other parameterizations of partial wave amplitudes have been used to fit elastic data of many reactions[6.14]. Usually, these involve either introduction of opacity factors reducing absorption of lower partial waves (grey sphere models) or different parameterization of the $R_{L\pm}$ amplitudes in page 157. However, these changes are unimportant qualitatively in that the positions of the structures are not shifted by significant amounts.

Another alternative is to use the complete $\bar{p}p$ amplitudes including all spin terms[6.12]. This will give a total of 5 scattering amplitudes for each L instead of 2 (3 additional amplitudes representing

spin-spin contributions and containing P_L^0's, P_L^1's and P_L^2's are added). The detail fitting to the data would therefore be more versatile at the expense of more parameters. In any case, it is expected that spinless terms like $(2L + 1)P_L$ would still dominate the dcs. Thus, the result of this kind of model would still be qualitatively the same as our spin-orbit optical model.

It is also possible to use a multiple scattering model to try to fit data with bump-dip structures[6.15]. In brief, double scattering would give a flatter decrease as a function of angle than single scattering. Destructive interference between the various scattering amplitudes would lead to bump-dip structures whose position depends on the relative strengths of the scattering amplitudes. One can also go further by assuming the quark or parton structure of $\bar{p}$ and p[6.16]. However, the result of this type of model would be similar to that of our diffraction model.

Thus, other models give results qualitatively similar to that of our simple spin-orbit optical model.

(c-ii) Features of Diffraction Dominance in $\bar{p}p$ Elastic Scattering

Now we discuss the general features which are expected in any type of diffraction dominance model.

The essential nature of a diffraction model is the interference of various L waves which causes the interference pattern. The position of the bumps and dips should be dependent on the radius which one assumes. The bumps and dips should occur in a regular pattern and, as a function of energy, should stay at fairly constant t values (at large angle regions, the t values of these structures

should increase slightly as energy increases[6.5]).

Spin-dependent terms are not expected to be important in the forward diffraction peak region. However, the spinless contribution decreases quite rapidly as angles increase. Thus, spin dependent terms will contribute significantly and fill in some of the interference dips in the spinless contribution. If diffraction structures still dominate at backward angles, then we expect that the shape of the dcs will be as drawn in Figure 6.2a. However, spin dependent terms may modify this kind of structure.

(c-iii) Assessment of Diffraction Dominance and Suggestion for Further Experimentation

Diffraction dominance in the forward elastic $\bar{p}p$ scattering is well established. The existence of the first diffraction dip and a second maximum can also be viewed as evidence of diffraction dominance. Thus, diffraction dominance in the forward hemisphere is fairly justifiable.

As for the backward hemisphere, the data of Cline[6.7] at low momentum appear to be consistent with diffraction dominance although finer structures (with poor statistics) suggesting possible resonances were claimed. Otherwise, the intermediate momentum data of Berryhill[6.9], Cooper[5.14] and Lys[5.17] as well as our data near 180^{o} (see Figure 6.4 and 6.5) are consistent with diffraction dominance.

We conclude that, although direct channel resonance effects may be present, diffraction dominance of $\bar{p}p$ elastic scattering is

consistent with existing data. Indeed, there is no major structure in the $\bar{p}p$ elastic scattering which contradicts diffraction dominance.

In order to test this concept, it is essential to 1) get better measurements (with statistical errors of the order of our experiment) of $\bar{p}p$ wide angle elastic scattering at intermediate or high momentum to try to see diffraction structures, and 2) get better measurements of polarization with polarized beams and target to look for diffraction structures. Eventually, a phase shift analysis, in addition to clearing up the resonance situation as described in the last chapter, may be able to force us to either discard or accept diffraction dominance in $\bar{p}p$ elastic scattering.

CHAPTER VII: SUMMARY AND CONCLUSION

a. Summary

We have presented data on $\bar{p}p$ backward elastic scattering in the intermediate energy region, the methods we used to acquire them, and two interpretations of the data.

Our experimental apparatus is essentially a missing mass spectrometer using wire spark chambers with digitized magnetostrictive delay line readouts to records the events. Antiprotons are incident on a liquid hydrogen target. The recoil proton from a backward elastic event is identified by a combination of time-of-flight measurements and gas threshold Cherenkov counter measurements. It is momentum analyzed by a magnet sandwiched between two sets of wire spark chambers which record the recoil proton trajectories.

An off-line program reconstructs the event trajectories from the spark positions and another program makes the appropriate cuts to remove all background events. We thus obtain the net number of backward elastic events. We calculate the angular acceptance of our apparatus using a Monte Carlo program. We study all sources of inefficiencies and losses and obtain the values of the various corrections necessary to obtain the proper normalization. We are then able to obtain the differential cross section for $\bar{p}p$ backward elastic scattering for 16 momenta between 0.7 and 2.37 GeV/c incident $\bar{p}$ momentum in several angular bins for $\cos \theta_{cm}$ between -1.00 and about -0.88.

The data which we obtained agree with three other sets of $\bar{p}p$

backward elastic measurements in the regions where there are overlaps. Our data show a sharp dip at 0.95 GeV/c and a broad hump near 1.4 GeV/c when the 180^{o} differential cross section is viewed as a function of momentum. As for the slope away from 180^{o}, our data indicate backward dipping below 0.95 GeV/c and backward peaking above 0.95 GeV/c.

We do not see any strong evidence for a strong u channel contribution from a single Regge trajectory over the entire range of our data. This is not unexpected since u channel exchange for $\bar{p}p$ elastic interaction would require the existence of particles with B and Q equal to 2. Such particles are not known to exist.

Our data show no behavior which can be attributed to any single resonance suggested by previous experiments although the broad hump could be due to the combination of effects from the three possible resonances found in $\bar{p}p$ total cross section[5.8]. Except for very narrow (widths less than 10 MeV) resonances which we may have missed, we believe that our data indicate that the coupling of $\bar{p}p$ to any resonance in our mass region is limited to $1/2(J + 1/2)K_{el}$ of less than about 0.3. Resonances in our mass range either couple too weakly to $\bar{p}p$ or are too close together for any single resonance to reveal itself unmistakably in backward elastic $\bar{p}p$ scattering.

Diffraction dominance appears attractive since diffraction is known to dominate the forward $\bar{p}p$ elastic scattering and no strong u channel effects are expected (as mentioned above). We have attempted to reproduce our data with a simple diffraction type model and found very good qualitative agreement. This model with the same

values of the parameters is also qualitatively consistent with other elastic $\bar{p}p$ data.

b. Conclusion

Our data revealed that it would not be profitable to search for unmistakable characteristics of resonances in backward elastic $\bar{p}p$ scattering. The resonances are either too close together or couple to $\bar{p}p$ too weakly for the individual resonance characteristic to show itself clearly. Thus, resonances in the direct $\bar{p}p$ channel must be revealed by other means -- 1) searching the inelastic $\bar{p}p$ channels, 2) searching the combined $\bar{p}p$ mass plot for reactions with $\bar{p}$ and p in the final states, and 3) using phase shift analysis of $\bar{p}p$ using elastic as well as polarization data.

Our data suggest that diffraction dominance may be approximately true for the entire angular range in $\bar{p}p$ elastic scattering. All the qualitative features of our data as well as other elastic data can be ascribed to diffraction dominance. Although this does not rule out possible resonance effects, it does suggest that resonance contributions in the elastic differential cross sections even at extreme large angles, may be small. An accurate polarization measurement would do a great deal to strengthen or weaken this possibility.

Thus, our data, although it cannot add much to the resonance situation, do enable the diffraction dominance idea to appear more attractive.

APPENDIX A: BEAM TRANSPORT SYSTEM

The beam transport system we used is the short branch of the partially separated beam No. 5 at the AGS in Brookhaven National Laboratory[2.5]. It is shown in Figure 2.1 (page 10). The system consists of 7 quadrupoles, 3 dipoles, 2 electrostatic beam separators, 2 beam stops, a mass slit and a vacuum system covering the first part of the beam transport. A sextupole exists to correct the chromatic aberration of the beam but was not utilized in our experiment.

At the Alternating Gradient Synchrotron (AGS) of Brookhaven National Laboratory (BNL), every 2.4 seconds, an accelerated proton beam of proton intensity between 0.7 to 1.5 x 10^{12} particles strikes an internal target (which is flipped into the beam) for a duration of approximately 400 msec. The beam transport system we utilized, the partially separated beam No. 5, focuses particles produced at 10^{o} to a target at the 10th magnet of the G-superperiod. The target, a Be wire 1 mm in diameter, is pointed at 10^{o} so as to present the smallest possible source to the beam transport system.

The momentum of the beam particle is selected by the first dipole bending magnet while the two electrostatic separators, coupled with the mass slit, reject the majority of particles with the wrong e/m ratio.

The first three quadrupoles Q_1, Q_2 and Q_3 are special magnets with most of their material above and below the magnet. Thus, they can be placed very close to the AGS main ring. Their purpose is to focus all particles of the appropriate momentum within a $\pm$ 14 mr

horizontal and ± 9 mr vertical acceptance into a parallel beam. Such a beam is bent horizontally by the first dipole (the particles of the desired momentum are bent 6^{o}). Figure A.1 shows a ray trace diagram for both horizontal and vertical deviations from the beam line of the extreme angle rays.

Q_4 and Q_5 focus the particles of desired momentum p_0 horizontally at H_0 and vertically at V. Particles of slightly different momentum will focus at places which are off to the side of the beam line. This allows us to place momentum slits at the appropriate places which will cut off all particles with momentum more than a certain allowance from the desired momentum p_0. For example, the momentum slit at H_{+2} in Figure A.1 is so placed that all particles with momentum above 1.02 p_0 will be removed. During most of our experiment, we set the momentum slit at ± 3%.

All particles are focused vertically at V. This allows us to remove wrong velocity particles (i.e., pions and kaons) by using the two beam separators to deflect these wrong velocity particles vertically and by using a mass slit with a narrow vertical aperture at V. The pion background of the $\bar{p}$ beam is reduced by more than a factor of 50.

D_2, which is situated right after Q_5, is used to bend the beam to our branch of the beam system. The sextuple, situated at H_0, is not used. D_3 bends the beam further away from the other branch, sweeps away any low energy junk created at the mass slit and recombines momenta at the hydrogen target.

Finally, Q_6 and Q_7 focus the remaining beam at the target area.

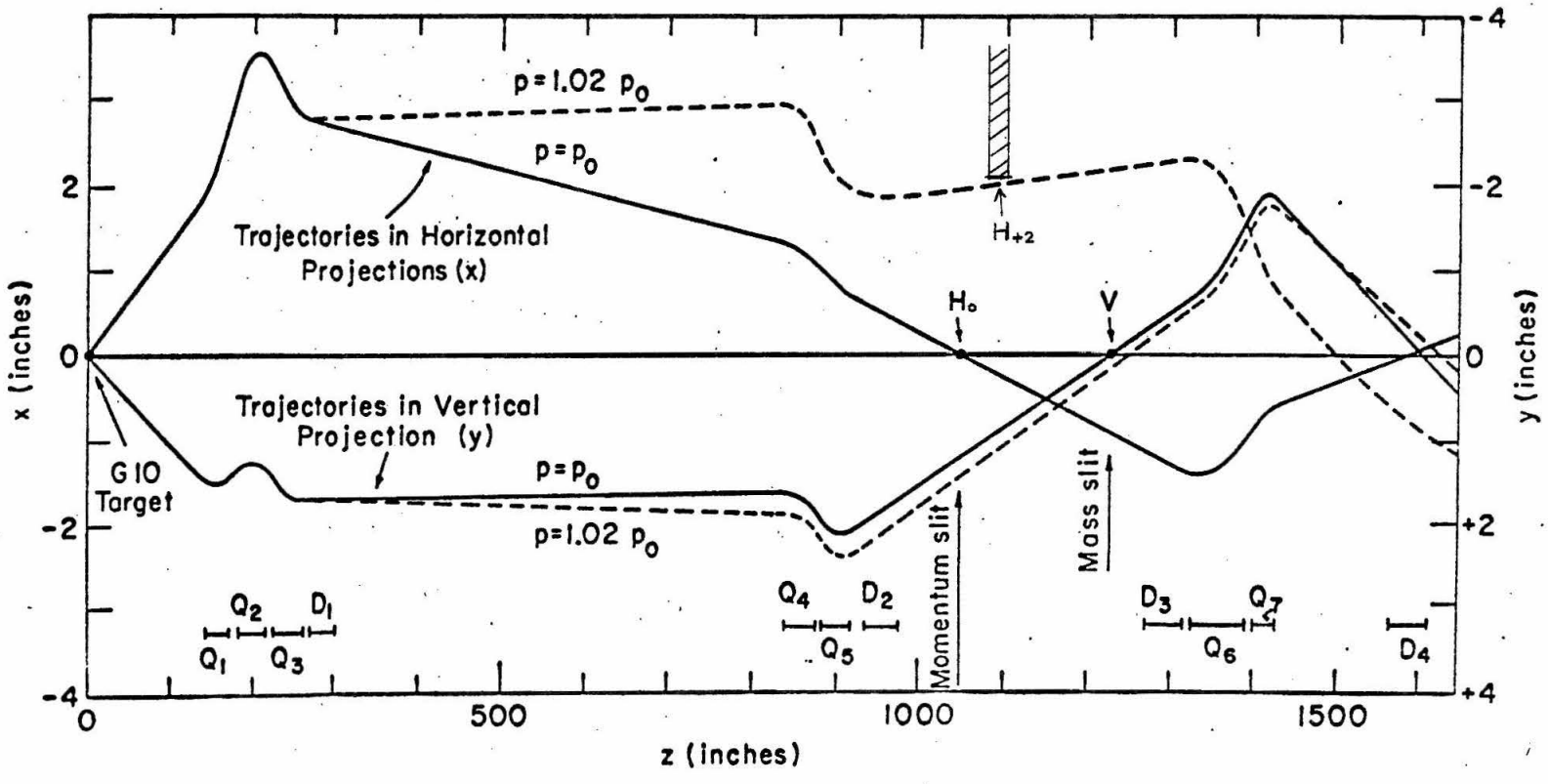

Figure A.1

Ray traces of the trajectories of particles passing through the beam transport system.

The size of the beam at the target area, as can be seen in Figure A.1 is less than 1-1/2 inches in diameter.

APPENDIX B: WIRE SPARK CHAMBERS

(B-i) Introduction

For each incident particle event meeting the trigger condition, we must record the positions of the trajectories of the 1) incident $\bar{p}$, 2) the outgoing recoil proton before, and 3) after its trajectory is deflected by the magnet. This is necessary in order to reconstruct the event and determine whether the event is a backward elastic event. We use three sets of four wire spark chambers with magnetostrictive delay line readouts[B.1] to record the three trajectories.

The physical construction of the wsc (wire spark chambers) is described in Section (B-ii). The high voltage pulsing system is discussed in (B-iii). Section (B-iv) contains a discussion of the clearing field system which removes ionization products from earlier particles and sparks. We describe in Section (B-v) the gas system used to maintain a mixture of neon, helium and alcohol vapor needed for optimum sparking characteristics. The magnetostrictive delay line readout system is described in Section (B-vi). Sections (B-vii) contains a discussion of the characteristics and response of the wire spark chambers, including the resolution, memory time and recovery time. A brief assessment of the use of these wire spark chambers in our experiment is contained in Section (B-viii).

Figure B.1 shows a schematic drawing of the components and operation of the wsc.

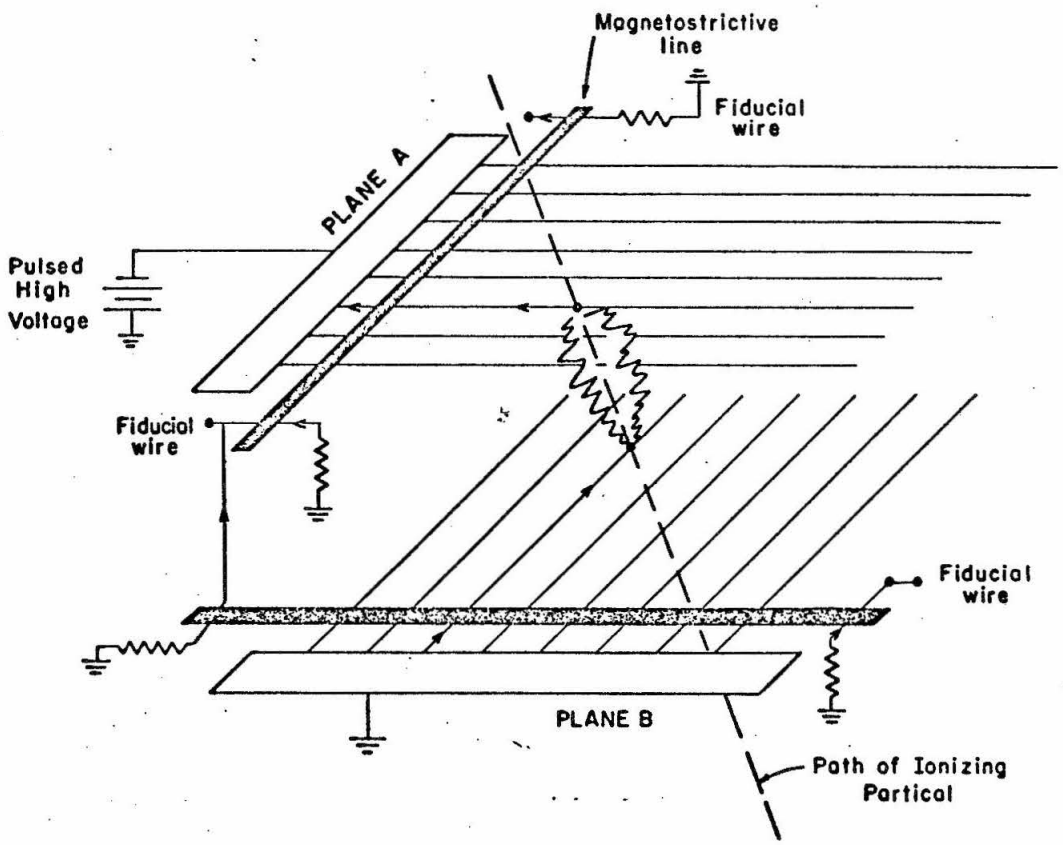

Figure B.1

Schematic of the operation and components of the wire spark chambers. A spark forms along the path of the ionizing particle. Current flows through the wires (denoted by arrows) coupled by the spark. Marker pulses are placed on the magnetostrictive lines by the fiducial wires.

(B-ii) Physical Construction of the Wire Spark Chambers

Figure B-1 shows a schematic drawing of the wsc. The wire planes each consist of parallel coplanar wires 25 mils thick and the centers 50 mils apart etched onto fiberglass epoxy sheets 3/4 mil thick. Two wire planes are mounted on a 1/8" thick fiberglass frame so that they are 1/4" apart. The wires in one plane are set perpendicular to the wires on the other plane. All the wires on each plane are connected to a bus bar (one for each plane). One of the bus bars is grounded while the other is connected to the output of the high voltage end of the pulsar system to be discussed in the next section. Magnetostrictive wires are placed between the sensitive areas of the wsc and the bus bar to detect the current of a spark.

For support, the fiberglass frame is further mounted on a 1/2" thick aluminum jig plate. A mylar envelope is put on the outside of the wire planes to maintain the necessary gas mixture between the planes.

(B-iii) The High Voltage Pulsing System

When a logic signal from the trigger logic arrives, the wire spark chambers must be triggered. That is, high voltage must be applied between the planes of the wsc in a short time so that the ionization from passing charged particles can be accelerated and made to produce spark avalanches. This will produce current flow along certain wires. The readout system records the information of which wires have current flow and thus allows the positions of the sparks to be determined.

The process of pulsing the wsc planes is as follows:

1. A pulse driver converts the trigger logic signal into an output of 800 volts with a width of 80 nsec. There is a delay of about 20 nsec between the input and the output. The timing of the pulsing system is included in Figure 2.14, the timing diagram for our entire recording procedure (pages 53 and 54).

2. The pulse driver output is shared by twelve high voltage pulsers (one to each chamber). The principal elements of the pulser are a storage capacitor and a hydrogen thyratron[B.2]. The storage capacitor, charged to a high voltage of between 4.8 to 5.6 kilovolts, shares its charge with the chamber capacitance through the thyratron, which is shorted about 60 nsec after the pulse driver signal is received. The thyratron is clamped off by the inductive kickback produced by the trailing edge of the pulse driver pulse. Thus, the chamber capacitance is charged only for a period of 20 nsec. The actual high voltage across the wire plane is about 60% of the original high voltage across the storage capacitor. Since the spark formation time is about 30 nsec, the thyratron is switched off before the discharge. This limits the energy dissipated and prevents the spark from becoming self-sustaining and damaging the chamber.

If the spark discharge does not occur, the chamber is discharged through a bleeder resistance R such that the time constant RC is about 200 nsec.

3. High voltage power supply exists for each pulser to charge the storage capacitor.

The actual time of discharge (see Figure 2.14, page 53 and 54) occurs approximately 300 nsec after the event. This delay is imposed

by (a) the counter photomultiplier delay and cable delay prior to the trigger logic, which totals about 100 nsec. (b) the trigger logic module delay of about 50 nsec and (c) the pulsing system delay of about 150 nsec (20 nsec pulse driver delay, 60 nsec thyratron delay and 30 nsec spark formation time plus more than 20 nsec of cable delay).

(B-iv) The Clearing Field

We apply a DC clearing field across the two planes of the wsc to sweep away ionization from old tracks. A DC clearing field of 17 volts is used which gives the wsc memory time of about 1000 nsec[B.3]. Large amounts of residual ionization remain after each spark avalanche. These are removed by a pulse clearing field of a few hundred volts which is applied after each pulsing of the wsc.

(B-v) The Gas System

Optimum response of the wsc is obtained by using a mixture of 90% He, 10% Neon and 1% Isopropanol[B.4] (we discuss the response under different circumstances in Section (B-vii)). This mixture of gases is maintained between the wire planes using one of the following systems[B.5]:

1. A feed-through system which forces the gases through the wsc mylar envelope using a slight overpressure to maintain flow. There are outlets for each chamber consisting of tubes whose openings are just below the surface of a liquid to allow gas to escape.
2. A recycling system which purifies the exhaust gases[B.6] and recycles the gases through again. Small amounts of additional gas are added continuously to compensate for loss through leakage.

Both systems bubble the gases through Isopropanol at $0^{o}C$ which gives the desired proportion of Isopropanol.

(B-vi) The Magnetostrictive Delay Line Readout System

The information of which wire(s) carried the spark avalanche current must be obtained so that the spark position can be determined. This is handled by the magnetostrictive delay line readout system.

Magnetostriction[B.7], a deformation induced by a change in magnetization, will propagate with the speed of sound. If the material is a wire, the transverse deformation waves can be suppressed. Thus, magnetostrictive waves can travel down a wire.

We use a wire made of iron-cobalt[B.8] which is placed next to the wires of each plane (see Figure B.1). The current going to or coming from the bus bar must pass over the readout wire. This induces a magnetostrictive deformation wave in the wire which is propagated to both ends of the wire. The wave is damped at one end. The wave is picked up at the other end by a coil of wire and amplified into a signal. Fiducial wires (see Figure B.1) marking the limits of the sensitive areas are placed over the readout wire and are pulsed every time the wsc is pulsed. This provides reference signals from which the spark signals can be calibrated. The deformation wave in the wire we use has a velocity of 5.2×10^{5} cm/sec. This allows the position of the spark current wire to be determined w.r.t the fiducial wires through the time delay between the arrival of the two pulse signals.

The output of the readout amplifier for each coordinate is transmitted to the readout wire of the next coordinate through a

transmitter (see Figure 2.13, top half, page 47). So, the entire spark signals from all 12 wsc come in a single wave train. This serial readout signal train is handled by the digitizer, as described in Section (d-i) of Chapter II (page 44). That section also contains a brief discussion of the merits and faults of the serial readout system.

(B-viii) Characteristics and Response of the Wire Spark Chamber System

In this section, we discuss the various characteristics and responses of the wsc, including memory time, recovery time, and resolution.

Memory time

We have applied a DC clearing field of 17 volts across the wire planes, restricting the memory time of the wsc to about 1000 nsec[B.3]. The memory time has to be within certain limits. The actual spark chamber discharge occurs approximately 300 nsec after the event (mentioned in page 181). Thus, the memory time must be at least several factors larger than this number. In our case, we have verified that the memory time is at least 100 nsec more than the 300 nsec normal spark discharge delay. This is done by artificially delaying the wsc discharging by 100 nsec. No appreciable decrease in efficiency is observed.

On the other hand, we are limited by the rate of incident particles. Since the beam halo rate is as much as 1/2 megacycle, one particle arrives each 2000 to 4000 nsec. Thus, to prevent the recording of too many spurious tracks, we would like to have the

memory time as short as possible. Since the memory time has to be at least of the order of 300 nsec, we have chosen 1000 nsec as a safe compromise. In order to decrease the number of extra tracks, we use a pile-up gate which prevents any $\bar{p}$ that comes within 500 nsec of any previous particle from initiating a trigger. This actually reduced our useful $\bar{p}$ flux by 15 to 30 percent. Most of our extra tracks come from passage of particles during the 300 nsec between the event and the spark discharge.

Recovery time

After each spark avalanche, there remain electrons, ionized ions and energy stored as metastable atoms which could give delay ionization. If these are not removed prior to the next pulsing of the wsc, another spark avalanche will be initiated at the same spot. This is clearly undesirable. We want as few extra sparks as possible. Thus, these electrons, ions and metastable atoms must be removed.

The mobility of the electrons in our gas mixture is of the order of 10^3 cm^2/sec-volt which gives a clearing time of about 10 microsec for 17 volts across 1/4". So the electrons cause no problem.

The ion mobility is much slower -- about 2-5 cm^2/sec-volt which imply a clearing time of about 10 msec. We speed this up by applying the pulsed clearing field of several hundred volts so that the ions are removed in about 1/4 of that time.

Residual energy from a discharge can be stored as metastable atoms which could produce delay ionization up to 100 msec. However, isopropanol vapor, having low level ionization energies, tends to absorb the energy from metastable atoms and get ionized. This

process, called "quenching", allows the stored energy to be dissipated within about 10 msec[B.9].

Hence, the recovery time for the wsc is approximately 10 msec. We impose a dead time of 20 msec between successive triggers to safely allow the wsc to recover. This is done by gating several critical beam counting modules and trigger logic modules off for 20 msec after each trigger.

Spark position determination

The measured spark positions may deviate from the actual spark positions for many reasons. The spark chamber inherently possesses several sources which contribute to this problem.

Spark jitters[B.10], defined as displacement of the spark from the real path of the ionizing particle, are a function of the gas composition, the DC clearing field strength, the amount of delay prior to sparking and the angle of incidence of the particle path.

Quenching vapor (in our case, the isopropanol) restricts the avalanche to the region of the primary ionization electrons. Hence the size of the spark jitter would be inversely correlated with the number of primary ionization electrons. We used an optimized mixture of 90% He, and 10% Ne which has a primary ionization density of 22 cm^{-1}. This gives an average standard deviation of the spark position of $\pm$ 0.4 mm[B.11].

Primary electrons may drift due to the DC clearing field. If the ionizing particle enters at an acute angle, this drift will affect the position resolution. The size of the deviation would be dependent on the angle of incidence and delay in sparking.

In addition to these inherent deviations, two other items affect the resolution: the wire spacing and the digitizing frequency. The wires are spaced 1.25 mm apart. The current flow in each wire is proportional to the strength of the coupling between the spark and the wire when more than 1 wire carries current from the same spark. Thus, the spark determination could be better than ± (1.25 mm)/2. We use 10 megacycle scalers to clock the signal in the digitizer. The position is thus quantized in steps of 0.52 mm (the velocity of the magnetostrictive wave being 0.52×10^7 mm/sec). This limits the spark determination.

All these factors suggest that the deviation in the determination of spark position should be of the order of 0.5 mm. A study of the distribution of sparks for straight tracks shows a standard deviation slightly less than 0.9 mm.

Two-spark resolution

The two-spark resolution is limited by the size of the pick-up coil and is about 3 mm. However, since we require only one track in each chamber, this fact is unimportant for this experiment.

(B-viii) Assessment of the wsc System in Relation to our Experiment

We assess our wsc system in terms of spark position determination, repetition rate and time lost due to wsc failure.

Spark position determination

Does the deviation in spark determination affect the momentum determination significantly? The typical bending by the magnet is 250 mr. The lever arms of the two sets of wsc to either side of the magnet are about 60 cm. A deviation of 1 mm would imply an error of

1.7 mr in angle. Therefore, we expect a possible 3/4% error in momentum determination from chamber position determination alone. This is not excessive since multiple scattering and beam spread cause similar deviations in momentum determination. The over-all result in momentum determination is shown in Figure 2.7c (page 29). Considering the various inherent deviations which cannot be removed, the position determination of our wsc is as well as can be expected.

Repetition rate

20 msec dead time is a significant waste. If we have 15 triggers per pulse, at least 75% of the beam is wasted. However, the recovery time of 10 msec cannot be reduced unless we do not spark our chambers (which could be achieved by using wire proportional chambers[2.39]). Fortunately, this was not necessary since our trigger rate was not always so high. On the average, we used 60% of the beam.

Time lost due to wsc failure

10% of useful beam is lost due to failure of the wsc system. Some typical problems include gas system trouble, pulser failure, etc.[B.12] The operation during the rest of the time is quite adequate.

APPENDIX C: INEFFICIENCIES IN RECONSTRUCTION OF TRIGGERED EVENTS

(C-i) Introduction

As we mentioned in Section (b) of Chapter III, there are inefficiencies in reconstruction of events. We quoted a 5% loss of backward elastic events due to these inefficiencies. In this appendix, we elaborate on the methods we use to derive this number. In Section (C-ii), we describe two major tools we use to study the inefficiencies. Section (C-iii) contains a description of the sizes of the inefficiencies and the methods we use to obtain them.

Reconstruction is inefficient only if:

1. Some of the tracks associated with the backward elastic event were not found.
2. The event associated track was mistakenly discarded in the spurious track removal procedure.
3. Reconstructed tracks give kinematical or topological reconstructed quantities which differ from the actual quantities by sufficient amounts to make us discard the event.

We find that there is a 3% inefficiency in the trackfinding procedure in regions 1 and 2. There is also a 2% inefficiency in the extra track removal procedure. No loss due to item 3 above is found.

(C-ii) Tools used to Study Reconstruction Inefficiency

Two important tools are used to study the reconstruction inefficiency:

1. Scanning and detailed study of selected events.

A special program has been written[C.1]. When it is used with the reconstruction program, we obtain for each event (or selected

events) a Calcomp plotter[C.2] picture with the positions of the sparks from the wsc plotted geometrically. Figure C.1 contains pictures for several events. For each event, there are two views -- a horizontal view with the sparks from regions 1,3, and 5 and a vertical view with sparks from regions 2, 4, and 6. This allows us to treat the wsc data like optical spark chamber pictures. We perform various optical scans to check the reconstruction procedure.

The program also prints out the raw spark positions, the counter bit information, the track(s) found in each region and the tracks accepted by the spurious track removal procedure. For each track, we print out the positions of the sparks associated with the track, the extrapolated slope and intersect (at z = 0 plane) and the chi-square of each fitted track. This allows us to make a detailed study of pathological events.

2. Modifying the reconstruction procedure

A modified version of the reconstruction program[C.3] was written to check the reconstruction procedure. We concentrate on checking the trackfinding efficiency in regions 1 and 2 where, as we will mention in the next section, sizable inefficiencies are suspected. We also check the spurious track removal procedure by using a different method in removing spurious tracks.

To check the trackfinding inefficiencies in regions 1 and 2, the modified reconstruction program bypasses these regions. That is, it creates artificial tracks in regions 1 and 2 designed to give acceptable reconstructed vertex and VD (vertex deviation). Thus, any event with the appropriate tracks in regions 3, 4, 5 and 6

Figure C.1: Calcomp plotted pictures of triggered events. (a) An event with the desired topology. Note that the tracks from regions 3 and 5 meet very closely at the center of the magnet. So do the tracks from regions 4 and 6.

(b) An event with extra spurious tracks (dashed lines) in regions 1-4. Extra tracks in regions 1 and 2 removed since the extra tracks have wrong slope for beam particle. Extra tracks in regions 3 and 4 removed since they do not meet the tracks from regions 5 and 6 at the center of the magnet.

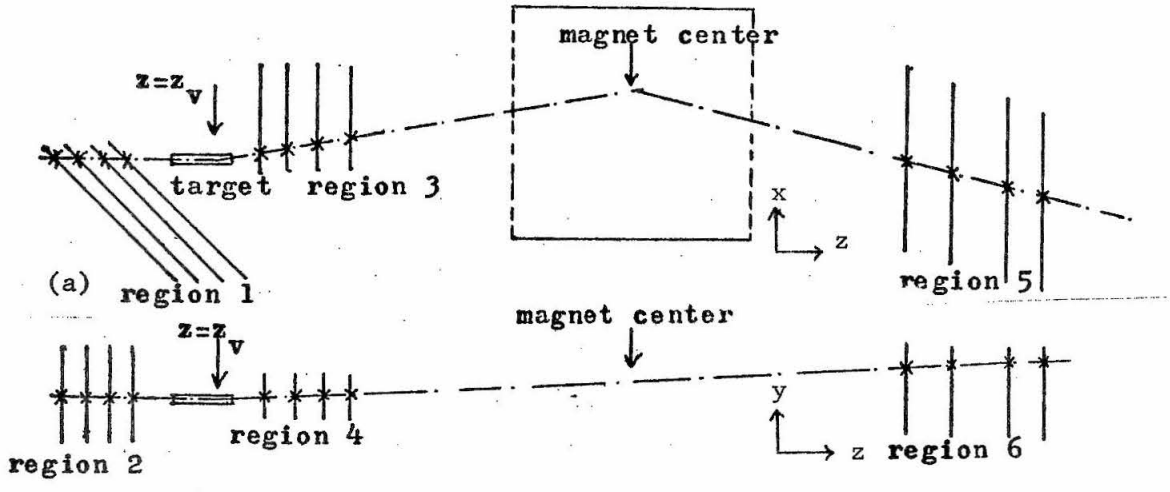

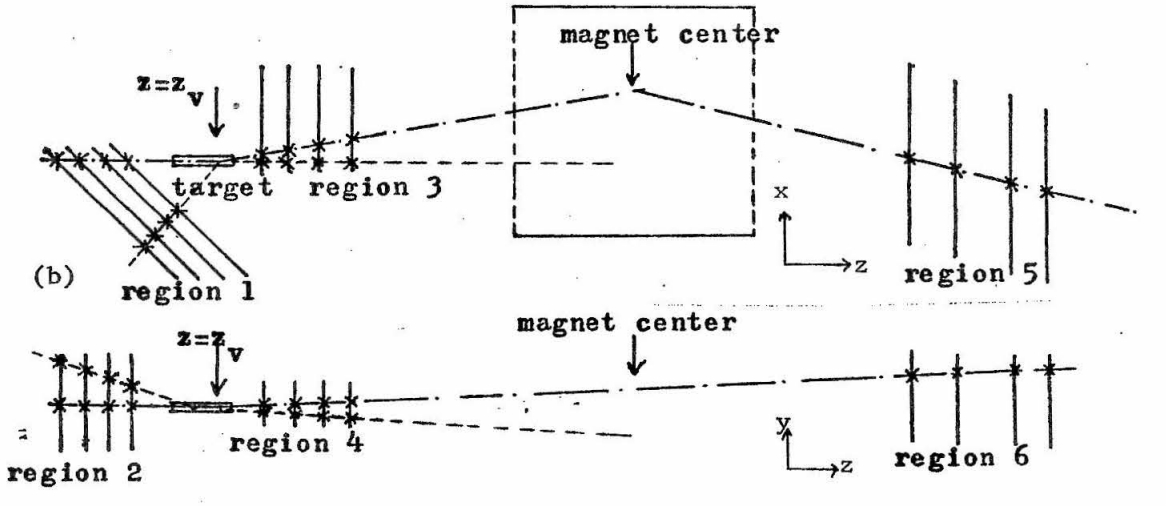

satisfying the MTD (magnet track deviation), momentum and velocity criteria will be accepted as backward elastic events. Any events gained by this modified procedure could represent inefficiencies in trackfinding[C.4].

To check spurious track removal procedure, the modified reconstruction program uses a procedure based entirely on topological quantities VD and MTD. No counter information is used. The combination of tracks which give the smallest MTD and then VD are considered the event associated tracks. In addition, ambiguity limits MTD_a and VD_a are defined (see Figure 3.2, page 79) so that more than 95% of backward elastic events would have MTD and VD less than these limits. The percentage of events which have more than one combination of tracks with MTD (VD) less than MTD_a (VD_a) are obtained and these events are selected for detailed study. We can use topological quantities such as MTD, VD and the information on whether the tracks in regions 4 and 6 are parallel[C.5] to help us decide whether the combination of tracks with the minimum MTD and VD are indeed the best choice.

(C-iii) The Sizes of the Reconstruction Inefficiences

A. Inefficient Trackfinding

(i) Given the existence of the sparks, the trackfinding inefficiency is less than 1%.

Given the existence of the sparks from a track, trackfinding is inefficient only if there are program errors or misalignment of sparks. Program errors include the slope and straightness require-

ments of the reconstructed tracks. Misalignment due to multiple scattering or chamber resolution may cause significant numbers of tracks to be rejected by the slope and straightness criteria.

For each track found, we calculate a chi-square assuming standard deviations of 0.5 cm. All tracks with chi-square greater than 6.6 are rejected. A survey of several hundred tracks for backward elastic events reveals that about 97% of tracks have chi-square less than 0.5 and only 1/2% has chi-square exceeding 1.0. Since the chi-square distribution is expected to be a Poisson distribution, this implies that the cutoff at 6.6 is safe. Much less than 1% of true tracks should have chi-square exceeding that number. Thus the straightness criterion has inefficiency less than 1%.

There is also a slope criterion on the tracks found. In regions 1, 2, 3, 4, and 6 only those tracks which extrapolate through the target is acceptable (no slope criterion for tracks in region 5 is possible due to the bending of trajectories through the magnet). A study of several hundred backward elastic events reveals that there a are no events with track slopes in those regions which are anywhere close to the limits set. This implies that any loss due to the slope criterion is unlikely. Thus, the inefficiency in the slope criterion is again less than 1%.

(ii) <u>There is an apparatus inefficiency of between 0 to 5% causing missing sparks. This is discussed on page 88 and this inefficiency is not considered a reconstruction inefficiency. This inefficiency is obtained by assuming the wsc inefficiencies to be uncorrelated</u>.

(iii) In the absence of more than 1 track in each region, the apparatus inefficiency mentioned above does reflect the actual inefficiency.

If there are no other spark(s) besides the 1, 2, 3 or 4 sparks of a single tracks, we can check for correlated inefficiency easily by scanning. Knowing the number of 4-spark and 3-spark tracks gives us some idea of the number of 2 spark tracks to expect assuming no correlated inefficiency. A scanning of about 500 pictures of events shows that the number of 2-spark tracks is as expected. Thus, in this case, the uncorrelated apparatus inefficiency does reflect the actual inefficiency.

(iv) In the presence of more than one track or extra spark, the apparatus inefficiency still reflects the actual inefficiency in regions 3, 4, 5, and 6.

Correlated inefficiency exists in cases where there are more than one track. Wsc sparking efficiency for two sparks is much less than the sparking efficiency for one spark[C.6]. In our case, the fact that we accept a maximum of 4 sparks per wsc may also contribute to correlated inefficiency. Therefore, additional correlated inefficiency is expected. We will consider this a reconstruction inefficiency.

The size of the inefficiency would be correlated with the percentage of time more than one track goes through a particular set of wsc. By scanning about 500 event pictures, we conclude that the additional correlated inefficiency in regions 3, 4, 5, and 6 is less than 1%. Multiple tracks exist for about 15% (5%) for all triggered

events in regions 3 and 4 (5 and 6). Scanning shows that the amount of events where there is (in either regions 3, 4, 5, or 6) one track with two other sparks possibly from another track is as expected if the uncorrelated apparatus inefficiency reflects the actual inefficiency.

(v.) In the presence of more than one track or extra spark, there is, in regions 1 and 2, an additional correlated inefficiency of 3%.

About 50% of triggered events have multiple tracks in regions 1 and 2. Scanning is not very useful since there are many extra tracks or sparks in the beam track region. Even though there are an average of 1.25 beam tracks per event, the number of events where no beam tracks are found cannot be accounted for by the uncorrelated wsc inefficiency alone. The trigger requirement is such that a particle must have gone through regions 1 and 2. Thus, additional correlated inefficiency is suspected.

The modified reconstruction program gives us the size of this correlated inefficiency. By bypassing the track finding in regions 1 and 2, we get N backward elastic events, where the normal procedure gives us M events. Note that for these studies, the vertex cut is not made since the vertex information is lost by not finding the beam track. The correlated inefficiency in regions 1 and 2 is thus $X_c = (N - M)/N - X_{unc}$ where X_{unc} is the uncorrelated wsc inefficiency in regions 1 and 2. We have applied this procedure to 5 sets of data runs and obtained the following results:

Date name and momentum	M	(N - M)	(N - M)/N	X_{unc}	X_c
A(0.812)	108	3	2.7%	0.1%	2.6%
B(1.590)	91	3	3.2%	0.8%	2.4%
C(1.844)	262	11	4.0%	1.7%	2.3%
D(1.338)	227	23	9.2%	2.9%	6.3%
E(1.797)	460	16	3.4%	1.3%	2.1%
Total-weighted average	1148	56	4.7%	1.7%	3.0%

We have studied the possible correlation between X_c and such factors as uncorrelated wsc inefficiency in regions 1 and 2, incident flux density and incident momentum. No strong correlation was found.

B. Inefficiency in Spurious Track Removal

About 30% of the events with sufficient tracks to be tested for backward elastic events have multiple tracks in some region. We check the spurious track removal inefficiency by using the modified procedure mentioned in page 190. In the modified spurious track removal procedure, we pick the combination of tracks with the smallest MTD and VD. A study of several hundred events with extra tracks convince us that the amount of ambiguous events is less than 2%. These ambiguous events are those which have two or more combinations of tracks with MTD or VD which are reasonable (i.e., within the ambiguity limits as defined in page 192). Thus, the over-all normalization correction needed for all the events is less than 30% times 2% = 0.6% which we shall neglect. Thus, the modified spurious track removal procedure is less than 1% inefficient.

We obtain the spurious track removal inefficiency of our normal reconstruction procedure by finding the number of events gained by the modified procedure. We find the inefficiency X_{str} is

Data name and momentum	Normal procedure	Modified procedure	X_{str}
A(0.812)	108	110	1.8%
B(1.590)	91	97	6.6%
C(1.844)	262	267	1.8%
D(1.338)	227	230	1.3%
E(1.797)	460	468	1.7%
Total	1148	1172	2.1% which we round off to 2.0%

Note that this actually constitutes an inefficiency in the spurious track removal procedure of about 7% since only 30% of the reconstructed events have multiple tracks.

C. Inefficiency due to Reconstructed Values Differing from Actual Values of the Kinematic or Topological Quantities

This inefficiency arises from the various selection cuts we use in obtaining the backward elastic events. We consider this inefficiency to be selective cut inefficiency and study it in the the appropriate section (Section (c) of Chapter III).

We summarize the reconstruction inefficiencies here. There is an additional correlated inefficiency in regions 1 and 2 of 3%. There is also inefficiency in the spurious track removal procedure of 2%. Thus, there is a total reconstruction inefficiency of 5%.

REFERENCES

1.1 For example, resonance contribution in the s channel gives a Breit-Wigner amplitude for a particular spin wave.

1.2 For L greater than 0, the amplitudes, which are functions of P_L^0, P_L^1 and (for $\bar{p}p$) P_L^2, tend to give stronger contributions near the extreme angles.

1.3 Resonance amplitudes are Breit-Wigner functions. Thus they peak at the position of the resonances. Backward peaking comes from the P_L^0 term in the resonance amplitude.

1.4 Kormanyos et al., Phys. Rev. 164, 1661 (1967).

1.5 See, for example, Chapter 9 of "High Energy Collisions of Elementary Particles" by Eden, University Press, Cambridge, 1967.

1.6 A.S. Carroll et al., Phys. Rev. Letters 21, 1282 (1969; and S. Tewksbury, thesis, University of Rochester (unpublished).

1.7 "Exotic"resonances are those which cannot exist under the simple quark model (where all baryons are made up of three quarks and all mesons of quark-antiquark). For example, Z*(B = 1, S = 1) is exotic.

1.8 We discuss this in Chapter V, Section (c-i). The January 1970 data booklet by the Particle Data Group (LRL and CERN) contains a table of many heavy meson resonances (pp. 20 and 21).

1.9 We discuss this in Chapter V, Section (c-ii).

1.10 J.K. Yoh et al., Phys. Rev. Letters 23, 506 (1969).

1.11 H. Nicholson et al., Phys. Rev. Letters 23, 603 (1969); and B.C. Barish et al., Phys. Rev. Letters 23, 607 (1969).

1.12 (K^-p) A.S. Carroll et al., Phys. Rev. Letters 23, 887 (1969).
(K^+p) A.S. Carroll et al., Phys. Rev. Letters 21, 1282 (1969).
($\pi^\pm p$) A.S. Carroll et al., Phys. Rev. Letters 20, 607 (1968).

2.1 For example, both BNL and CERN have partially separated beams in this momentum range.

2.2 If the forward proton in a $\bar{p}p$ interaction is a result of elastic scattering, the momentum is significantly higher than if the scattering is inelastic.

2.3 Knowing the velocity and momentum of a particle allows us to determine the e/m ratio and thus the type of particle it is.

2.4 Multiple scattered events are difficult to handle and therefore they are discarded. We account for this in our Monte Carlo program when we calculate the solid angle acceptance.

2.5 Designed by B. Barish of Caltech and T. Kycia of BNL. This beam covers the momentum range of about 0.7 GeV/c to 2.4 GeV/c (up to 3.0 GeV/c for the other branch of the beam) and provides about a factor of 100 in reduction of pi's for a $\bar{p}$ beam.

2.6 Cherenkov radiation is emitted whenever a particle in a medium has velocity faster than the speed of light in that medium. The standard reference for Cherenkov radiation is Jelly's "Cherenkov Radiation and its Application", Pergamon Press, New York (1950). The liquid differential Cherenkov counter

we use was constructed by B. Leontic and associates of BNL. We thank him for permission to use this counter.

2.7 S_3 is placed as close to the target as possible since we are using it to aperture the beam, which we want to pass through the target.

2.8 We used wire spark chambers constructed by J. Fischer of the Instrumentation Division of BNL. See report No. 11031 (BNL) by J. Fischer titled "Digitized Spark Chambers in High-Energy Physics".

2.9 The gas threshold Cherenkov counter was loaned from W.A. Wentzel of Berkeley for which we thank him. The optics of this counter are more suitable for a target situated closer to the counter. Fortunately, the mirrors are adjustable. Thus the performance of this counter is acceptable for the geomentry of our experiment.

2.10 See Appendix B, Section (B-vi) for a discussion of the recovery time needed for the ionization from previous sparks to dissipate.

2.11 See Figure 2.8 (page 33) for an idea of the loose momentum criterion imposed by the combination of P-R counters.

2.12 Most of the spurious tracks resulted from the delay between the event and the spark discharge. It takes approximately 300 nsec to apply high voltage to the wsc. See Figure 2.14.

2.13 The sizes and positions of these counters are given in Table 2.1. These counters have 3' air light pipes.

2.14 See Figure 2.14 for the timing diagram.

2.15 Chronetic logic modules were on loan from BNL HEP.

2.16 These distributions were obtained from wsc reconstruction of beam tracks.

2.17 Wsc resolution and multiple scattering accounts for a large portion of the spread in momentum and slopes but is not important for the spread in position of the beam.

2.18 The target was constructed and maintained by the BNL AGS target group.

2.19 The vent tube is directly connected to atmospheric pressure. We found that the boiling rate is such that the volume of bubbles inside the target is less than 1%.

2.20 The gap between successive plates of iron increases the magnetic impedance between the plate. The inner plates became saturated before the next plate was coupled strongly into the magnetic circuit.

2.21 The nuclear magnetic resonance probe meters were manufactured by Varian Associates. We used H_2O and D_2O as samples in the probe.

2.22 S. Tewksbury, thesis (University of Rochester) unpublished, 1969. He studied the magnet D_4 of this experiment in great detail including doing a field map of $B_y(x,0,z)$ along z for several x values at many momenta to obtain parameters for a particular parameterization by Danby et al. ("Three-dimensional projection of magnetic beam transport elements" in Proc. of Particle Acc. Conf., Washington D.C., March 1-3, 1967). This parameterization was verified at B = 11 Kgauss by

measuring the values at y = + 8". The predicted values and measured values differ by less than 0.3%.

2.23 As we will mention in Section (B-viii) of Appendix B, wsc position determination would cause a momentum spread of about 3/4%.

2.24 This is limited by the size of the buffer in the PDP-8 since we write the events on tape only at the end of each pulse of the beam. During the first part of the experiment, only 10 triggers per pulse are taken.

2.25 Logic modules used are Chronetic 100 megacycle logic modules borrowed from BNL HEP.

2.26 We are saturated only during the high momentum runs. For the remaining momenta, a 40% reduction in trigger rate is not very useful. For example, if we have 5 triggers per pulse, reducing the trigger rate by 40% would enable us to use 13% more beam.

2.27 Currently, we are analyzing $\bar{p}p$ into pi^+ and rho^- and preliminary results are expected in a few months.

2.28 Half of the counter bits use EG & G electronics modules. The other half use electronics made at Caltech by A.V. Tollestrup.

2.29 For example, K^-p into $pi^-\Sigma^+$ could result in the pion having momentum higher than the initial state kaon.

2.30 At the pressure we are using, the Freon-12 will condense if the temperature is below 25^oC.

2.31 We used RCA-7046's borrowed from T. Kycia of BNL. Although their

quantum efficiency is low, they are quite fast (2 nsec rise time).

2.32 Quantum efficiencies of 20% are possible. For example, RCA 4522's are 5" tubes with fast rise times (2.5 nsec) and high quantum efficiencies (up to 29%). However, they cost $900 apiece.

2.33 A liquid Cherenkov counter considered for another part of this experiment. We could have built a liquid Cherenkov counter with threshold of 1.0 GeV/c for protons had it been needed.

2.34 The preliminary analysis is done at the CDC-6600 computer usually within 5 hours of the data taking.

2.35 The interfacing uses modules manufactured by Computer Control Co. Inc., Framingham, Mass. The interfacing, digitizer, and PDP-8 programs were designed and written by H. Pate and modified by A. Entenberg (Rochester University), B.C. Barish and A.V. Tollestrup.

2.36 The positions of the wsc and fiducials were surveyed to 1/16" both when they were installed and when they were removed.

2.37 The digitizer is designed and constructed by the instrumental division of BNL. It includes 4 scalers (Texas Instrument Co., modified to count in base of 8) and an oscillator (10 MHz Tektronix time mark generator) with several fast logic modules (developed at BNL; R. Sugarman, F. Merrit, W.A. Higginbotham, Nanocard Counter Circuit manual, BNL report 711 (T-248)).

2.38 The PDP-8 uses 12-bit words. Thus, 5 PDP-8 words are combined to form a CDC-6600 60-bit word.

2.39 G. Charpak et al., Nuclear Instr. & Methods 62, 262 (1968).

2.40 This is not absolutely true since for a particular incident momentum, some process like $\bar{p}p$ into pi and A_2 could result in large numbers of forward pions with momentum close to incident momentum. However, the width of the A_2 and the fact that we are using wrong kinematics (i.e., assuming proton forward) will spread the enhancement out so that any enhancement would be very weak compared to the elastic peak.

2.41 Methods for determining energy of particles includes total absorption counters and range counter. Their resolution and efficiency are much worse than magnet-wsc spectrometers.

3.1 The first stage program is written by A.S. Carroll and the second stage program by A.S. Carroll and the author.

3.2 These reconstructed quantities may be different from the actual quantities. This will be considered in later discussion.

3.3 The Monte Carlo program is written by Y. Nagashima.

3.4 The positions of the fiducials are surveyed.

3.5 The trackfinding procedure is modified by M. Hind from a program used in a CERN experiment.

3.6 This is true to robbing of energy between sparks.

3.7 See Section (C-ii) of Appendix C.

3.8 Bricman et al., Physics Letters 29B, 451 (1969).

3.9 See Section (C-ii) of Appendix C.

3.10 See reference 2.40 above.

3.11 As mentioned in Ref. 2.40 above, pions could have a weak en-

hancement underneath the elastic peak. Thus, we do not correct for the loss at each momentum separately since chance coincidence could put the pion enhancement either in our signal bins or background bins (see the next section (c-v)) at a particular momentum.

3.12 The studies indicate that the correction at each momentum ranges between +7% to -2%. However, the statistics are poor -- usually based on less than 10 events.

3.13 R.J. Abrams et al., Phys. Rev. Letters 18, 1209 (1967); C. Daum et al., Nuclear Phys. B6, 617 (1968).

3.14 Our criteria for backward elastic events will only reject about 35% of events with additional forward elastic scattering of incident $\bar{p}$.

3.15 Although the actual distribution is not really a gaussian, the approximation is sufficiently adequate.

3.16 A simpler Monte Carlo program has been written by the author to check the program written by Y. Nagashima.

3.17 Written by the author.

3.18 At one atmosphere near boiling point.

3.19 Usually, we have between 25 to 200 events per bin.

3.20 See reference 2.40.

3.21 For example, additional scattering in the magnet region will not allow us to determine the momentum of the particle.

3.22 In our data tape, each event record is a separate block. If we had put several records in each block, the tape reading time would have been drastically decreased.

3.23 As we mentioned in the previous chapter, there is a PDP-6 at the AGS which we could have used.

4.1 The standard least-square fitting procedure involves minimizing the chi-square by flipping the error matrix. See page 365, Mathews and Walker, "Mathematical Methods of Physics", Benjamin, New York (1964).

4.2 D. Cline et al., Phys. Rev. Letters 21, 1268 (1968).

4.3 W.A. Cooper et al., Phys. Rev. Letters 20, 1059 (1968).

4.4 J. Lys et al., Phys. Rev. Letters 21, 1116 (1968).

4.5 D. Cline has informed us of $\bar{p}p$ bubble chamber film up to 0.85 GeV/c which is under analysis. Mendelkern of UC Irvine was reported to have $\bar{p}p$ bubble chamber film near 1.0 GeV/c under analysis.

4.6 See Figure 2.7 (page 29) for a distribution of incident momentum of $\bar{p}$'s hitting each mass slit counter.

5.1 If $\alpha(0)$ of a trajectory is -3.5, then the physical states lying on this trajectory would have mass higher than about 2 GeV if the slope is 1 GeV^{-2}. This would be in agreement with the trajectory being a dibaryon trajectory (masses would be expected to be heavier than two protons). However, note that the u dependence of our $\alpha(u)$ is about 3 GeV^{-2}. If this is true, then one might expect mass states of about 1 GeV.

5.2 See, for example, page 19 of "Meson and Baryon Spectroscopy" by D.B. Lichtenberg, Springer-Verlag, New York (1965).

5.3 This idea was suggested both by Professor Frautschi of Caltech and Dr. A.S. Carroll of BNL.

5.4 For a general discussion of angular distribution of scattering cross sections, see Blatt and Biedenharn, Rev. Mod. Phys. 24, 258 (1952). A more detailed discussion of the $\bar{p}p$ elastic system is contained in Lys, Phys. Rev. 186, 1691 (1969).

5.5 It is easy to demonstrate that $\bar{p}p$ is 1/4 singlet and 3/4 triplet. $\bar{p}p$ is 1/4 abnormal triplet and 1/2 normal triplet since there is $L_1 = J$ abnormal triplet states and $L_2 + L_3 = (J + 1) + (J - 1) = 2J$ normal triplet states.

5.6 Blatt and Biedenharn, Rev. Mod. Phys. 24, 258 (1952).

5.7 M.N. Focacci, et al., Phys. Rev. Letters 17, 892 (1966); and R. Baud et al., Physics Letters 30B, 129 (1969).

5.8 R.J. Abrams et al., Phys. Rev. Letters 18, 1209 (1967).

5.9 E.W. Anderson et al., Phys. Rev. Letters 22, 1390 (1969).

5.10 Yen at Argonne has calculated the positions of the expected enhancements due to pi minus p going to (N or N*) and (pi or rho) for the particular geometry of the experiment of Anderson (ref. 5.9) at the suggestion of C.N. Yang. The positions correspond to the positions of the bumps found in the experiment. Thus, kinematic enhancement is likely. However, to have the size of the bumps as observed, the coupling would have to be very strong.

5.11 M. Adelholz et al., Nuclear Phys. B14, 255 (1969).

5.12 Diamond (Wisconsin-W.D. Walker group) private communication.

5.13 D. Cline et al., Phys. Rev. Letters 21, 1268 (1968).

5.14 W.A. Cooper et al., Phys. Rev. Letters 20, 1059 (1968).

5.15 Kalbfleisch et al., Physics Letters 29B, 259 (1969).

5.16 G.A. Smith (Michigan State), private communication.

5.17 J. Lys et al., Phys. Rev. Letters 21, 1116 (1968).

5.18 C. Bricman et al., Physics Letters 29B, 451 (1969).

5.19 D. Fong, thesis (Caltech, 1968) and D. Fong et al., to be published.

5.20 H. Nicholson et al., Phys. Rev. Letters 23, 603 (1969) and Caltech report CALT-68-197.

5.21 J.W. Chapman et al., Phys. Rev. Letters 21, 1718 (1968).

5.22 G. and S. Goldhaber, in "Advances in Particle Physics" edited by Cool and Marshak, Interscience, New York (1968).

5.23 D.Z. Freedman and J.M. Wang, Phys. Rev. 153, 1596 (1967).

5.24 M. Gell-Mann, Physics Letters 8, 214 (1964); and G. Zweig, CERN preprint 8419/Th. 412.

5.25 The 0^{-+} includes π, K, η and probably X^0. The 1^{--} includes ρ, $K^*(890)$, ω, and φ. The 2^{++} includes A_2, $K^*(1420)$, f^0 and f'.

5.26 See Ref. 5.22 and Dalitz's article in "Proc. of 12th International Conf. on High-Energy Physics" UC Press, Berkeley (1967).

5.27 The positions and widths of the 3^{--} and 5^{--} are 2.12 GeV (less than 250 MeV wide) and 2290 MeV (less than 165 MeV wide). These can be identified with the L = 4, I = 1 states in Figure 5.3c.

5.28 Radial excitation in the $q\bar{q}$ model would allow low-lying trajectories in addition to those in Figure 5.3.

5.29 We use the mass slit counter information for this study. See Figure 2.7 (page 29) for the distribution of incident momentum for particles hitting each mass slit counter.

5.30 See Section (b-ii) of this chapter.

6.1 Usually, the diffractive background is treated apart from exchange and direct channel resonance effect and one writes $A = A_{diff} + A_{dual}$ where A_{dual} is either A_{res} or A_{exc}.

6.2 See, for example, Coombes et al., Phys. Rev. 112, 1303 (1958); and Armenteros et al., Phys. Rev. 119, 2068 (1960).

6.3 See Ref. 6.2 and, for example, Greider and Glassgold, Annals of Physics 10, 100 (1960).

6.4 It is possible that antishrinking continues at higher momentum so that the radius of $\bar{p}p$ elastic diffractive peak approaches that of the pp elastic diffractive peak, which is about 0.7 Fermi.

6.5 See Figure 6.2

6.6 Diffractive minimum arises due to interference of the partial waves. Diffractive minimum should be at constant t at small angles but should be at lower t at large angles.

6.7 D. Cline et al., Phys. Rev. Letters 21, 1268 (1968).

6.8 C. Daum et al., Nuclear Phys. B6, 617 (1968).

6.9 J. Berryhill and D. Cline (private communication-Wisconsin), and B.C. Barish et al., Phys. Rev. Letters 17, 720 (1966).

6.10 The diffraction scattering can be viewed as shadow scattering of the absorption of the wave by inelastic processes.

6.11 Frahn and Venter, Annals of Physics 27, 135 (1964).

6.12 Goldberger and Watson, "Collision Theory" (New York, Wiley, 1964) contains a rigorous derivation of the scattering matrix of two fermion systems (Section 7.3).

6.13 See. Ref. 6.11 and also E. Fermi, Nuovo Cimento II, Supp. 1, 84 (1955).

614. For example, the model of Ref. 6.11 allows the radius of the J = L + 1 term to be different from the radius of the J = L - 1 term.

6.15 T.T. Chou and C.N. Yang, Phys.Rev. 170, 1591 (1968).

6.16 For references on quark model, see references 5.22, 5.24 and 5.26. The parton model might be considered a generalization of the quark model and is developed by Feynman. It assumes that the proton contains point-like constituents. See S.D. Drell et al., Phys. Rev. Letters 22, 744 (1969).

B.1 Constructed by J. Fischer of BNL.

B.2 The pulsers were manufactured by Instrumental Division of BNL.

B.3 Ref. 2.8, Figure 5 is a plot of sparking efficiency vs. delay for different values of the DC clearing field.

B.4 Isopropanol, spectral grade, obtained from Kodak Co. Rochester, N.Y.

B.5 The feed-through system was used during the early part of this experiment. The recycling system was constructed by R.H. Phillips.

B.6 The major contamination is water vapor. This is removed by

running the exhaust gas through a liquid nitrogen cooler to condense the water vapor and also through some activated charcoal to absorb other impurities in the gas.

B.7 See R.M. Bozorth, "Ferromagnetism" D. Van Nostrand, New Jersey, (1951), pages 595-712.

B.8 The iron-cobalt wire supplied by W.B. Driver Co., Newark, New Jersey, under thetrade name Remendur.

B.9 This is achieved with about 1% isopropanol vapor.

B.10 Similar to the spark jitter observed in optical spark chambers (see O.R. Frisch (editor), "Progress in Nuclear Physics", Vol. 9, McMillan, New York (1964) pages 3-26).

B.11 100% He, 75% He/25% Ar and 90%He/ 10% Ne gives primary ionization densities of 5, 14, and 22 cm^{-1}, respectively, which imply average standard deviations of ± 0.8, ± 0.5 and ± 0.4 mm, respectively.

B.12 Among the major sources of wsc failure are gas flow stoppage, impurities in the gas, too much or too little alcohol in the gas, etc.

C.1 Written by A.S. Carroll.

C.2 Manufactured by California Computer Products, Inc.

C.3 Modified program called ROCHEK developed by the author.

C.4 As mentioned in Chapter III, only backward elastic scattering would result in a forward proton with momentum close to the incident momentum.

C.5 Since the bending magnet should not alter the vertical trajec-

tory, the track in regions 4 and 6 should be close to parallel.

C.6 Multi-spark efficiency is reduced due to robbing of energy. In our case, the two-spark efficiency is still of the order of 90% and is usually acceptable.